CONTROLLED SELF-ASSEMBLY OF 2D COLLOIDAL LIQUID CRYSTALS

A Dissertation

by

DALI HUANG

Submitted to the Office of Graduate and Professional Studies of
Texas A&M University
in partial fulfillment of the requirements for the degree of

DOCTOR OF PHILOSOPHY

Chair of Committee,	Hong Liang
Committee Members,	Tahir Cagin
	Svetlana Sukhishvili
	Qingsheng Wang
Head of Department,	Ibrahim Karaman

May 2021

Major Subject: Materials Science and Engineering

ABSTRACT

This dissertation research investigates two-dimensional (2D) nanoparticles, their synthesis, characteristics, function and performance. The 2D nanoparticles, as a novel class of materials, have attracted significant interest in last two decades. With the development of synthetic technology, many 2D materials like graphene, MXenes, transitional metal dichalcogenides, boron nitride, black phosphorus, and emerging hybrid materials have been developed and achieved more complicated structures. The 2D particles possess distinct properties like low-dimension, ultrathin thickness, and large surface areas. The controlled self-assembly of 2D materials enabled additional functions and device fabrication. In particular, colloidal suspension of 2D materials displays a plethora of liquid crystal phases including isotropic, nematic, smectic due to self-assembly variance. Liquid crystal is an intermediate state between liquids and solids, which has relatively ordered arrangements and flows like a fluid. The direct optical visualization of 2D liquid crystals is incredibly beneficial to investigate the real-time self-assembly and orientation of 2D colloids. Therefore, investigation of 2D colloidal liquid crystals, accompanying the control of structure, self-assembly and phase transition property, has become the critical influencing aspect in 2D materials.

In this dissertation, 2D nanoparticle zirconium phosphate (ZrP) has been chosen as a model for investigating the nanoplate liquid crystal phase transition behaviors. We investigate 2D materials' structure, processing and optical performance relations. ZrP is working as a template particle due to its high shape anisotropy, controlled morphology,

small polydispersity and high diameter-to-thickness ratio. The self-assembly of ZrP liquid crystals is affected by internal properties and external fields at the same time.

We use an experimental approach to study controlled self-assembled 2D nanoparticle liquid crystals. It includes four major activities: synthesis of 2D ZrP crystals and liquid crystals; development of aspect ratio dependence of liquid crystal phase transition; investigation of the temperature field dependence of liquid crystal phase transition; study the concentration dependence of nematic liquid crystal photonic applications. The ZrP liquid crystal phases are found to be precisely tuned through aspect ratio, temperature and concentration. The self-assembly controlled 2D ZrP colloids will facilitate understanding the processing and performance of 2D materials in diverse areas like photonics, energy storage, sensors and electronics.

DEDICATION

To my family.

ACKNOWLEDGEMENTS

I would like to sincerely thank my advisor, Dr. Hong Liang for her great guidance, support and patience throughout my research. I am very grateful for her valuable discussion, critical suggestion and encouragement during my Ph.D. study.

I would like to thank my committee members, Dr. Tahir Cagin, Dr. Svetlana Sukhishvili and Dr. Qingsheng Wang for supporting my research study. All of your suggestions and help lead my way to proceed.

I also would like to express my deepest gratitude to Dr. Zhengdong Cheng. His research advising is the crucial motivation and direction for me to complete this dissertation work. I am very thankful for his inspiring discussions and dedicated support.

I greatly appreciate for Dr. M. Sam Mannan, Dr. Stewart Behie and Dr. Noor Quddus in Mary Kay O'Connor Process Safety Center for the continuous research and financial support. The time working in the center is an impressive memory to me.

Moreover, I acknowledge the Department of Materials Science and Engineering for tolerance and understanding. I am truly grateful to Dr. Li Liu for the research guidance.

Finally, I would like to express my gratitude to my dear friends and colleagues for making my years at Texas A&M University a meaningful experience. I have met many challenges and difficulties at Texas A&M University. I am fortunate there are always people encouraging and helping me on the way.

Wish you all the best.

CONTRIBUTORS AND FUNDING SOURCES

Contributors

This dissertation work was supervised by dissertation committee chair Professor Hong Liang of the Department of Mechanical Engineering, committee members Professor Tahir Cagin and Professor Svetlana Sukhishvili of the Department of Materials Science and Engineering, and Professor Qingsheng Wang of the Department of Chemical Engineering.

All the research work conducted for the dissertation was completed by the student under the guidance and suggestions of Professor Hong Liang and Professor Zhengdong Cheng.

Funding Sources

This dissertation work was fully supported by the research assistantship and teaching assistantship at Texas A&M University. The research assistantship is from Mary Kay O'Connor Process Safety Center. The teaching assistantship is from the Department of Materials Science and Engineering, and the AggiE-Challenge Program of Texas A&M Engineering.

NOMENCLATURE

1D	One-dimensional
2D	Two-dimensional
3D	Three-dimensional
ZrP	Zirconium phosphate
DLS	Dynamic light scattering
TEM	Transmission electron microscopy
AFM	Atomic force microscopy
SEM	Scanning electron microscopy
POM	Polarized optical microscopy
SAXS	Small angle X-ray scattering
XPS	X-ray photoelectron spectroscopy
XRD	X-ray powder diffraction
FTIR	Fourier-transform infrared spectroscopy
TGA	Thermogravimetric analysis
LC	Liquid crystal
I	Isotropic
N	Nematic
S	Smectic
C	Columnar
Φ_I	Volume fraction point between I to I-N coexistent phase
Φ_N	Volume fraction point between I-N coexistent to N phase

h	Thickness of nanoplate
D	Diameter of nanoplate
ξ	Aspect ratio
P	Polarizer
A	Analyzer
E	Electric field
B	Magnetic field
GQD	Graphene quantum dot
DI	Deionized
PhC	Photonic crystal

TABLE OF CONTENTS

Page

LIST OF TABLES

LIST OF FIGURES

Page

CHAPTER I

INTRODUCTION

1.1 Two-dimensional (2D) colloids

Colloids are particles of size in a range of nanometer to micrometer dispersed in another continuous medium to form a relatively stable system. The lower limit of colloidal particle size is significantly larger than the size of the solvent molecule, so that the solvent molecule can be regarded as a continuous phase. One important property of colloidal particles is Brownian motion in the continuous phase, which determines the upper limit of the particle size. The thermal fluctuation movement of the solvent molecules makes the particles move in a random manner, and can well prevent the rapid sedimentation of the particles. The colloidal particles and the solvent phases can be a gas phase, liquid phase or solid phase.[1-3] The colloidal particle sizes are larger than molecules and easier for optical observation. Moreover, since the inter-particle forces, sizes and shapes of colloidal particles are subject for control, it can be often considered as a model to study the mesoscopic world.[4-6]

Traditional colloidal particles include spheres (0D), rods (1D) and plates (2D). The distinct self-assembly characteristics of 2D colloids come from the shape anisotropy of the nanoparticles and bring materials' controllability and designability. In nature, there are a large number of 2D materials, such as clay, asphalt, protein octamer in organisms and red blood cells.[7-9] Besides, the advancement of modern materials, like the MXenes, Xenes, graphene, molybdenum disulfide, and α-zirconium phosphate (ZrP).[10] These nanoplate

materials are widely used in various research and industry fields due to their small aspect ratio, large specific surface area and excellent engineering performance.

The 2D colloidal particles could perform more distinct liquid crystal phase behaviors than 0D and 1D particles due to the shape anisotropy, as shown in Figure 1. A higher concentration of colloidal particles results in higher crystallinity and various liquid crystal phases. In addition, the smectic phase, which is easy to appear in 1D rod-shaped particles, is a long-time challenge for 2D nanoplate liquid crystals. It has only been observed in nanoplate liquid crystals with higher polydispersity.[11] Different from 1D liquid crystals, 2D nanoplate liquid crystals belong to a relatively new field.[12] Looking a good model to study the self-assembly of 2D materials and liquid crystals is a critical concern for 2D materials research.

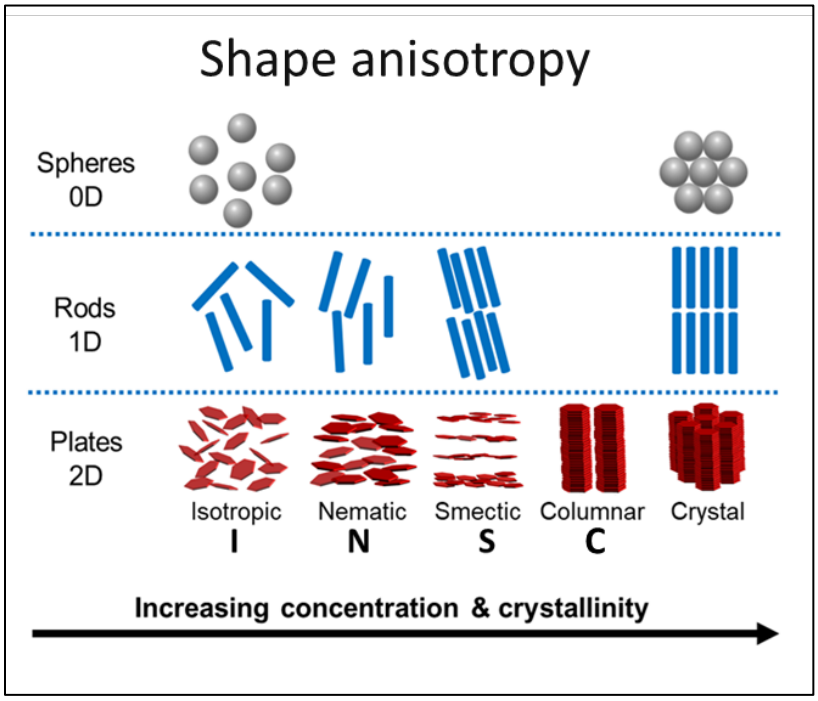

Figure 1. Self-assembly of various dimensions (0D, 1D, 2D) nanoparticles.

1.2 Liquid crystals

Liquid crystals have the characteristics of both crystal order and liquid fluidity. According to the conditions of formation, liquid crystals can be categorized into thermotropic liquid crystal and lyotropic liquid crystal.[13, 14] The appearance of the liquid crystal phase of the thermotropic liquid crystal depends on the temperature. When the temperature is in the liquid crystal phase interval of the composition, the liquid crystal phase will be formed in the sample. Lyotropic liquid crystals are liquid crystals formed by one or more anisotropic particles dispersed in a solvent. When the particles reach a certain concentration, a liquid crystal phase is formed.[15-17] In this dissertation study, liquid crystal in our system is a lyotropic liquid crystal.

1.2.1 Liquid crystal phases

As shown in Figure 2, the liquid crystals can be generally divided into the following nematic phase, smectic phase, columnar phase and chiral phase.

(a) Isotropic phase (I): Strictly, the isotropic phase (Figure 2a) is not a liquid crystal phase and does not have ordered nor anisotropic structures.

(b) Nematic phase (N): Generally, it is formed by 2D-shapes or 1D-shaped anisotropic particles. The structure is shown in Figure 2b. The particles have long-range orientational order while without positional order.

(c) Smectic phase (S): It is the same as the lamellar phase; as shown in Figure 2c, the molecules in the smectic layer tend to be in order, but there is fluidity between layers. It has 1D positional order.

(d) Columnar phase (C): The 2D nanoplate particles arranging in columns has higher order parameters than nematic phase, as shown in Figure 2d.

(e) Chiral phase: It is the same as the cholesteric phase. The particles are distributed in a nematic phase in every layer (Figure 2e). Unlike the smectic phase, the crystal orientation of each layer of liquid crystal is slightly twisted to form a spiral structure. A periodic structure is formed after 360° rotation.

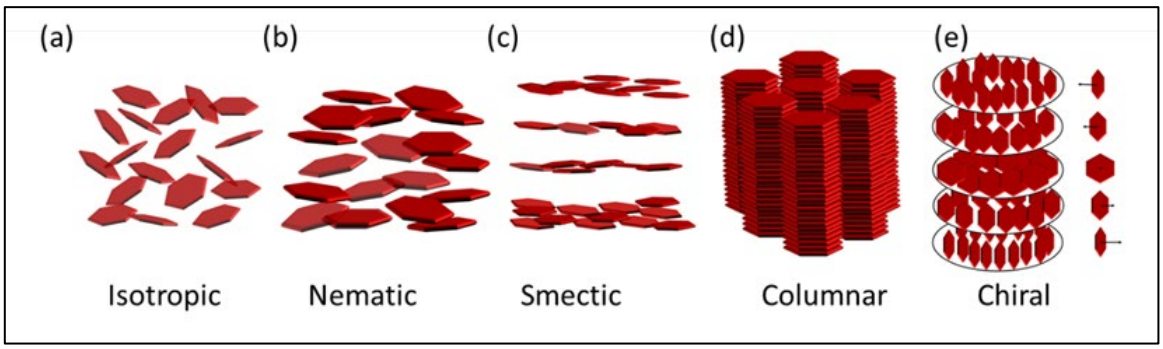

Figure 2. Liquid crystal phase classification.

1.2.2 Liquid crystal characterization methods

The characterization methods related to analyzing ordered structures usually could be utilized in liquid crystals study. The most traditional and basic characterization methods are testing through polarized light microscopy, small-angle X-ray scattering, differential scanning calorimetry and X-ray diffraction.

1) Polarized light microscopy

The liquid crystal samples were placed between two cross-polarizers for observation under the transmitted light. When the direction of the liquid crystal director is

consistent with the polarization direction of the analyzer or polarizer, the light will be blocked and appears black. The texture of the liquid crystal is the product of the collection of defects in the liquid crystal. Defects are caused by the breakdown of the symmetry of the liquid crystal structure. The texture is formed by the collection of defects, which is the primary feature of the liquid crystal structure. The polarized optical microscope can be used to study real-time phase transitions of liquid crystal phases, textures and defects.

2) Small angle X-ray scattering (SAXS)

When X-rays irradiate the surface of a substance, the difference in the electron density of the substance will cause X-ray scattering. The microcrystalline structures of colloidal particles are often measured through small angle X-ray scattering (SAXS). When a beam of extremely fine X-rays irradiates a layer of ultrafine powder, the electrons in the powder particles will scatter the X-rays, and the X-rays are dispersed in a small area near the original beam. The intensity of the scattering can reflect the size and distribution of the particles. We can use small-angle X-ray scattering to achieve the internal structures like the size of colloidal particles, the distribution of particles and the structure of the interface. Colloidal liquid crystal is generally a homogeneous system formed by uniform mixing of two or more phases. There are apparent differences in the electron density within the system. SAXS can be used to study the liquid crystals' orientation structure and is one of the most important methods to determine different liquid crystal phases.

3) Differential scanning calorimetry (DSC)

DSC is a thermal analysis method for measuring the power of heat as a function of temperature under the controlled temperatures. It is measured as the sample and reference change of heat power. Multiple parameters like specific heat, phase transition heat, phase diagram transition point, reaction rate and crystallinity and sample purity. The DSC method has a wide reaction temperature range, high resolution and small sample amount advantages. It is suitable for various inorganic and organic chemistry analysis. For liquid crystal study, it is a useful technique of investigating thermotropic and lyotropic liquid crystal phase transition temperature.

4) X-ray diffraction (XRD)

The structure of the crystal is that the atomic elements are arranged in an orderly three-dimensional space. The X-rays scattered by different atoms interfere with each other, resulting in strong X-ray diffraction in certain specific directions. The intensity of the diffraction fringe and the position of the spatial distribution are closely related to the results. Different crystal structures have various diffraction fringes. The pattern of diffraction fringes can reflect the spatial arrangement of atoms in the crystal. XRD was used to characterize the colloidal liquid crystal to get a diffraction pattern. The higher order of the liquid crystal will result in higher and sharper peaks of the diffraction pattern.

1.3 2D colloidal liquid crystals

1.3.1 2D nanoplate liquid crystals

Anisotropic 2D nanoplate particles can form liquid crystals. In 1938, Langmuir observed the liquid crystal behaviors of 2D clay particles. Then Onsager proposed a theory that predicted the ability of cylindrical objects with diameter D and height h to undergo liquid crystal phase transition through the volume repulsion between hard-core particles.[18-20] His theory was based on the nanoparticle repulsive volume. For 1D nanoparticles, the aspect ratio should be large and for 2D nanoparticles aspect ratio should be small.

Figure 3 represents one simulation model for nanoplate phase diagram,[21] which the aspect ratio is $\xi = \mathrm{h(thickness)/D(diameter)}$. From the simulation model results, the I-N transition requires high anisotropy of particles and low aspect ratio for nanoplates. Also, the concentration increase will result in long-range orientational order. The molecular ordering is to maximize packing entropy and minimize excluded volume. And the relative low polydispersity can increase the arrangement ordering. And it is clear to observe that nanoplates are easier to reorientate and form ordered nematic or columnar liquid crystal phases at smaller aspect ratios with lower concentration.

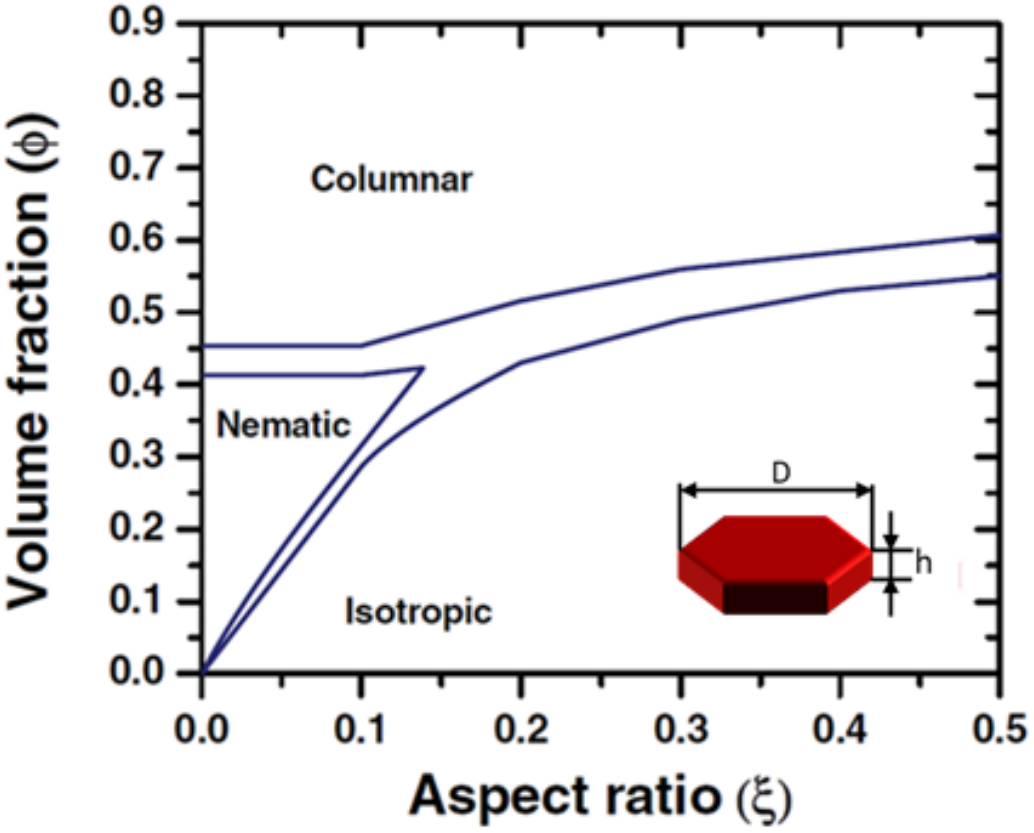

Figure 3. The phase diagram of nanoplate liquid crystals calculated by simulation.[21]

2D nanoplate liquid crystal phase transition is still a relatively new research field comparing with 1D rod liquid crystal. Although various discotic liquid crystal systems have been established, which mainly include clay suspensions, gibbsite, and the graphene oxide,[22-24] their polydispersity and large aspect ratio as shown in Figure 4 limit the materials to form higher concentration and more ordered structures (like smectic).

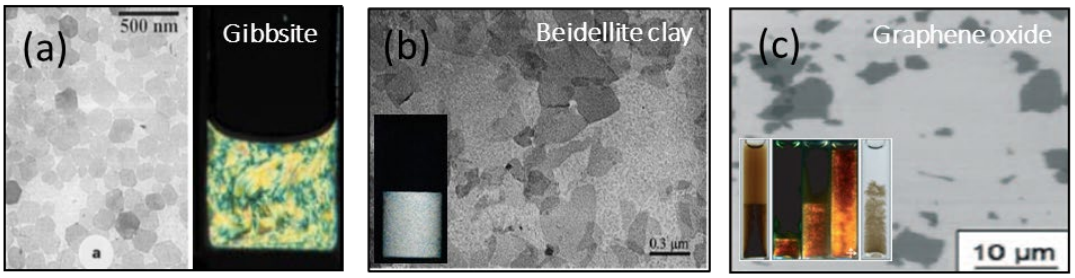

Figure 4. TEM image and photo of liquid crystals for common discotic liquid crystals. (a) Gibbsite, (b) Beidellite, (c) Graphene oxide.[22-24]

1.3.2 ZrP as 2D colloidal model

In general, the physical and chemical properties of the nanoplates have great influence on studying 2D colloidal liquid crystals. Aspect ratio, polydispersity, chemical stability, and surface charge impacting factors all should be considered.

Zirconium phosphate (α-ZrP or ZrP), working as a 2D material with controlled synthesis process,[25, 26] has great advantages of controllable morphology, particle size and stable crystal structures, as shown in Figure 5. It also has low polydispersity, not easy for forming gel, multiple reaction sites on the surface and small aspect ratio features. All these characteristics make ZrP involving broad research areas like flame retardancy, catalyst drug delivery, fuel cells, colloidal stabilizers and polymer composite additives.[27] It is worth noting that the diameters for ZrP nanoplates can reach 1800 nm and the thickness of monolayer ZrP nanoplates after exfoliation is 2.68 nm from our previous research work.[28, 29] So, the aspect ratio would be very small to 0.0015 and can form nematic liquid crystals at the very small volume fraction. It is a good study model for investigating self-assembly of 2D materials and liquid crystals.

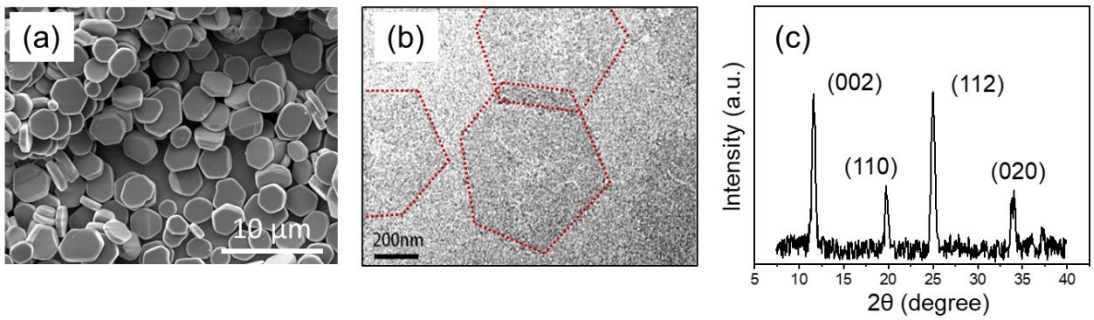

Figure 5. Characterizations of zirconium phosphate nanoplates.

1.3.3 ZrP synthesis methods

ZrP was synthesized with the reflux method in the early beginning with amorphous ZrP gel and phosphoric acid.[30, 31] Since then, many researchers have conducted extensive research on the synthesis of zirconium phosphate, columnar phosphate, phosphonate and its organic derivatives. Recently, Sun. et al. used the hydrothermal method to synthesize ZrP, they found that its particle size was positively correlated with the concentration of phosphoric acid and the synthesis reaction time. It could also be synthesized in other solutions, such as organic acid, ethanol or inorganic acid solution.[27, 32, 33] Traditional methods for synthesizing ZrP are discussed below.

1) Reflux synthesis method:

Mix the desired concentration of zirconium oxychloride octahydrate and concentrated phosphoric acid, and then transfer them to a three-necked flask with a reflux device to react for a certain period of time (24-48 hours). The reaction temperature is about 100 °C. The ZrP prepared by the reflux method has a small particle size (200-600 nm), low crystallinity, and high polydispersity.[34]

2) Hydrothermal synthesis method:

It is the simplest and most efficient method of adding the mixture of zirconium oxychloride octahydrate and phosphoric acid, and transferred to autoclaves. The reaction temperature is set to about 160-250 °C. The reaction time (5-168 hours) is used to synthesize ZrP crystals and its particle size is 500-2000 nm.[35]

3) Hydrofluoric acid (HF) synthesis method:

Mix the zirconium oxychloride octahydrate and phosphoric acid with a suitable concentration and volume, put HF into the autoclave and react at 110 °C for a fixed time. The particle size of the synthesized ZrP can reach 2000-3000 nm.[36]

4) Microwave-assisted synthesis method:

Adding the mixture of zirconium oxychloride octahydrate and phosphoric acid under vigorous stirring. The precursors were mixed homogeneously and added into the specific microwave synthesis adaptable container. It is under microwave irradiation at 150-200 °C at 250 psi for 1 hour. After the reaction, the later size of zirconium phosphate can reach 190-750 nm.[37]

CHAPTER II

MOTIVATION AND OBJECTIVES

2.1 Motivation and research

As discussed in Chapter I, high-anisotropic 2D nanoparticles belong to an emerging class of materials and have been widely discovered in nature and industry worldwide. Unlike 0D sphere and 1D rod, 2D materials like nanoplates have more anisotropies for forming oriented liquid crystal phases. In order to make the materials useful, it is critical to obtain an understanding of the morphology, properties and self-assembly of 2D materials & liquid crystals. The objective of this research is to develop novel synthesis procedures and new 2D materials with new functions and properties. Based on the processing, property, and performance of 2D materials, a fundamental understanding in effects of processing parameters on structures and performance will be achieved. To succeed, we use the novel 2D colloidal model system to study the self-assembly and liquid crystals phase transition behavior. ZrP nanoplates are chosen due to the controlled synthesis, stable morphology and small aspect ratio.

This research's four major objectives are addressed in the research flow chart in Figure 6 and elaborated below. (1) Development of synthesis methods of 2D ZrP nanomaterials and liquid crystals; (2) Study kinetics of ZrP liquid crystal phase transition with tunable internal aspect ratios; (3) Investigation of ZrP liquid crystal phase transition with external temperature fields; (4) Study the concentration effect on nematic photonic liquid crystal applications.

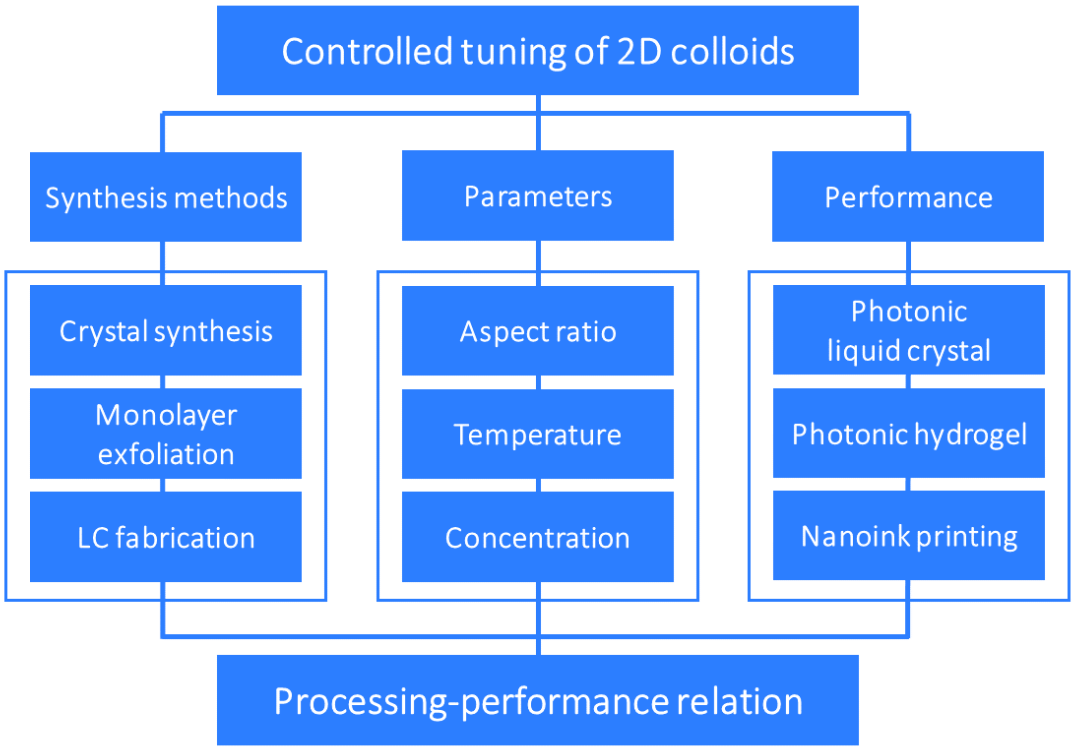

Figure 6. Research flow chart.

2.2 Research objectives

2.2.1 Development of synthesis methods of 2D ZrP nanomaterials and LCs

Various synthesis approaches like hydrothermal, reflux and microwave methods are utilized for synthesizing 2D ZrP layered crystals. The monolayer ZrP can be achieved through vigorous sonication and exfoliation after adding tetrabutylammonium hydroxide solution. The ZrP liquid crystals are fabricated by preparing the monolayer ZrP suspensions and characterized for next-step experimental use.

2.2.2 Study kinetics of 2D LC phase transition with tunable internal aspect ratios

The internal property of nanoparticles significantly affects the self-assembly of the materials. Here, the aspect ratio of 2D ZrP liquid crystal is investigated to study the nucleation and growth kinetics of isotropic-nematic phase transition. The larger aspect ratio of ZrP nanoplate liquid crystals would be considered higher the I-N phase transition starting point Φ_I. Moreover, a larger aspect ratio or smaller sizes of 2D liquid crystals result in higher Brownian motion rate and a higher I-N phase transition rate. Herein, the larger aspect ratio nanoplates will form oriented structures quicker and easier to achieve I-N phase transition.

2.2.3 Investigation of 2D LC phase transition with external temperature fields

Controlling self-assembly of 2D colloids through external forces is essential to materials research. Unlike ordinary magnetic fields or electric fields, tuning orientation of 2D materials through temperature gradient fields is rarely discussed. An external temperature gradient field to different nanoplate suspensions in isotropic and nematic phases was applied. It can be effective in controlling nematic liquid crystal arrangements and growth in nanoplate suspensions. The external temperature field and thermophoresis might move the 2D colloidal particles and reorientate the nanoplates to nematic or higher-ordered structures, which would be useful in materials transporting research areas at varying temperature environments.

2.2.4 Study the concentration effect on 2D nematic photonic LC applications

The phase transition of the 2D ZrP liquid crystals is highly dependent of the nanoplate volume concentration. Certain short-ranged nematic orders of ZrP suspension showed a bright field under cross-polarizers, and performed structural colors due to nanoplate orientation. The nanoparticle arrangements and structural colors relation will be studied. The 0D and 2D photonic crystals with color-enhanced additives are fabricated, and the photonic applications like nano inks and photonic hydrogels are also synthesized for performing their optical characteristics.

2.3 Dissertation structure

The dissertation is organized as follows. Chapter I is the introduction of 2D materials and ZrP colloidal liquid crystals. The importance, novelty and challenges are discussed. Chapter II is the motivation and objectives for this research work. Chapter III is the materials and methods, which the synthesis methods of ZrP crystals, the exfoliation, the ZrP liquid crystal fabrication and characterization are investigated. The kinetics of internal nanoplate aspect ratio dependence of ZrP liquid crystal isotropic-nematic phase transition is discussed in Chapter IV. The external temperature fields dependence on the growth and motion of isotropic and nematic ZrP liquid crystals is presented in Chapter V. The ZrP nematic photonic liquid crystals and hydrogel applications are studied. Photonic color-based applications are discussed in Chapter VI. Conclusions and future recommendations for the ZrP colloidal liquid crystals and 2D materials are given in Chapter VII.

CHAPTER III

MATERIALS AND METHODS

3.1 Synopsis

In this Chapter III, the synthesis methods of 2D colloidal ZrP liquid crystals are discussed. The ZrP synthesized in the dissertation is α-zirconium phosphate (α-ZrP). Three research work was focused in this chapter. First is the ZrP layered crystal synthesis with hydrothermal and reflux methods. The second is that ZrP monolayer intercalation and exfoliation. The third is the ZrP liquid crystal fabrication. Since ZrP has multiple research advantages and industrial applications the controlled growth of ZrP crystals and liquid crystals will be beneficial for 2D model systems.

3.2 Materials and instruments

Zirconyl chloride octahydrate ($ZrOCl_2 \cdot 8H_2O$), tetrabutylammonium hydroxide ($C_{16}H_{37}OH$, TBAOH) were purchased from Sigma-Aldrich. The phosphoric acid (H3PO4), Ethanol (200 Proof, C_2H_5OH) were purchased from Fisher Scientific.

The morphologies of nanoparticles could be imaged through a Quanta 600 field emission scanning electron microscopy (FESEM). The thin monolayer nanoparticle samples could be imaged through JEOL 2010 transmission electron microscopy (TEM) and FEI TECNAI G2 FE-TEM. The SEM samples were sputter coated to 3-5 nm thickness Pt/Pd alloy. The size distribution of particles and thickness was tested through Bruker

Dimension Icon AFM. The Malvern ZetaSizer NANO NS-90 was used for dynamic light scattering (DLS) testing to measure the average size of nanoparticles and size distribution.

The absorption and reflectance spectra were conducted with the Hitachi U-4100 UV-Vis high-resolution spectrophotometer. The photoluminescence intensity was measured with the PTI QuantaMaster series spectrofluorometer. The X-ray photoelectron spectroscopy (XPS) spectra of composition and element chemical state were obtained by Omicron's DAR 400 series XPS system with Mg kα radiation. The microwave-assisted reactions were running with the Discover SP microwave synthesizer (CEM Corporation). Nanoparticles could be tested with thermogravimetric analysis (TGA) through TA Instruments Q500 to quantify materials surface coverage grafting on the surface.

3.3 Experimental

3.3.1 Hydrothermal synthesis method for ZrP crystals

6 g zirconyl chloride octahydrate ($ZrOCl_2 \cdot 8H_2O$) was first dispersed in 12 mL deionized (DI) water in a 200 mL beaker. 48 mL of 15 M (15 mol/L) phosphoric acid was dropwise added into the $ZrOCl_2$ solution under continuous stirring. The mixture (12 M) was poured into the 80 mL Teflon-lined pressure vessel and the vessel was placed into hydrothermal autoclave composed of stainless-steel shell and lid, pressure plate and was heated in convection oven at 200 °C for various hours (10-40 hours). The hydrothermal autoclave was cooling down 8 hours to room temperature. ZrP nanoplate crystals were collected in 50 mL centrifuge tubes, and utilized centrifuge to wash with water and ethanol several times to remove the residue acid. The ZrP crystals were then dried in oven at 75

°C overnight and then use a pestle and mortar for grinding to achieve dried ZrP nanoparticles.

3.3.2 Reflux synthesis method for ZrP crystals

The ZrP nanoplates were synthesized by reflux method. 6 g zirconyl chloride octahydrate was added to a 250 mL bottom round flask. Then 12M phosphoric acid (12 mL 15M H_3PO_4 and 48 mL H_2O mixture) was refluxed at 94 °C. The intermediate product went centrifuging and was washed with DI water and ethanol at least three times to remove residue acids and then dried for 12 hours at 75 °C and mortared to obtain fine ZrP powder particles.

3.3.3 Microwave synthesis method for ZrP crystals

The microwave-assisted synthesis was performed in the Discover SP microwave synthesizer. 3 g $ZrOCl_2 \cdot 8H_2O$ powder was placed into 30 mL 15 mol/L phosphoric acid in the 50 mL centrifuge tube, and stirred 10 min for homogeneous mixing. 5 mL solution above was transformed to a 10 mL microwave glass vessel and 6 glass batches were achieved. Various glass vessel batches can react once a time and transfer automatically with Discover SP autosamplers when one reaction batch is ready. The microwave irradiation reaction was setting at 170 °C, 100 W under 1 hour. The products were washed with DI water 4 times and went through centrifuging to remove unreacted H_3PO_4. The washed samples were set in the oven 24 hours at 75 °C for complete drying and were grinding into white powders.

3.4 Exfoliation of layered ZrP crystals

1 g dried ZrP in 10 mL of DI water in a 50 mL centrifuge tube. 2.2 mL of TBAOH was dropwise added and vortexed for at 2 minutes. The suspension was sonicated for 1 hour and leave for 2-4 days (hydrothermal method 2 days, reflux method 3-4 days) to allow complete intercalation of TBA^+ ions and complete exfoliation of ZrP crystals. The resulting materials include large amount of ZrP monolayer and small amount of unexfoliated sample, so 15 minutes high centrifuge speed was performed several times to remove macroscopic unexfoliated sample in the bottom of the centrifuge tubes. The mother suspension was herein achieved and it was the basis of preparing all phase diagrams of liquid crystals.

Another thing needed to be paid attention to was that the smaller particle size of ZrP would be easier to perform high polydispersity (> 30%) after TBA exfoliation, which would reduce the optical performance of the 2D liquid crystals. Therefore, we let the ZrP I-N coexistence liquid crystals samples in centrifuge tubes automatically stand still 3 days to fractionate with gravity. Then the ZrP suspension would perform generally three layers during the I-N phase separation, which were top layer, middle layer and bottom layer. The relatively smaller diameters of nanoplates would be on the top of the suspension, the relatively larger diameters of nanoplates would be on the bottom. And the middle layer was I-N coexistence layer. We used pipette to remove the isotropic ZrP in top layer and collected the nematic ZrP in the bottom layer. Then we diluted the nematic ZrP suspension with DI water again and waited for another 3 days for next round I-N phase separation, and then achieved new nematic ZrP suspension. The process could be repeated several

times to prepare the monolayer ZrP liquid crystal suspension with lower polydispersity. Smaller polydispersity of ZrP liquid crystals would perform better optical liquid crystal performance under polarized optical microscope.

3.5 Fabrication of monolayer ZrP liquid crystals

The mother suspension has high volume fraction of monolayer ZrP nanoplates. When other volume fractions of liquid crystals need to be prepared, the volume fraction Φ_{ZrP} of mother suspension was defined through the equation below and then diluted with water to get the desired volume fraction.

$$\Phi_{ZrP} = 1 - V_{H2O} = 1 - \frac{m_{initial} - m_{final}}{\rho_{H2O} V_{initial}} \quad (1)$$

The detailed method for determining Φ_{ZrP} of mother suspension was shown below. The volume $V_{initial}$ of ZrP suspension was taken and measured the weight $m_{initial}$. Then the ZrP suspension was placed into an 75℃ oven overnight to remove solvent water. The residue ZrP suspension was weighted m_{final}. V_{H2O} was the water volume fraction, ρ_{H2O} was the water density. So, the mother suspension ZrP volume fraction was calculated by the above equation.

Φ_{ZrP} of mother suspension was diluted with DI water to make liquid crystal phase diagrams. For example, one ZrP mother suspension has the volume fraction of 11.0 %. The pipette was used preparing total 1 mL ZrP suspensions with 9 different volume fractions (data collected in Table 1) in glass vials. The ZrP suspension volume fractions were calculated by V1 and V1+V2=1000 μl. The glass vials were arranged in a line with

the increasing concentration orders from 0.025 to 0.095 (left to right), as shown in Figure 7.

Table 1. Amount of mother suspension and DI water for ZrP liquid crystal phase diagram.

No.	ZrP volume fraction	V1: Volume of ZrP mother suspension (μl)	V2: Volume of DI water (μl)
1	0.025	230	770
2	0.029	260	740
3	0.044	400	600
4	0.048	440	560
5	0.054	490	510
6	0.058	530	470
7	0.073	660	340
8	0.087	790	210
9	0.095	860	140

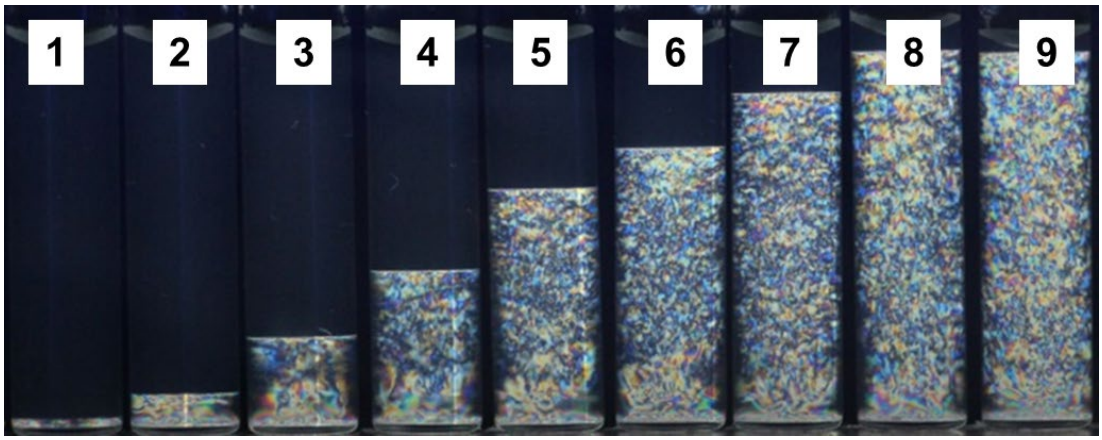

Figure 7. Polarized images of ZrP liquid crystals with various volume fractions.

3.6 Characterizations for ZrP liquid crystals

Apart from the common characterization methods POM, XRD and SAXS discussed in Chapter I, there are other characterization methods could be utilized in nanoparticle liquid crystal study, which were shown in Figure 8. The morphologies of nanoparticles and composites could be imaged using field emission scanning electron microscopy (FESEM) and transmission electron microscopy (TEM). The size distribution and thickness of particles could be tested through Bruker Dimension Icon AFM. Dynamic light scattering (DLS) could be used for measuring nanoparticles and size distribution.

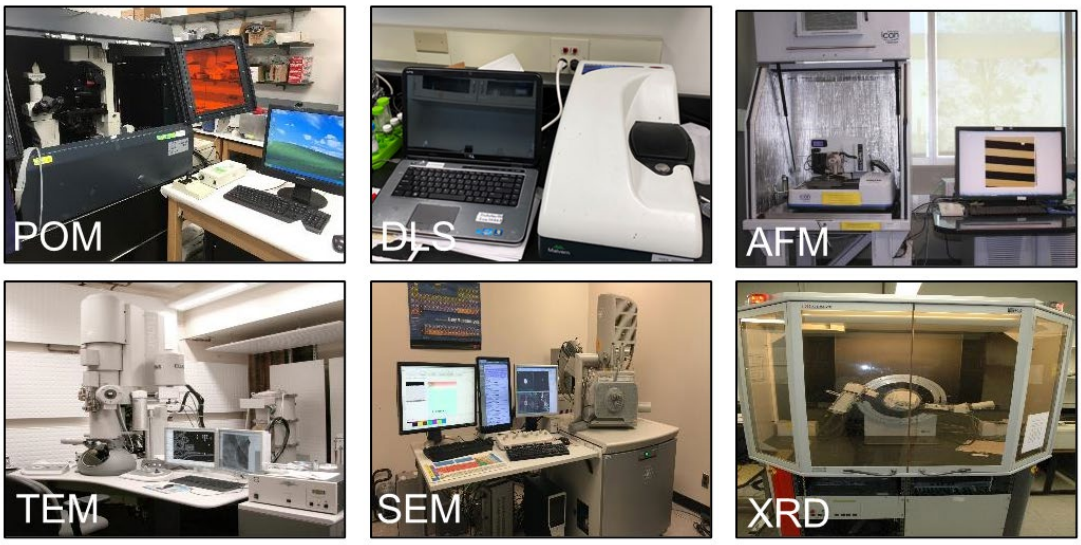

Figure 8. Photographs of common characterization methods for liquid crystals of nanoparticles.

Five ZrP crystals have been synthesized and exfoliated, which are Sample A (12M-reflux-6hr), Sample B (12M-hydro-10hr), Sample C (12M-hydro-20hr), Sample D (12M-hydro-30hr), Sample E (12m-hydro-40hr). Figure 9 presented SEM image of 12M reflux 6hr, 12M hydro 30hr and TEM image of 12M hydro 40hr. From the SEM and TEM images in Figure 9, ZrP synthesized from hydrothermal method have clearer and sharper crystal edges and exfoliation did not break the hexagonal shape of ZrP crystal. The sample made by reflux method has smaller size than that of hydrothermal method.

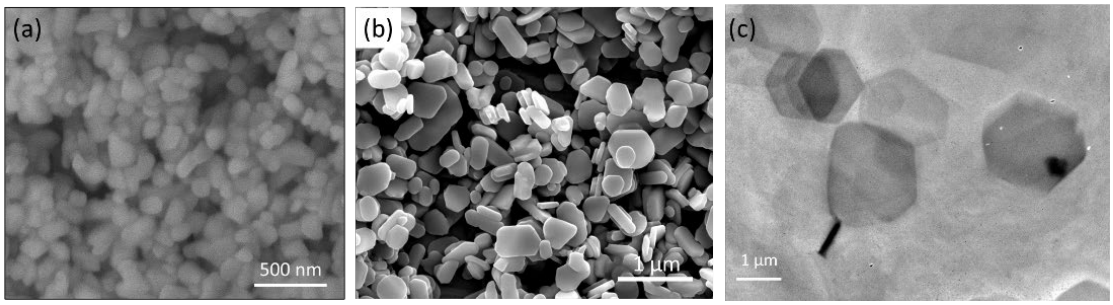

Figure 9. (a) SEM image of ZrP crystals (12M-reflux-6hr), (b) SEM image of ZrP crystals (12M-hydro-30hr), (c) TEM image of monolayer ZrP (12M-hydro-40hr).

The ZrP monolayer nanoplate after exfoliation was studied. The thickness of monolayer was measured with AFM from previous research work to be 2.68 nm.[28, 29] In this dissertation, we considered the thickness to be a constant. And the hydrodynamic diameter of monolayer ZrP could be measured by DLS instrument. The diameters were 169, 420, 583, 779 and 945 nm for sample A to E. The DLS data presumably of sizes of nanospheres and could be transformed to diameter of nanoplates by the equations below.

$$R_h = \frac{k_B T}{6\pi D_T \eta} \quad (2)$$

$$h = \frac{k_B T}{3\pi^2 \eta D_T} \frac{\arctan\left(\sqrt{\left(\frac{1}{\xi}\right)^2 - 1}\right)}{\sqrt{\left(\frac{1}{\xi}\right)^2 - 1}} \quad (3)$$

$$\xi = h/2R \quad (4)$$

R_h is the hydrodynamic radius, R is the nanoplate radius. D_T is the diffusion coefficient, η is the viscosity, and k_B is the Boltzmann constant. The lateral sizes of ZrP monolayer nanoplate could be calculated through the software, which will be discussed in detail in Chapter IV.

The schematic diagram of layered ZrP exfoliation was shown in Figure 10. As discussed in Chapter 3.4, tetrabutylammonium hydroxide (TBAOH) would release TBA^+ ions and first covered ZrP surface, and would like to intercalate into the inner layer of ZrP. So, more intercalation time and sonication will make TBA+ ions better enter the layered structure and complete exfoliation. As seen in Figure 11, the ZrP suspension will transform from opaque white to the translucent color and revealed flow-induced birefringence after exfoliation.

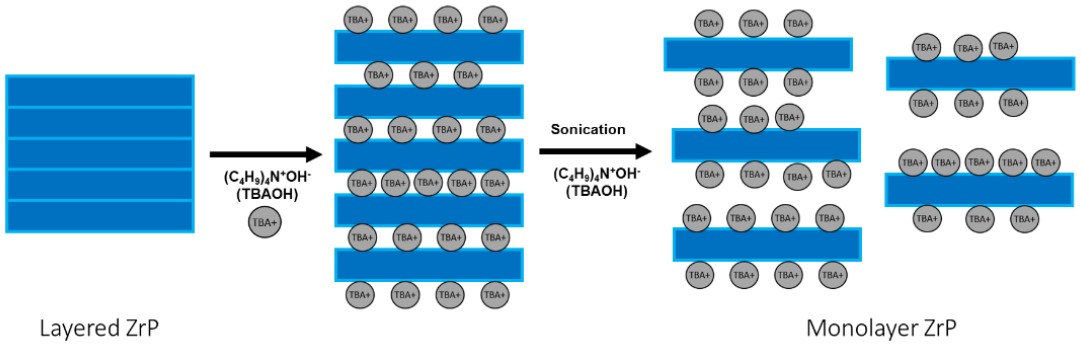

Figure 10. Scheme of exfoliation of layered ZrP using exfoliating agent TBAOH.

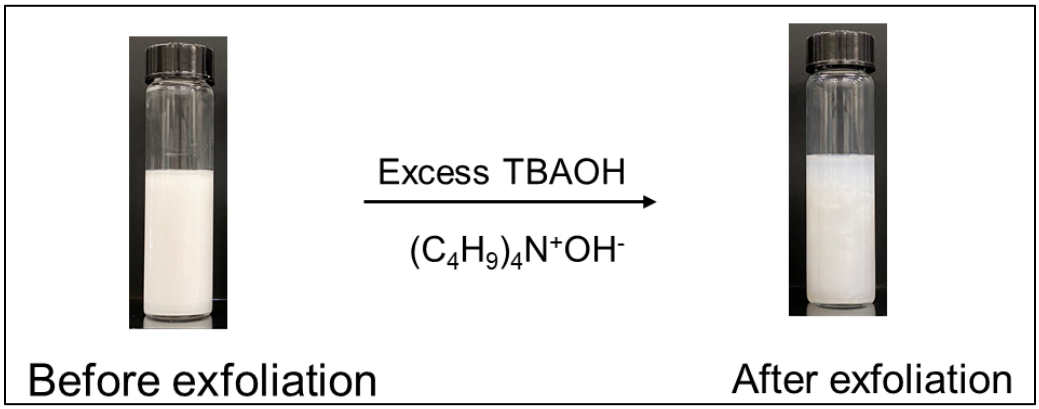

Figure 11. Photographs of ZrP suspension before and after exfoliation.

The experimental setup for observation of phase diagram was shown in Figure 12. Liquid crystal has the birefringence behavior, so the ZrP liquid crystal samples were placed between cross-polarizers for observation. When the light source is on, we can see bright part of liquid crystals in the vials are nematic phases, settling in the bottom and the

dark part in the vials are isotropic phase. The nematic volume fraction f_N is the ratio of nematic liquid crystals in the whole vials, which can be directly calculated.

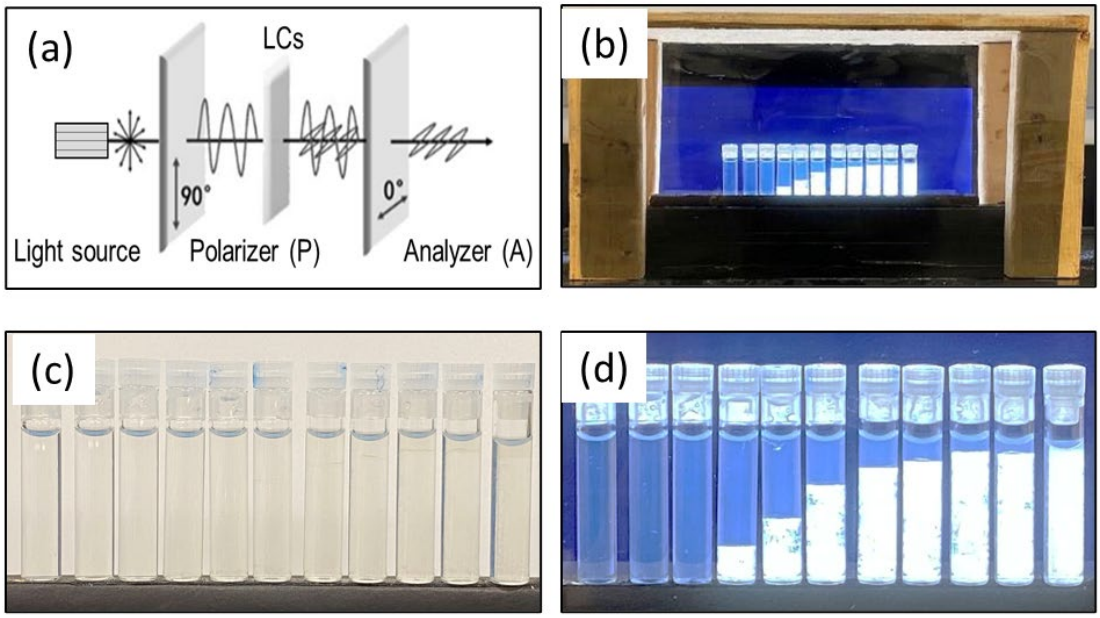

Figure 12. (a) Light pathway in the cross-polarizer stage. (b) Experiment platform for observation. (c) Image of liquid crystal sample vials without cross-polarizers. (d) Image of liquid crystals with cross-polarizers.

3.7 Summary

The controlled size, regular shapes and good crystal morphology of ZrP crystals and monolayer liquid crystals have been studied and synthesized. Hydrothermal and reflux methods for fabrication of ZrP layered crystals were used and various samples were prepared. In Appendix A, another synthesis way of microwave-assisted method of making ZrP crystals will be discussed. Then ZrP exfoliation has been applied and is the critical part for making monolayer ZrP mother suspension. ZrP liquid crystals fabrication and phase diagram making is the key point for studying the controllability of 2D colloids. The uniform and low polydispersity samples indicating and high consistency. The ZrP liquid crystal fabrication could be used in optical performance applications and can also work on flame retardancy, fuel cells, ion exchange materials and lubricants requiring controlled 2D monolayer structures.

CHAPTER IV

EFFECTS OF ASPECT RATIO PHASE TRANSITION, KINETICS OF NUCLEATION & GROWTH OF NANOPLATE LIQUID CRYSTALS

4.1 Synopsis

In this chapter, the phase transition dependence of the aspect ratio of nanoplate liquid crystals has been investigated. The crystallization and I-N phase separation of ZrP nanoplates with various aspect ratios is studied through the I-N phase transition starting point Φ_I and I-N phase separation time $t_{Nematic}$. The research findings indicate that larger aspect ratio nanoplates have larger Φ_I, it will undergo faster nucleation and complete I-N transition quicker.

4.2 Introduction

The colloidal system is an ideal model for studying the behavior of atoms.[38-41] For example, when the volume fraction of spherical glue increases, we can observe the crystallization process or glass transition process similar to the behavior of atoms in the suspension.[42, 43] The shape anisotropic particle colloidal system can produce liquid crystal phenomena and would be for studying liquid crystal phase transition. When the concentration of colloidal particles increases, the shape anisotropic particle colloidal system first undergoes the transformation from isotropic phase to nematic phase. The study of the kinetic properties of colloidal suspensions can not only enable us to have a deeper understanding of suspensions, but also develop its potential practical value.

Spherical colloidal particles have thermodynamic properties similar to atoms or molecules due to Brownian motion, and the interaction potential between colloidal particles can also be similar to the interaction potential between atoms. Therefore, people often reveal the dynamic properties of the atomic system by studying the movement and crystallization process of large-scale colloidal particles.[3, 42] In the kinetic study of spherical particles, it has been observed that the volume fraction of particles and the polydispersity of particle size play a key role in the kinetics of spherical colloidal systems. When the particle concentration is less than the melting concentration, the nucleation and crystallization process of a single crystal can be observed; and when the particle concentration is higher than melting concentration, the nucleation of the crystals is related to each other and is no longer independent, and the nucleation rate is accelerated and high nucleation rate inhibits the growth of crystals.[44] The polydispersity affects the nucleation of colloidal particles, the greater the polydispersity, the longer the nucleation time of the particles.[45]

Few research works have been studied on the phase separation rate of 2D nanoplate liquid crystals. As can be seen, the internal aspect ratio of nanoplates plays an important role in the phase change process.[46] The Onsager theory[18] discussed in Chapter I for anisotropic colloidal particles has predicted that 2D nanoplates with smaller aspect ratios would form ordered structures like nematic liquid crystals phase at smaller concentration. For industry production, it needs relative faster self-assembly formation rate for 2D nanoplates. But the smaller aspect ratio of nanoplates might result in slower efficiency of production and applications. So, finding an optimistic aspect ratio parameter of nanoplates

liquid crystals would greatly benefit for understanding the kinetics and improving the performance of 2D colloidal applications.

4.3 Experimental

Five nanoplate liquid crystal samples with different sizes were synthesized. The detailed synthesis and exfoliation methods were discussed in Chapter III. Withing all samples, Sample A was synthesized through reflux method and Sample B, C, D, E were synthesized through hydrothermal method. All samples went through the sonication and complete exfoliation process.

Table 2 recorded these 5 samples' lateral size (diameters) and aspect ratios. Sample A had the smallest size and largest aspect ratio. Sample E had the largest size and smallest aspect ratio. Dynamic light scattering (DLS) method was used here to measure the ZrP monolayer nanoplates. The hydrodynamic diameter data were 168.8 nm for sample A, 420.4 nm for sample B, 583.5 nm for sample C, 779.1 nm for sample D and 945.1 nm for sample E. Moreover, the polydispersity of ZrP suspension was also monitored. And all five samples' polydispersity were smaller than 0.20 for better optical observation of liquid crystals, which has been discussed in Chapter III.

The hydrodynamic diameters of ZrP suspension were measured from DLS and needed to transform to 2D plate lateral diameter. From the equations discussed in Chapter III below,

$$h = \frac{k_B T}{3\pi^2 \eta D} \frac{\arctan\left(\sqrt{\left(\frac{1}{\xi}\right)^2 - 1}\right)}{\sqrt{\left(\frac{1}{\xi}\right)^2 - 1}} \quad (5)$$

$$\xi = h/2R \quad (6)$$

Different 2D ZrP monolayer diameters and aspect ratios accordingly can be calculated through the software. The nanoplate diameters and aspect ratios were recorded below in Table 2.

Table 2. Aspect ratios of ZrP nanoplate suspension.

Sample List	Synthesis Method	Diameter (nm)	Aspect Ratio
Sample A	12M-reflux-6hr	265±37	0.0101±0.0014
Sample B	12M-hydro-10hr	660±78	0.0041±0.0005
Sample C	12M-hydro-20hr	916±120	0.0029±0.0004
Sample D	12M-hydro-30hr	1223±140	0.0022±0.0003
Sample E	12M-hydro-40hr	1481±135	0.0018±0.0002

Phase diagrams of five different samples were prepared for further use. The mother suspension was diluted with DI water for preparing various volume fractions of ZrP liquid crystals. All ZrP suspension samples were diluted to 1 mL and sealed in the glass vials. Every sample has a group of 9 vials with various volume fractions, which was recorded in

Table 3. There are five groups in total and the glass vials with different volume fractions were arranged in a line with the increasing concentration orders from left to right.

Table 3. Volume fractions of five different sizes of liquid crystals.

Diameter (nm) / No.	265±37	660±78	916±120	1223±140	1481±135
1	0.025	0.021	0.007	0.005	0.004
2	0.029	0.0244	0.0108	0.0086	0.006
3	0.044	0.0276	0.012	0.0094	0.0066
4	0.048	0.0308	0.0132	0.0102	0.0072
5	0.054	0.034	0.0156	0.011	0.0078
6	0.058	0.0404	0.0188	0.0142	0.0096
7	0.073	0.0468	0.0212	0.0158	0.0108
8	0.087	0.05	0.0244	0.019	0.0182
9	0.095	0.0532	0.0292	0.0238	0.0244

The morphology of ZrP nanoplates layered structures and monolayer structures were investigated. Figure 13 presented the electron micrograph images of pristine ZrP and monolayer ZrP after exfoliation (Sample D). As seen from SEM image in Figure 13a, the hexagonal shapes of ZrP nanoplates were clear and it was easy to differentiate single ZrP crystal. From the TEM image in Figure 13b, the ZrP layered crystals have been exfoliated and the exfoliation agent tetrabutylammonium hydroxide did not break the ZrP lateral

structures and retained the hexagonal shape. The diameter of nanoplates were measured through DLS and thickness was measured to be 2.68 nm from previous literatures.[47] Then the aspect ratio was achieved through thickness/diameter of nanoplate liquid crystals. Monolayer ZrP suspensions with various aspect ratios were fabricated. Five groups of samples were prepared with introduction of DI water to achieve the desired concentration. Different arrangement of liquid crystals like isotropic, nematic and coexistence phases were fabricated and set up in the vial for polarized optical imaging. The phase diagram of Sample A group was shown in Figure 14. Different nematic fractions of ZrP liquid crystal samples were measured and plot the phase diagram of nematic fraction vs volume fraction.

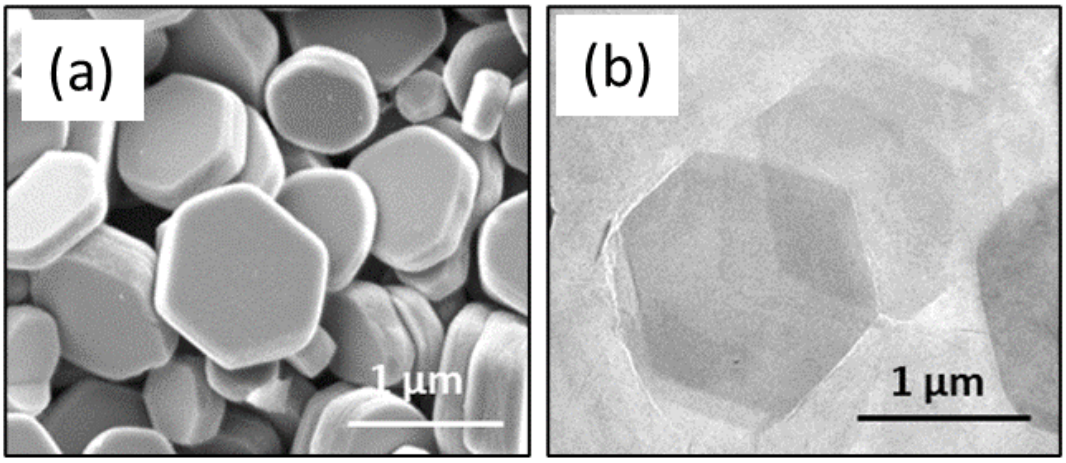

Figure 13. The morphology of ZrP of different layers. (a) SEM image of the pristine ZrP layered crystals, (b) TEM image of ZrP monolayer after exfoliation.

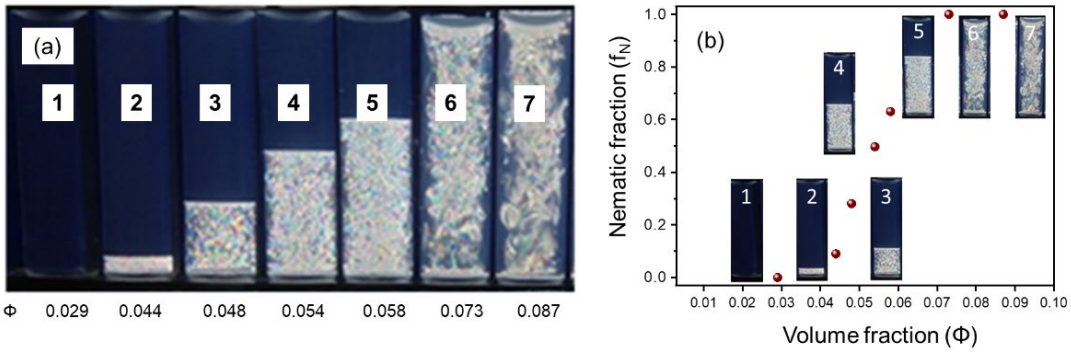

Figure 14. Polarized image (a) and phase diagram (b) with different volume fractions of Sample A liquid crystals.

4.4 Results and discussions

Volume fraction Φ=0.048 of sample A has been prepared for observation of I-N phase separation time. Here, Sample A suspension was studied, which had largest aspect ratio of all 5 samples. Initially, the homogenized sample started to settle down with time and presented nematic phases under cross polarizers. The sample nucleated nematic liquid crystals or called droplets tactoids. It would grow accompanying with time. At the same time, the nanoplates would start to deposit and sediment because of the gravity effect. From the snapshots, the sample started from metastable state, went through nucleation, growth, sedimentation and reached equilibrium. In the end, the nematic tactoids completely deposited to the glass vial bottom. The interface between isotropic and nematic phase appeared and the time was recorded to be 840 min. Herein the complete I-N phase separation ($t_{Nematic}$) from the start to the clear interface shown was defined. The bottom nematic phases of ZrP would not form more and the I-N liquid crystals have reached the equilibrium. Figure 15 is the schematic illustration for the ZrP liquid crystals

sedimentation and phase transition process. Then phase diagram of kinetics for I-N separation in sample A to sample E suspensions were performed.

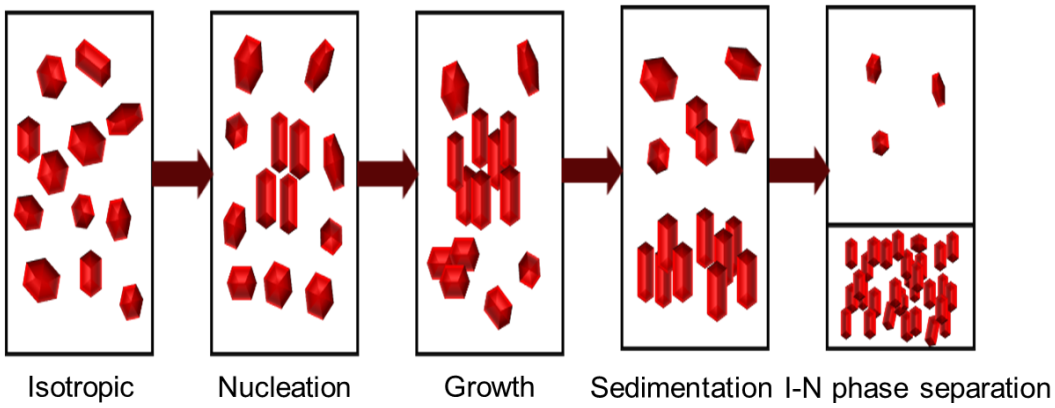

Figure 15. The schematic diagram of I-N phase transition process of nanoplate liquid crystals.

The I-N phase transition diagram of ZrP liquid crystals with different aspect ratios (Sample A, B, C, D, E) was shown in Figure 16. It was clear that as the aspect ratio of the ZrP nanoplates increases, the I-N phase transition concentration Φ_I also increase. This could be explained based on the influence of the aspect ratio effect of nanoplates on phase transition. According to the theoretical simulation results of Bates on the influence of the aspect ratio on 2D colloidal suspension, the smaller aspect ratio of nanoplates have higher orientation order [48] compared with ones have larger aspect ratio at the same concentration. The colloidal suspension of discs with smaller aspect ratio will first reach Φ_I. As we considered the thickness is certain to be 2.68 nm, the aspect ratio decreases with increasing nanoplate size. Smaller aspect ratio Sample E has higher orientation order and will start I-

N phase transition first. Increasing the aspect ratio of ZrP liquid crystals will increase Φ_I accordingly.

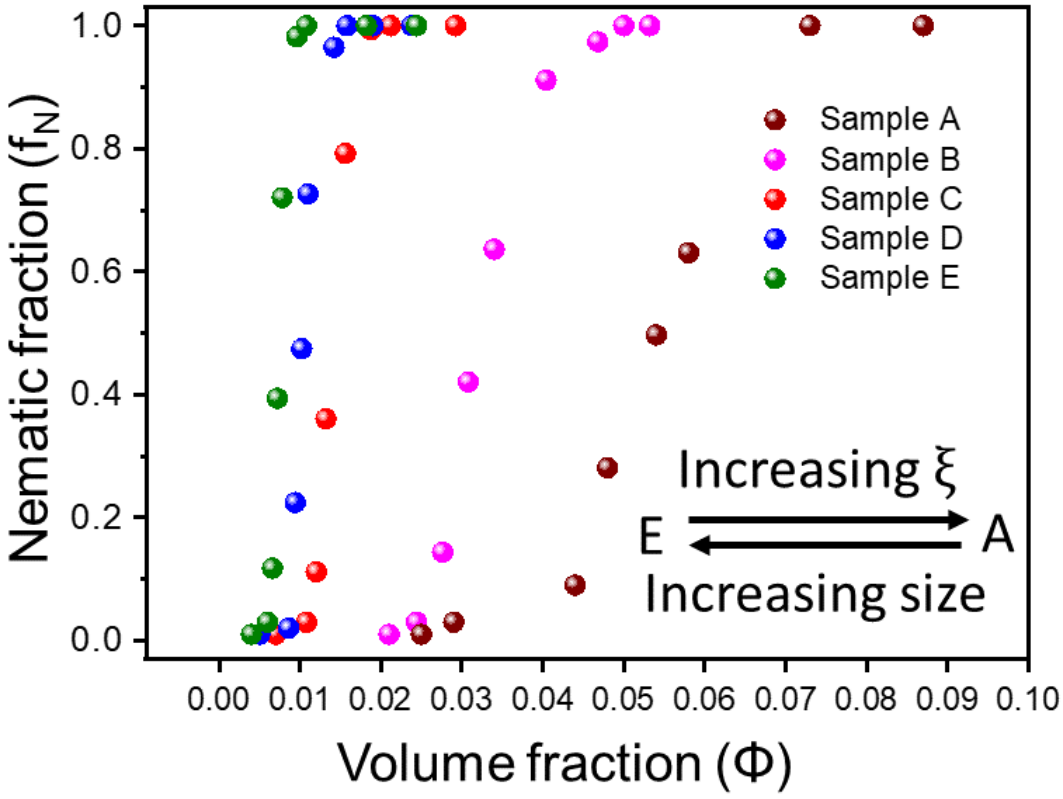

Figure 16. The nematic fraction of Sample A, B, C, D, E as a function of volume fraction Φ.

The I-N phase separation time t_N of 5 samples were recorded and plot as a function of accordingly aspect ratios. The relation of the I-N phase separation time $t_{Nematic}$ and the aspect ratio of ZrP liquid crystals were plotted as shown in Figure 17. $t_{Nematic}$ decreased with the increment of aspect ratio. The reason might be that larger aspect ratio is accompanying with smaller size. The rate of Brownian motion will be quicker and would

be easier to form ordered oriented structures and form new liquid crystal phases, so it will perform I-N phase transition quicker.

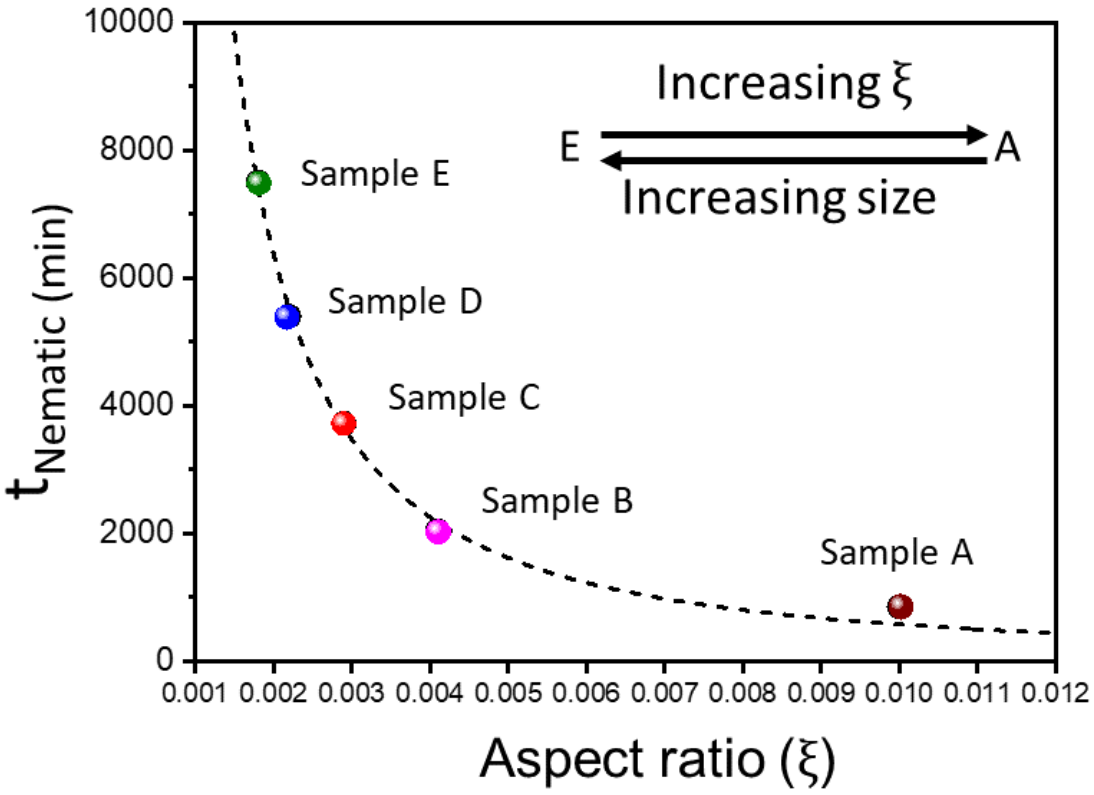

Figure 17. The I-N phase separation time $t_{Nematic}$ as a function of ZrP nanoplate liquid crystal aspect ratios.

4.5 Summary

To conclude, in this chapter, we have studied the internal aspect ratios of 2D ZrP nanoplates dependence of the liquid crystals phase transition. The larger aspect ratio of ZrP nanoplate liquid crystals would result in the larger the I-N phase transition starting point Φ_I. The I-N phase transition rate of the ZrP nanoplate liquid crystals will increase at smaller nanoplate lateral size or larger aspect ratio. This finding offers a method to tune 2D materials performance through adjusting their aspect ratios.

CHAPTER V

CONTROLLED GROWTH OF 2D LIQUID CRYSTALS UNDER EXTERNAL TEMPERATURE FIELDS[*]

5.1 Synopsis

Controlling self-assembly of 2D colloids through external forces is essential to develop modern electrooptical and biomedical devices. In this chapter, we demonstrated that an external temperature field can be effective in controlling nematic liquid crystal order and growth in nanoplate suspensions. Suspensions of nanoplates with isotropic or nematic arrangements, could be effectively moved using a temperature gradient environment causing a phase transition to liquid crystal nematic phase. Such controllably formed nematic phase featured large nematic monodomains and enabled topologically more stable structures that were evident from the absence of hedgehog-type defects which are typically found in nematics formed spontaneously via nucleation and growth mechanism in a sufficiently high concentration suspension of nanoplates. Due to their high surface area-to-volume ratio and excellent thermophoretic properties, nanoplates can prove to be an ideal candidate for biomolecules transporting through temperature varying environments.

[*] Part of this chapter is reprinted with permission from "Growth of colloidal nanoplate liquid crystals using temperature gradients for offshore oil spill treatment." by Shinde, A*., Huang, D*., Saldivar, M., Xu, H., Zeng, M., Okeibunor, U., Wang, L., Mejia, C., Tin, P., George, S. and Zhang, L., Cheng, Z., 2019. *ACS nano*, 13(11), pp.12461-12469 (*equal contribution). Copyright 2021 by ACS Publications.

5.2 Introduction

Dynamic control of the self-assembly of anisotropic colloids such as nanorods and nanoplates can be realized by using external electric and magnetic fields.[49-55] The excellent electric field response of graphene oxide flakes can be useful in electronic displays.[56] Very recently, fascinating materials mimicking nature's rare arrangements such as the structure colors were fabricated using nanoplates such that their colors could be tuned by using external fields.[57, 58] Electric and magnetic fields thus allowed control on the orientation of the anisotropic colloids. However, there are limitations in controlling colloid concentration or creating their gradients with electric and magnetic fields. Control of colloid concentration can potentially enable establishing the directional control on the growth of the colloidal soft matter phases.[59]

To overcome the challenge, external temperature fields could be thought of as an effective method that allows controlling colloid concentrations through transport mechanisms involving thermophoresis and natural convection. As thermal temperature gradients have already been found to be useful in many applications involving colloidal dispersions such as isotope separation,[60] nuclear fusion in ionized gas,[61] particle separation,[62-65] optothermal trapping,[66] and growth of colloidal single crystals.[67] Among a rich variety of soft matter phases, nematic liquid crystal is in the focus of many intensive interdisciplinary studies.[68] Inherent phenomenon of natural convection associated with using thermal gradients can also be seen to be widely used industrial applications, such as solar collectors,[69] furnaces,[70] building heating and cooling system.[71] Previous experimental,[72] computational[73] studies on nanofluids convection as well as those

involving combination of thermophoresis and natural convection[74, 75] were found helpful for the presented research.

We have designed an experiment using temperature field with continuous temperature gradient to successfully drive nanoplates to one end of the sample and thereby control the formation of the nematic phase. The colloidal nanoplate nematic phase in this study can be considered as a soft matter analog of biological thermophilic micro-organisms that prefer to go to the warm region. The idea of nematic phase growing at higher temperature regions is somewhat counterintuitive because conventionally in thermotropic liquid crystal systems, the nematic phase growth happens as the temperature is reduced. Our findings in this study complement our recent research interest in developing stimuli responsive soft matter systems.[55, 76]

When a colloidal suspension is placed in a temperature gradient, the dispersed particles are driven out of equilibrium. Considering convection and the particle flux due to temperature gradient can be explained by the equation below,[77]

$$J = -\Phi D_T \nabla T + D\nabla\Phi + \Phi v \quad (7)$$

where Φ is the local volume fraction of colloids in the sample, D is the translational diffusion coefficient of colloids, D_T is the thermophoretic mobility, T is the absolute temperature and v is the particle velocity due to fluid convection. Thermal inhomogeneity inside the thin layer of fluid in contact with colloids is considered to be responsible for thermophoresis.[78] The gradient of the solid-liquid interfacial tension parallel to thermal gradient creates an anisotropic pressure tensor near the particle's surface due to which the particle is pulled towards the direction of lower interfacial tension.[79]

Although most commonly found direction of thermophoretic motion is parallel to the temperature gradient, the thermophoretic drift of anisotropic colloids can have a nonzero component in the direction perpendicular to the temperature gradient.[80] Thermal response of the electrolyte plays a major role in the transport of charged colloids such that a change in the salt concentration could cause inversion of thermophoretic mobility D_T of charged colloids.[64, 81] The difference in thermophoretic mobilities of positively and negatively charged ions in solvent could lead to separation of charges in presence of the thermal gradient.[64] The resulting thermoelectric potential can generate a thermoelectric current and depending on the sign of charge on the colloids, they drift either to the cold or to the warm region.[82] The thermophoretic mobilities of individual ions in an electrolyte are determined by their solvation forces and concentration.[83]

Studies of non-spherical colloids in thermal gradients are rare. From a fundamental standpoint, one of the specialties of non-spherical nanoparticles is their ability to form soft structures of different symmetry, such as nematic, smectic liquid crystals at higher concentrations.[11, 84, 85] It is therefore possible to control the growth of soft phases of platelets, rods and board-like particles using external temperature gradients. Due to the slow and epitaxial-like growth, topological defect structures of external field-driven phases can be significantly different from those formed spontaneously at higher colloid concentration.

Physicochemical properties of charged colloids might affect their Soret coefficient ($S_T=D_T/D$). Since the solvation forces are dependent on temperature, many colloidal and biological systems show negative Soret coefficient below a certain temperature that is

typically known as the critical temperature.[64] In polystyrene latex spheres, critical temperature was near about 4 ºC whereas in micellar solutions of non-ionic surfactant dodecyl maltoside, it was close to 43 ºC.[86] Thermophoretic mobility (D_T) of colloids was measured for polystyrene spheres and was found to be independent of the size of colloids[87] whereas the Soret coefficient was found to be proportional to particle surface area.[88] Recently, it was also shown that S_T depends on the average temperature of the temperature gradient environment.[89] In the limit of extreme dilution, the interactions between colloids can also be neglected; however, in concentrated colloidal suspensions, thermophoresis can be understood as the sum of single particle and collective effects.

Herein, we demonstrated control on the nanoplate concentration by applying a linear temperature gradient field to different nanoplate suspensions in isotropic phase and nematic phases, which in few hours leads to formation of nematic phase *via* crowding of nanoplates at the hot end of the sample. An increasing fraction of nematic liquid crystals towards the hotter region was indicative of positive density gradient towards the hot region. The colloidal nanoplates of zirconium phosphate show negative Soret coefficient in the temperature gradient ranging from 26 ºC to 42 ºC. Our study also demonstrated that 2D materials as nanoscale transporters through temperature gradient environments. Nanoplates can carry more amount of cargo due to higher surface area to volume ratio as compared to spheres. Due to the biocompatibility of the ZrP nanoplates in this experiment has been proven to be excellent,[90, 91] their use in biomolecular transport in medical devices is promising.

5.3 Experimental

The sample used in this experiment was sample A (12M-reflux-6hr). The detailed synthesis procedure was discussed in Chapter III. The experimental setup is schematically represented in Figure 18. It includes a transparent sapphire crystal plate as temperature gradient substrate, a sample microcapillary channel mounted on the substrate. A white light source was used as a backlight and the temperature gradient assembly was placed in between crosse-polarizers such that the temperature gradient is along the horizontal direction and the gravity direction points downwards in the Figure 18. A portable microscope was used for imaging.

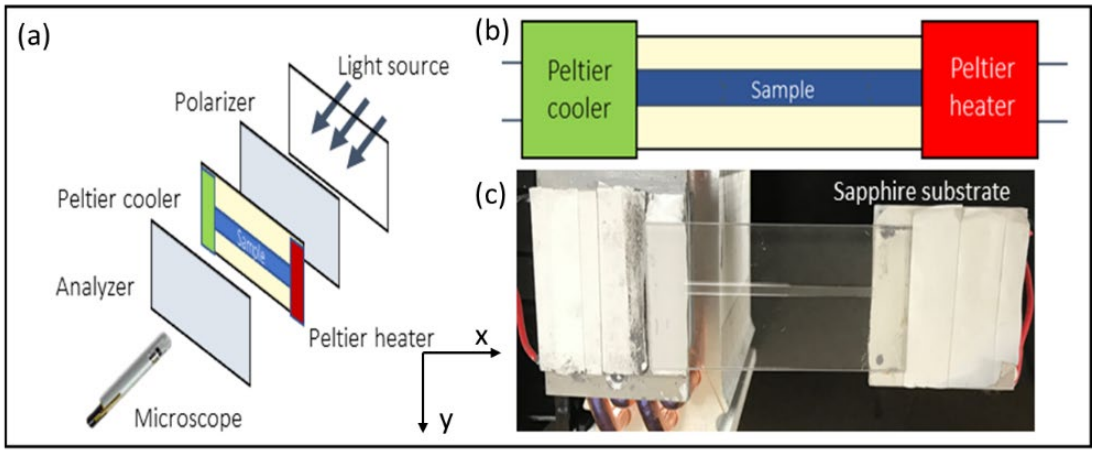

Figure 18. (a) Schematic drawing of the full experimental setup. (b) Scheme of the LC sample in temperature fields. (c) Photograph of the LC sample in the temperature fields. The setup was placed in XY plane with X direction pointing towards horizontal direction of increasing temperature and Y-direction was along gravity.

The sapphire crystal was chosen due to its transparent and temperature conductive properties. The sapphire crystal was purchased from Meller Optics Inc, being transparent with moderate thermal conductivity of 23 W/mK was a suitable candidate enabling setup of linear thermal gradient within several minutes, as shown in Figure 19. The two ends of the substrate were kept in touch with thermoelectric Peltier heating/cooling devices. Suspension of ZrP nanoplates was filled in flat rectangular capillary (Vitrocomm, Inc) having dimensions 50 mm x 2 mm x 0.2 mm and its two ends were sealed using UV-curing glue. A Peltier device has two surfaces. When voltage is supplied to the device, one of the surfaces gets heated and the other one gets cooled. By reversing the polarity of the external voltage, the hot and cold surfaces can be interchanged. If an appropriate heat sink is not provided to the hot surface, the device stops functioning. In this experimental setup, the hot surface of thermoelectric device on the right was touching the sapphire plate, which conducted heat to its other end and worked as a heat sink. The hot surface of the thermoelectric Peltier device on the left was kept in touch with an 8 mm thick metallic plate maintained at 5 ^{o}C using a cooling fan mechanism like that of computer CPU cooling.

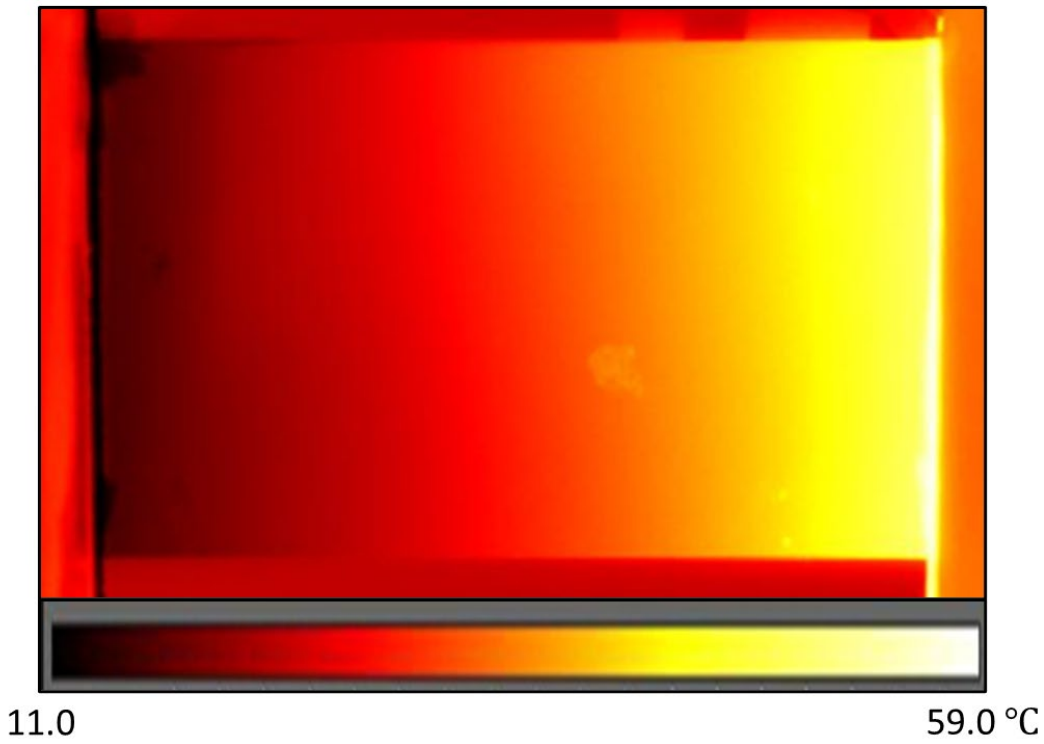

Figure 19. The thermal camera photograph of the temperature gradient substrate obtained 5 minutes after turning on the Peltier devices.

5.4 Results and discussions

The average size and polydispersity of nanoplates were 262 nm. With the increase of volume fraction of ZrP nanoplates, the aqueous suspensions showed phase transition from isotropic liquid to nematic liquid crystal as shown in Figure 20a. The ratio of the height of the nematic phase to the total sample height gave the relative amount of nematic fraction (f_N). The phase diagram was as shown in Figure 20b. The transition from isotropic to isotropic-nematic coexisting phase happened at $\Phi_I = 0.035$ and from coexisting to full nematic phase at $\Phi_N = 0.068$ at which the percentages of nematic phase in the sample were 1% and 99% respectively.

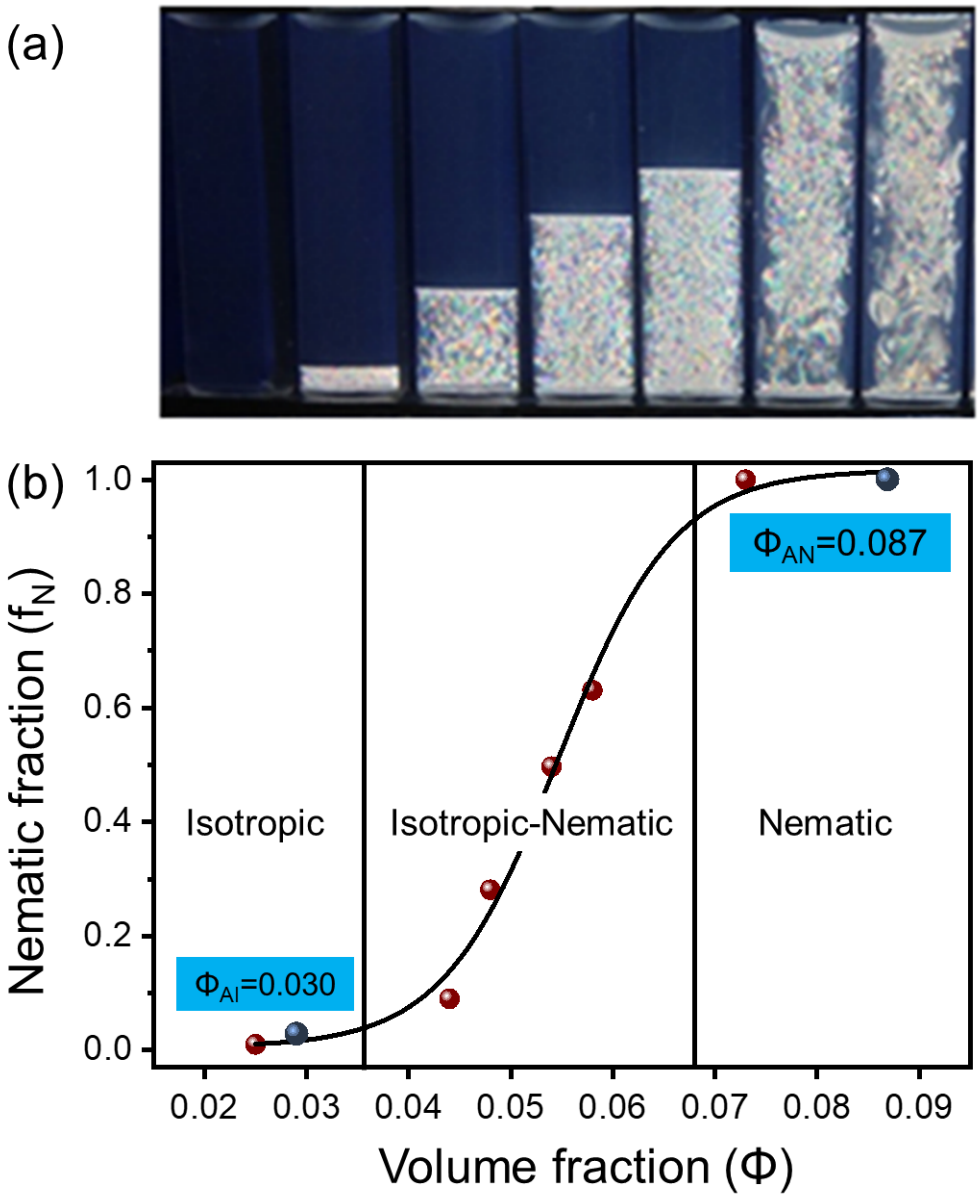

Figure 20. Phase diagram and isotropic & nematic sample choosing for thermophoresis testing. (a) Images of aqueous suspensions of ZrP nanoplates kept between crossed polarizers. The nematic liquid crystal appeared bright and had settled down due to gravity. (b) Phase diagram of isotropic-nematic phase transition in ZrP nanoplates.

Two blue dots in Figure 20 represent the concentration of the isotropic sample and nematic sample used in this study. We chose one isotropic sample and one nematic sample

of zirconium phosphate nanoplates for this experiment. Two samples were performed separately. Its volume fractions are Φ_{AI} = 3.00% and Φ_{AN}= 8.70%. Firstly, isotropic sample was performed in thermophoresis test. The sample was filled in the capillary and was sealed on both sides using UV curable glue. The capillary was placed horizontally in touch with the sapphire crystal plate.

Steady state temperature profile was established three minutes after the voltage was supplied to the Peltier devices and was as shown in Figure 21a. The temperature gradient was along the length of capillary (henceforth, X-axis). As shown in Figure 21b, the suspension appeared completely dark, as observed between crossed polarizers indicating that no liquid crystals were present at the beginning. The left and right menisci appeared bright due to reflection or scattering of light from the liquid-air interface. With the passage of time, as nanoplates underwent thermophoretic drift to the warm region, a small amount of nematic liquid crystalline phase formed as shown in Figure 21c after 80 min of thermophoresis. The local volume fraction of nanoplates at the warm end was thus 7% according to the phase diagram shown in Figure 21d. Due to its nanometer range thickness, it is not possible to observe an individual nanoplate in optical microscope and to track their thermophoretic motion. The formation of the concentration dependent nematic phase at the warm end clearly showed that the nanoplates were sensitive to the external temperature gradient and that they showed thermophilic behavior by drifting to the warm region. Subsequent growth of the nematic phase was observed as shown in Figure 21d-i. The thermophilic (tendency to the warm region) colloidal nanoplate liquid crystal mimicked the behavior of the thermophile micro-organisms. Previous studies

showed that the soft matter phases such as that of the lyotropic chromonic liquid crystal[92] and hard-sphere colloidal crystal[93] formed at the cold end. The fundamental mechanism for thermophoresis of colloids is not clear yet and the movement to the warm or to the cold is understood as a complex function of particle-solvent interactions.[94,95] Simulations of thermophoresis of spherical colloids with tunable interaction showed that the colloids with repulsive interactions drifted to warm regions.[96]

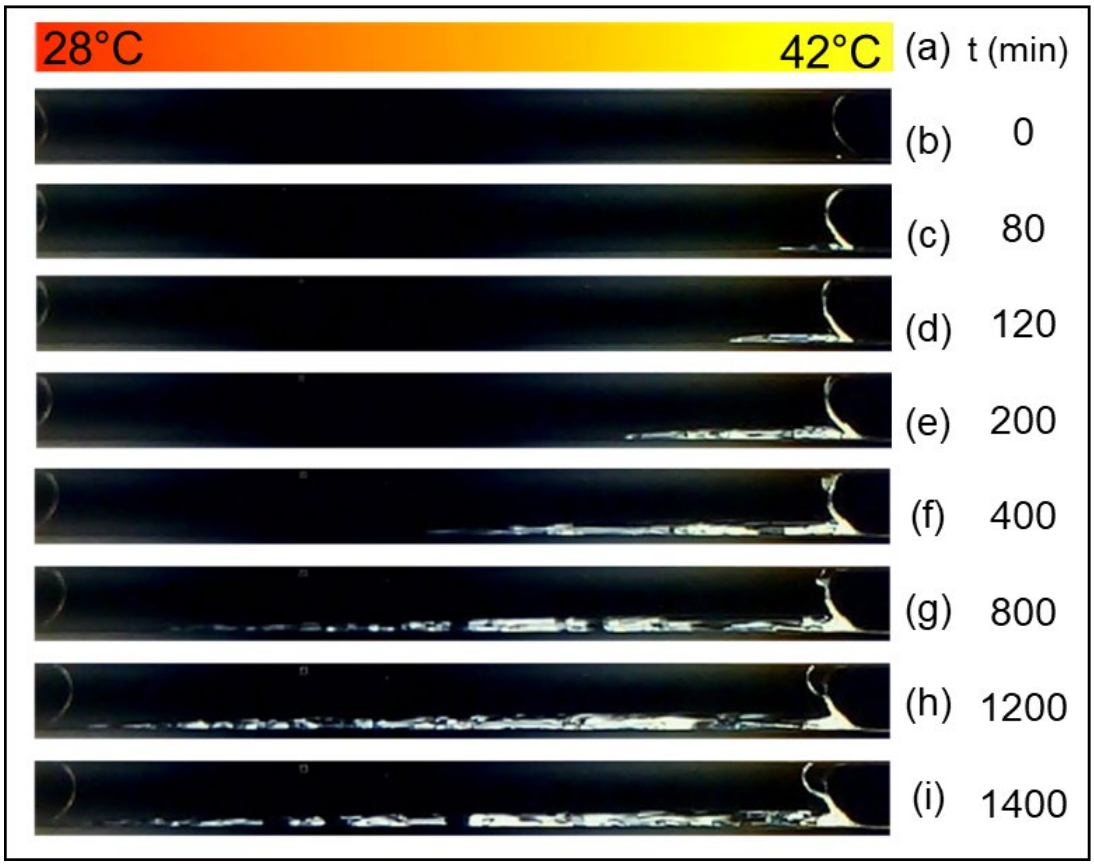

Figure 21. Snapshots of movement of ZrP isotropic liquid crystals under thermophoresis. Total time 1400 min. Time dependent snapshots images of a 2mm high, 26mm long capillary containing isotropic sample.

We used a computational fluid dynamics simulation based on Eulerian multiphase model to study the nanoplates flow velocity and volume fraction change with time. Thermophysical properties of water and nanoparticles are listed in Table 4.[97] The boundary conditions and geometries of the simulation domain are shown in Figure 22a. Initially, 3.2 % of nanoparticles were put into the simulation domain. CFD model simulated a period of 130 seconds after T gradient was applied. On the one hand, nanoplates moved with the carrier fluid. On the other hand, nanoplates tend to move downwards due to gravity. Figure 22b and Figure 22c shows the velocity and volume fraction distribution of nanoplates at the end of the simulation (130 seconds), respectively. As shown by Figure 22c, nematic phase appeared at the right corner, where the nanoparticle volume fraction reaches 4.1 %. Notably, nanoplates concentration increased at the left corner as well, but did not reach to the phase transition concentration, 4.1%. The stagnation zone on the right of the enclosure may contribute to the larger accumulation of nanoparticles on the right corner. It takes about 10 hours for the computer to simulate a period of 130 seconds of the experiment. To fully simulate the experiment may require a future work using super computers.

Table 4. Properties of water and nanoplates for CFD simulation.

	$\rho(kg/m^3)$	$C_P(J/kgK)$	$k(W/mK)$
water	1000	4179	0.613
nanoplate[97]	1600	400	1

Figure 22d illustrated the possible mechanism of colloidal nanoplate nematic phase growth under the temperature gradient. The velocity profile v (blue arrows) for natural convection in the experimental enclosure were shown to divide the sample roughly into four layers- two layers on top half drifted nanoplates to the cold region while the remaining two layers in the bottom half resulted in nanoplate flux towards the warm region. Nanoplates (shown in red) continually moved downwards due to gravity sedimentation (flux is shown as j_g), thus crossing the convective flow lines. Following the convection loop (flux shown by j_v) and subsequent accumulation in the stagnant zones (which were larger at the warm end) and the persistent gravity sedimentation, nanoplate crowding at the bottom of the warm end of the sample resulted into a small nematic phase formation. The growth direction of nematic phase was perpendicular to the isotropic-nematic interface. We argue that nanoplate crowding was greatly enhanced due to convection and the timescale was much shorter than that if only thermophoretic drift ($j_{\nabla T}$) were present. If we consider approximately the bottom ¼ part layer of the sample, initially, $j_{\nabla T}$ is parallel to j_v. Later, convection ceased to exist in this region with the growth of LC phase and thermophoretic flux contributed more. In the top ¾ part section of the sample, convection remained predominant.

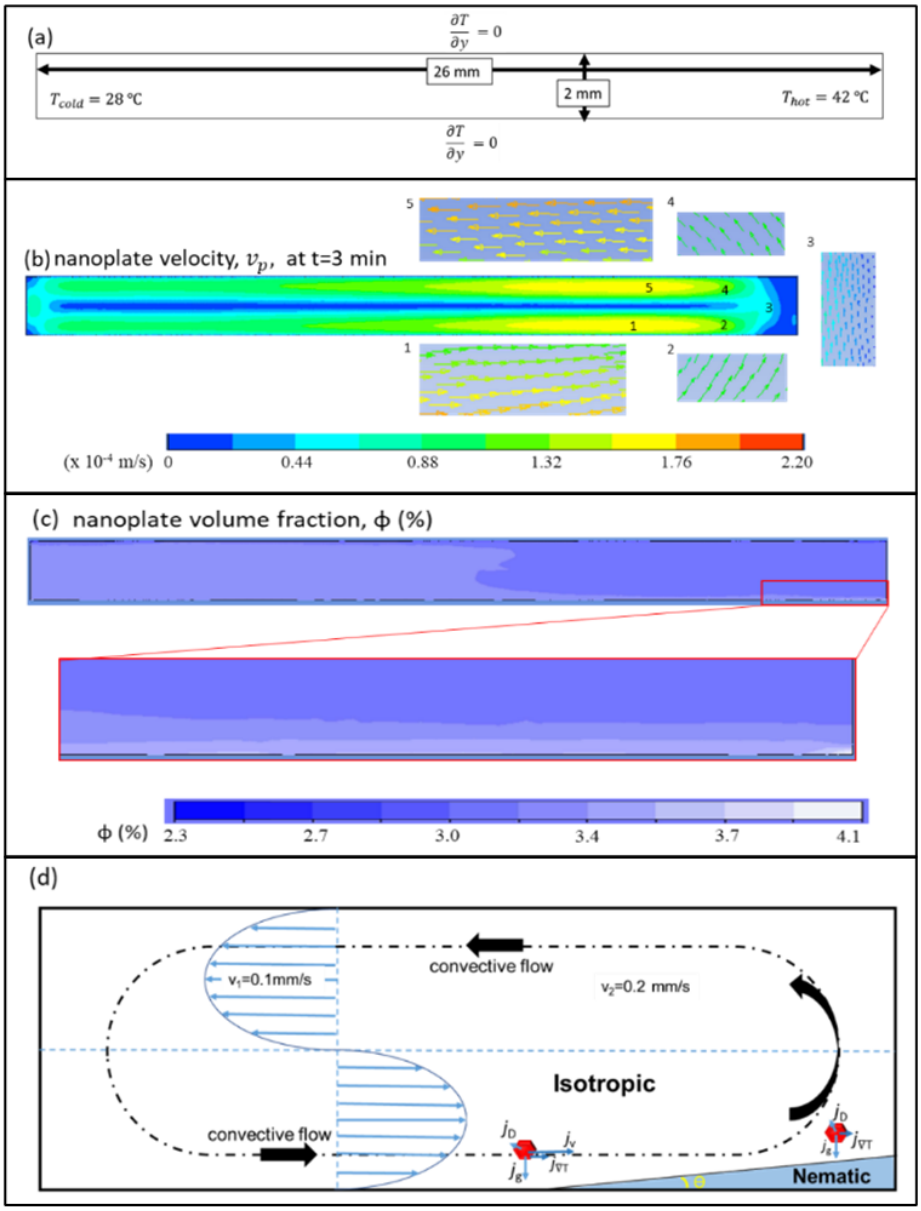

Figure 22. CFD simulation on nanoplate accumulation under a temperature gradient shown at 3 minutes after applying the temperature gradient. Gravity causes particle sedimentation along vertical direction.

Since the isotropic to nematic phase transition is related to the volume fraction of the nanoplates according to the phase diagram shown in Figure 20b, the Soret coefficient of the nanoplates can be estimated from this experiment. Molecular dynamics simulations

showed that the anisotropic rod-shape colloids have a non-vanishing thermophoretic flux in the direction perpendicular to the temperature gradient.[80] However, formation of the nematic phase at the meniscus at warm end of the sample showed that the thermophoretic flux of nanoplates was mainly in the direction of the temperature gradient and the perpendicular component can be neglected.

Moreover, we turned our focus to the steady state profile of nanoplates, at which the further formation of nematic phase stopped. A net positive density gradient towards warm region was evident from the increasing height of the nematic phase. Importantly, the shape of the nematic phase remained undisturbed indicating that the convection was almost negligible in the bottom ¼ part rectangular section of the sample as shown in Figure 23. In remaining ¾ part section on the top, convection was considerable and the nanoplate concentration could be assumed to be uniform at Φ_1. The isotropic-nematic interface made an angle θ (1.5° calculated using ImageJ) with the horizontal direction and isotropic phase present in the bottom ¼ part section of the sample was assumed to have linear concentration gradient in the direction perpendicular to the I-N interface as shown by coordinate l in Figure 23. The concentration of nanoplates was assumed to be equal to Φ_N because it has been previously proven that it takes several days to develop density gradient in nematic phase of nanoplates under external forces such as gravity.[54,98,99] Using the concentration gradient created by the temperature gradient in the isotropic phase present in the bottom ¼ part section outlined with dotted lines, we provide a rough estimate of the magnitude Soret coefficient of zirconium phosphate to be of the order of $0.01/^{o}K$.

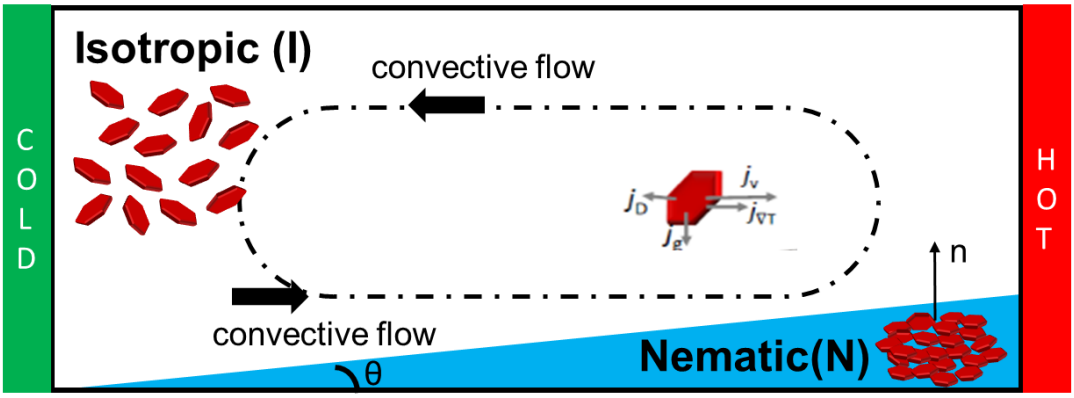

Figure 23. Steady state profiles under simultaneous gravity and temperature gradient conditions. The tilt angle θ was around 1°. Inscribed in squares underneath are nanoplates in isotropic phase having random orientations (left) and in the nematic phase (right) aligned along a common direction, *n*, called the director.

To the best of our knowledge, this is the very meaningful measurement of thermophoretic properties of the nanoplate colloids. The order of magnitude of the Soret coefficient of nanoplates was same as that of spherical (0D) colloids.[88] 2D nano-colloids are attracting an increasing research interest due to their superior properties, the autonomous catalytic activity, than 0D colloids.[100]

Similarly, a full nematic sample of zirconium phosphate nanoplates for this experiment was also performed in the thermophoresis process. Its volume fraction, Φ_{AN} = 8.7% and the sample was filled in the capillary and was sealed on both sides using UV curable glue. The snapshots of capillaries were as shown at Figure 24.

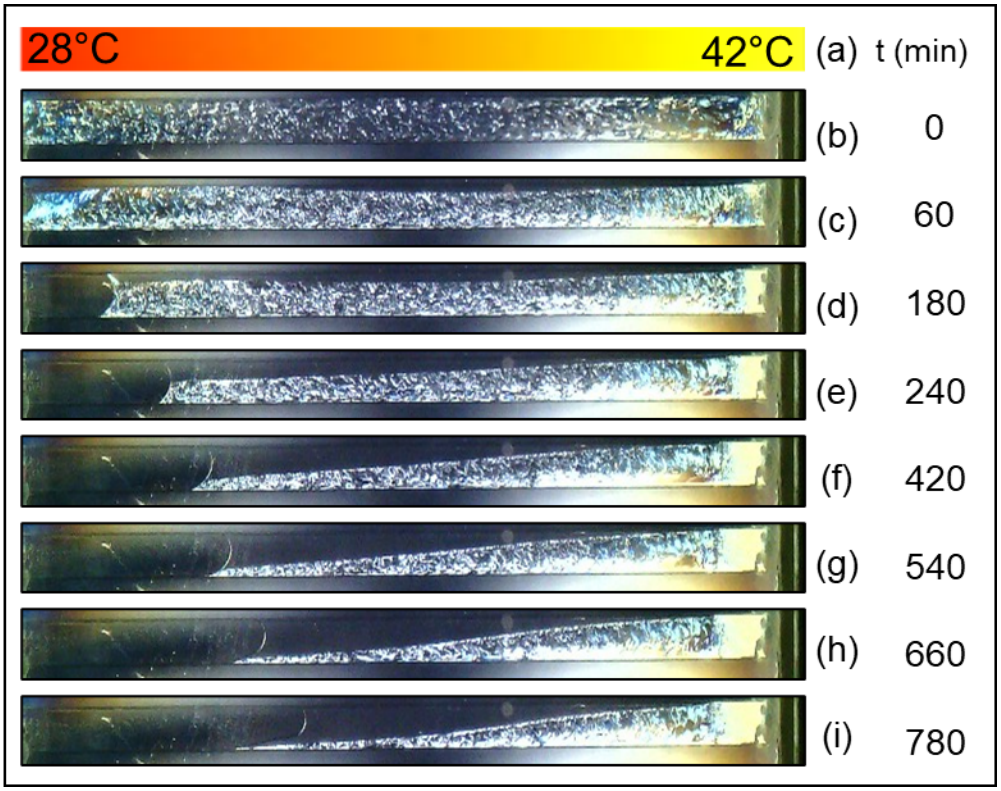

Figure 24. Snapshots of movement of ZrP nematic liquid crystals under thermophoresis. Total time 780min. The steady state was assumed to establish after 660 min.

After experiments completion on the thermophoresis of full nematic Φ_{AN} = 8.70%, two thermophoresis process can be compared. Thermophoresis at Φ_{AI} = 3.00% reaches steady state at 1400 min much slower than 780 min of thermophoresis at Φ_{AN}= 8.70%. The hot ends for both started aggregation and sedimentation and we magnified the hot end through polarized optical microscope and the image was shown below in Figure 25. Both two ZrP liquid crystals got affected with thermophoresis, gravity and convection. Also, both of nanoplates move from the cold end to hot end. It is clear to see isotropic (Φ_{AI} = 3.00%) sample have oriented and formed more nematic phases, while it would be hard to

tell the amount difference of full nematic (Φ_{AN} = 8.70%) samples. Different form isotropic (Φ_{AI} = 3.00%) sample sedimentation in the hot end bottom, full nematic (Φ_{AN} = 8.70%) has high ZrP concentration, which did not have enough space in the hot bottom end. It is interesting to find that due to ZrP liquid crystals stacking, there were interference color bands showing up in Figure 25d, the color bands were not vertically straight because of the gravity and thermophoresis.

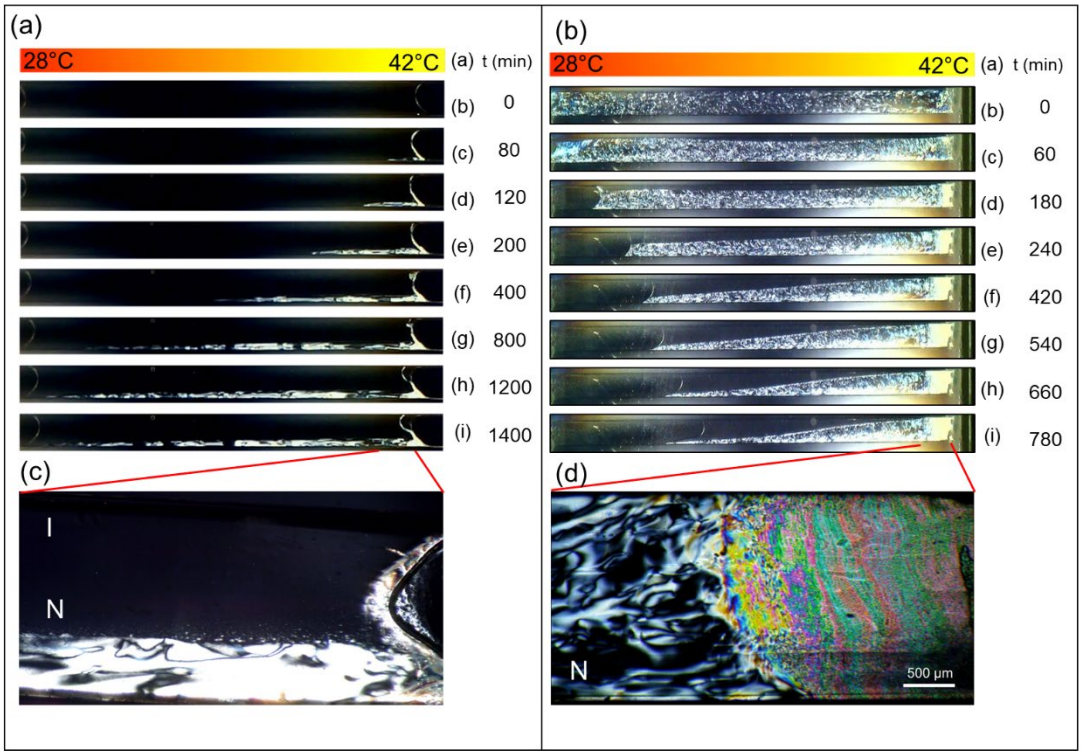

Figure 25. Polarized optical microscope images comparison of two thermophoresis Φ_{AI} = 3.00% and Φ_{AN} = 8.70%. (a) and (b) share same experimental conditions. (c) and (d) have achieved steady state and shared the same scale bar.

The color band differences might be explained through the Michel-Levy interference chart,[101] as shown in Figure 26. From the magnified polarized optical microscope image Figure 26a, the 2D ZrP nanoplates moved to the right side (hot end) due to the thermophoresis and convection flux. The left side of Figure 26a clearly performed nematic liquid crystals and the right side of Figure 26 presented structural colors under polarized optical microscopes and might form higher liquid crystal phases due to the larger nanoplate orientation.

It was usually difficult to directly analyze the nematic concentration relation with a specific position due to the liquid crystal fluidity. But for the right side of Figure 26a, investigating the relations of colloidal liquid crystal concentration and positions has become possible. It was found that the color bands were well-regulated and has a similarity to the Michel-Levy interference color chart. So, six points, which showed yellow, blue, yellow, blue, green, green in the ZrP nanoplate stacking areas were chosen and defined as 1Y, 1B, 2Y, 2B, 3G and 4G. These six points in the interference color bands fit for the colors in the Michel-Levy chart (Figure 26b) from 1^{st} to 4^{th} orders. We calculated the density profile local volume fraction Φ with different heights z/L of all the six points and got the relation plot in Figure 26c. Equation $\Phi=0.44439-6.976989*(z/L)$ was achieved. The 2D colloidal concentration has an approximately linear relation with position and temperatures in the ZrP high concentration stacking area. The liquid crystal phases of the colloidal ZrP stacking areas in Figure 26a could be further characterized by SAXS and higher magnification of polarized optical microscopes.

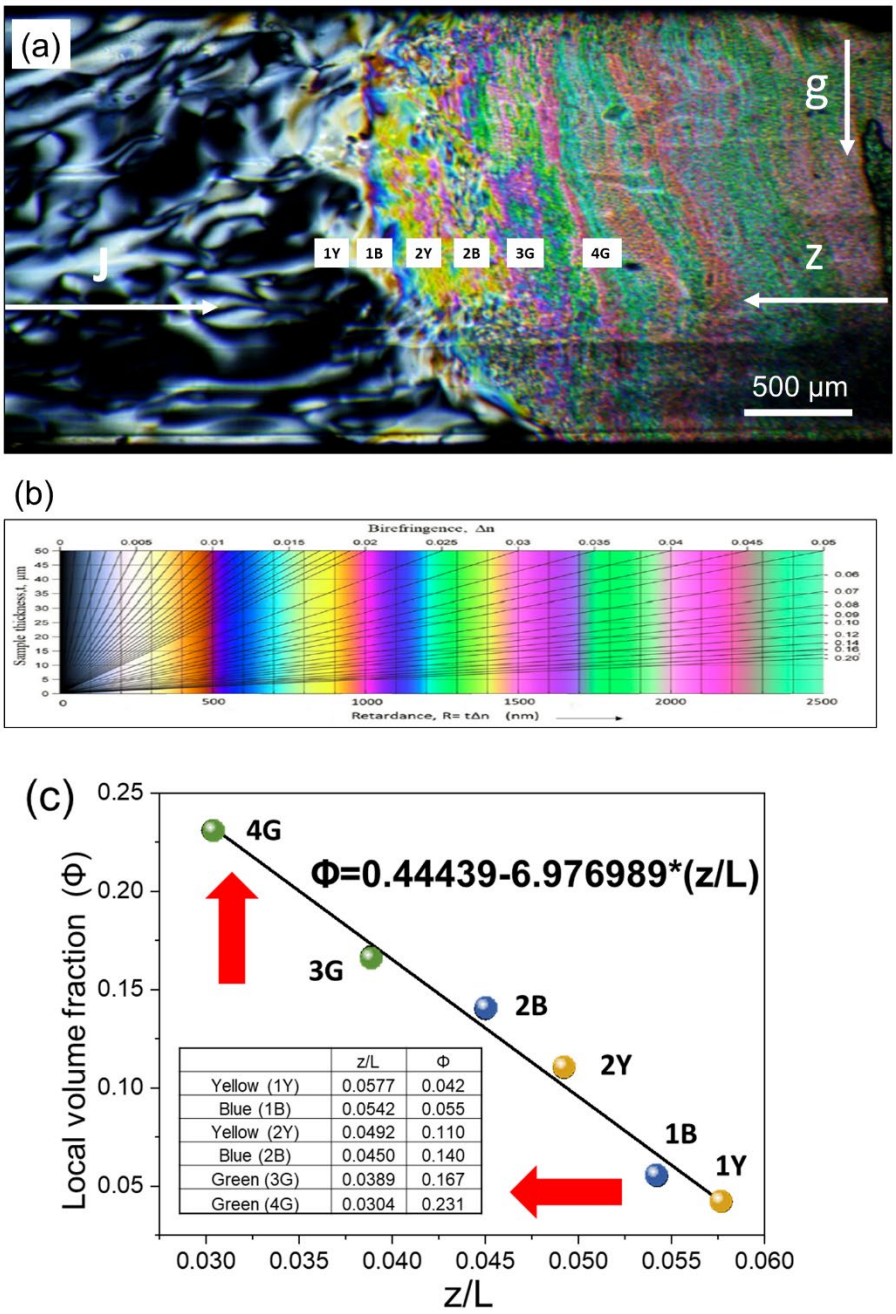

Figure 26. Michel-Levy interference color bands in nematic phases. (a) polarized optical microscope image of sample with initial nematic (Φ_{AN} = 8.7%). (b) Michel-Levy chart. (c) Nematic nanoplate volume fraction vs location (z/L).

5.5 Summary

In summary, we demonstrated an external temperature gradient field-induced formation of liquid crystals of nanoplates exploiting the concentration dependent phase transition in anisotropic colloids. The establishment of net concentration gradient of nanoplates was indicative of thermophoretic effects while the natural convection helped speeding up the process. The external temperature field and thermophoresis could help move the 2D colloidal particles and reorientation to nematic or higher-ordered structures, which would be useful in bio transport or drug delivery. We point out that external temperature gradient controlled formation of the liquid crystal phase can be achieved in colloids, and the colloidal liquid crystals has the potential to form new smectic phases.

CHAPTER VI

2D COLOR-ENHANCED NEMATIC PHOTONIC LIQUID CRYSTALS*

6.1 Synopsis

Biomimetic nanostructured materials with iridescent structural colors have attracted significant attention due to their potential in photonic inks, optoelectronic devices, and biomedical engineering. In this chapter, the concentration effect on structural colors would be investigated. We first develop the artificial 0D spherical photonic crystals, and promote to 2D nanoplate photonic crystals. The structural colors of 2D ZrP photonic liquid crystals come from short-ranged nematic order, which is different from the 0D polystyrene long-ranged periodic ordered structures. Moreover, 2D nanoplate photonic hydrogels are fabricated through the nanoplate concentration tuning. Also, due to the increasing interest in applications for structural color enhancement, the additives are used for absorbing incoherent light and improved color visibility.

6.2 Introduction

Biomimicking the structural iridescent colors of living organisms such as butterfly wings and cephalopods, which may provide an important channel for mate signaling and communication as well as survival in hostile environments, is currently in the research limelight due to their fundamental importance and potential technological applications.[102-

* Part of this chapter is reprinted with permission from "Biomimetic colloidal photonic crystals by coassembly of polystyrene nanoparticles and graphene quantum dots." by Huang, D., Zeng, M., Wang, L., Zhang, L. and Cheng, Z., 2018. RSC advances, 8(61), pp.34839-34847. Copyright 2021 by RSC Publishing.

[109] It has been demonstrated that the fascinating structural coloration in the wings of morpho butterflies arises from the combination of highly ordered or quasi-amorphous structures and embedded black melanin,[110-113] with the periodic lattice structures generating the iridescent structural colors while the melanin enhances the color visibility by serving as a background absorber.[114, 115] A variety of colloidal photonic crystals have been fabricated through facile self-assembly of different colloidal nanoparticles, such as silica, polystyrene, and poly (methyl methacrylate) into a close-packed array.[116-119]

Besides the 0D artificial spherical photonic crystals, 2D nanoparticles photonics have also achieved great interest in self-assembling and structural color exploration.[120] The reflection color 2D photonic crystals result from the long-range positional ordering, like lamellar periodic arrangement.[121, 122] Traditional 2D materials like GO and titanium oxide,[123, 124] were recently utilized into photonic liquid crystals (PhC). But reflection structural colors by nematic structure is rarely able to be seen. Most likely it is because that in the nematic phases, it is hard to find long ranged periodic structures. In the result of smaller order parameter and less crystalline, the nematic phase photonic color is a challenging task. The nematic photonic liquid crystals will be required to reflect structural colors in a shorter periodic range instead of the long-range periodicity.

On the other side, the low color visibility originated from incoherent scattering remains a hindrance to practical applications.[125] Inspired by butterfly wings, artificial photonic crystals with enhanced colors have been reported by incorporating various black additives like dark color polymers[126, 127] and magnetic nanoparticles[128, 129] into ordered structures, leading to enhanced color visibility. In addition to synthetic materials, natural

biopolymers such as cuttlefish ink[130] have also demonstrated strong capacity for reducing incoherent light scattering, thus enhancing the color visibility of photonic crystals. With the development of the additives in biomimetic photonic crystals, it also brings new problems. Some undesired defects or dislocations, such as impure phases and missing local particles, however, are often inevitably introduced into the colloidal PhCs due to the nonuniform size of these additives and low compatibility with colloidal nanoparticles. Graphene quantum dots (GQDs) are single-layer to few-layered graphene nanoparticles with lateral dimensions smaller than 20 nm, which have attracted much research interest due to their unprecedented advantages of controllable synthesis, cost effectiveness, superior compatibility and high photoluminescent quantum yield.[131-139] Different from traditional enhanced photonic crystals' research, graphene quantum dots have competitive advantages on working as additives of photonic crystals. First, the morphology of GQDs can be well-tuned and prepared in nanoscale range (5-15 nm) such that the small size of GQDs will retain the integrity of PhCs, preserving their periodic lattice structures. Second, the surface carbonization of GQDs can be readily modulated by controlling the kinetics of hydrothermal reaction to actively tailor the blackness of GQD additives. Some successful examples of controlled surface carbonization by hydrothermal treatment have been reported for applications like cell labeling,[140, 141] photovoltaic devices[142, 143] and sensors.[144]

In this chapter, the colloidal 0D sphere and 2D nanoplate photonic crystals with enhanced color visibility were achieved. The oriented orders of 0D and 2D photonic crystals will be discussed. Furthermore, enhanced colloidal photonic crystals with brilliant structural colors covering the full visible spectral range could be tuned through lattice

spacing between nanoparticles, which are concentration in this 2D ZrP system. The resulting 2D colloidal photonic crystals could fabricate photonic hydrogels and utilized in nanoink printing.

6.3 Experimental

6.3.1 Polystyrene nanoparticles (0D)

Chemicals were purchased from commercial suppliers and were used without further purification. For preparation of PS nanoparticles, styrene (stabilized, purity > 99%) was purchased from Acros Organics. Methyl methacrylate was obtained from Polysciences, Inc. Acrylic acid (purity > 99%), ammonium persulfate (purity ≥ 99.99%), sodium dodecylbenzenesulfonate (technical grade), and sodium bicarbonate (purity ≥ 99.7%) were purchased from Sigma-Aldrich.

Monodisperse PS nanoparticles were fabricated using the emulsion polymerization method. In a 500 mL bottom-boiling flask, 28.0 g styrene, 1.1 g acrylic acid, 1.5 g methyl methacrylate, and 200 mL deionized water were heated to 85 °C under magnetic stirring and nitrogen flow. Then 0.725 g ammonium persulfate (APS), 2-9 mg sodium dodecylbenzenesulfonate (SDBS), and 500 mg $NaHCO_3$ were added into the solution. The PS nanoparticles were achieved after continuous heating at 85 °C for 7 hours. The size of synthesized PS nanoparticles was primarily tuned by varying the SDBS amount. Monodispersed PS colloidal nanoparticles of different sizes (192, 214, 274 and 396 nm) were purified by washing three times with water. The PS suspension was subjected to a freeze-drying process to produce dried monodisperse PS powder.

6.3.2 Zirconium phosphate nanoplates (2D)

The sample used in this experiment was sample E (12M-reflux-40hr). The detailed synthesis procedure was discussed in Chapter III. The ZrP suspension volume fraction was prepared by various concentrations 54.5%, 51.2%, 47.3%, 37.5% and 31.0% in the rectangular vials. For the photonic color enhancement experiment, the ZrP suspension volume fraction kept the same and the GQDs additives concentration was 1 wt% of ZrP suspension.

6.3.3 Graphene quantum dots synthesis

Chemicals were purchased from commercial suppliers and were used without further purification. For preparation of GQDs, citric acid (purity > 99%), 1-thioglycerol (purity ≥ 97%), and glycine (purity ≥ 98.5%) were purchased from Sigma-Aldrich.

GQDs were prepared using the traditional hydrothermal pyrolysis method. 2.40 g citric acid and 1.0 g glycine were dissolved in 5 mL deionized water, then 1.07 g 1-thioglycerol was added, after that sonicated for 15 minutes. The solution was then decanted into an 80 mL Teflon vessel and sealed within a stainless autoclave reactor. The autoclaves were heated to 200 °C and three different reactions were prepared with 3 hours, 5 hours and 7 hours, separately. The reaction products were centrifuged at 10000 rpm for 15 minutes to remove solid residue.

6.3.4 Fabrication of PhCs films by drop-casting method

The PhCs film was prepared by the drop-casting method. The PhCs composite suspension was prepared by mixing fixed amounts of PS powder and 0 wt%, 0.1 wt%, 0.5 wt%, and 1 wt% GQDs, then deionized water was added to make a solution density of PS nanoparticles of 100 mg/mL. The solution was shaken by vortex mixer and put under sonication for 10 minutes to achieve uniformity. A black paper was placed on the 50 °C hot plate surface. Then 100 µl mixed suspension was dropped onto the black paper and allowed to dry. The enhanced PhCs thin film was made after complete drying.

6.3.5 Fabrication of PhCs flakes by the centrifugal sedimentation method

The PhCs flakes were prepared by the centrifugal sedimentation method. 200 mg PS powder was added into different volumes of 0.2 mg/mL GQDs solution (0 wt%, 0.1 wt%, 0.5 wt%, and 1 wt%). The suspension was transferred to a 50 mL centrifuge tube into which deionized water added to fill to an amount of 35 mL. The solution was shaken on a vortex mixer and centrifuged at 10000 rpm for 45 minutes. Then the PhCs flakes were taken out by a spoon spatula after removal of solution followed by drying on the 50 °C hot plate.

6.4 Results and discussions

The 0D PS nanoparticles were achieved through emulsion polymerization. The size of synthesized PS nanoparticles was primarily tuned by varying the SDBS amount. Monodispersed PS colloidal nanoparticles of different sizes (192, 214, 274 and 396 nm)

were purified by washing three times with water, as shown in Figure 27. The PS suspension was subjected to a freeze-drying process to produce dried monodisperse PS powder.

The PhCs film was prepared by the drop-casting method. The photonic crystals were suspended in water and the solution was shaken by vortex mixer and put under sonication for 10 minutes to achieve uniformity. A black paper was placed on the 50 °C hot plate surface. Then 100 µl mixed suspension was dropped onto the black paper and allowed to dry. The enhanced PhCs thin film was made after complete drying, as shown in Figure 27a-d inlet. The 0D nanoparticles self-assembled and due to the Bragg reflection and reflected green color.

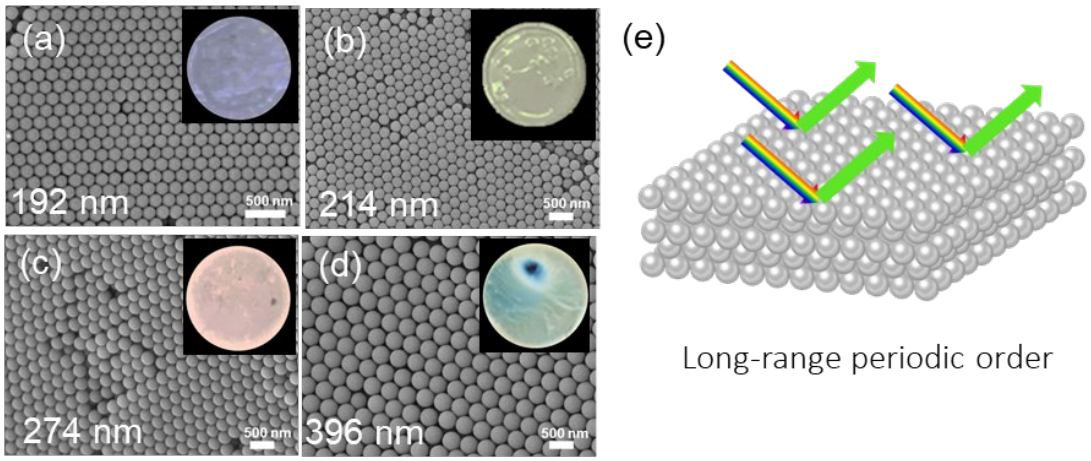

Figure 27. 0D sphere photonic crystals. (a)-(d) SEM image of polystyrene nanoparticles (192nm, 214nm, 274nm, 396nm) and structural color films (e) Scheme of Bragg's law of 0D spherical photonic crystal and reflected green color.

Inspired by 0D nanoparticle photonic crystals, we started to use ZrP nanoplate for self-assembling as a film, as shown in the inlet of Figure 28a. When the film is completely dry, it revealed white color. The ZrP nanoplate film can be considered 100% volume fraction, so we started to gradually add water in the system and decrease the ZrP nanoplate concentration. ZrP solution started to show structural color at around 55% volume fraction. The reflection structural color transfer from blue to green, then red. The volume fraction decreasing come with larger lattice spacing and moved to larger wavelength (red shift), which fits the Bragg diffraction. The 2D ZrP red structural color vial was observed under the polarized optical microscope, as seen in Figure 28c, the nematic structure was shown. We could predict that the structural color from ZrP photonic liquid crystals did not come from long-range periodic order, but come from short-range nematic structures.

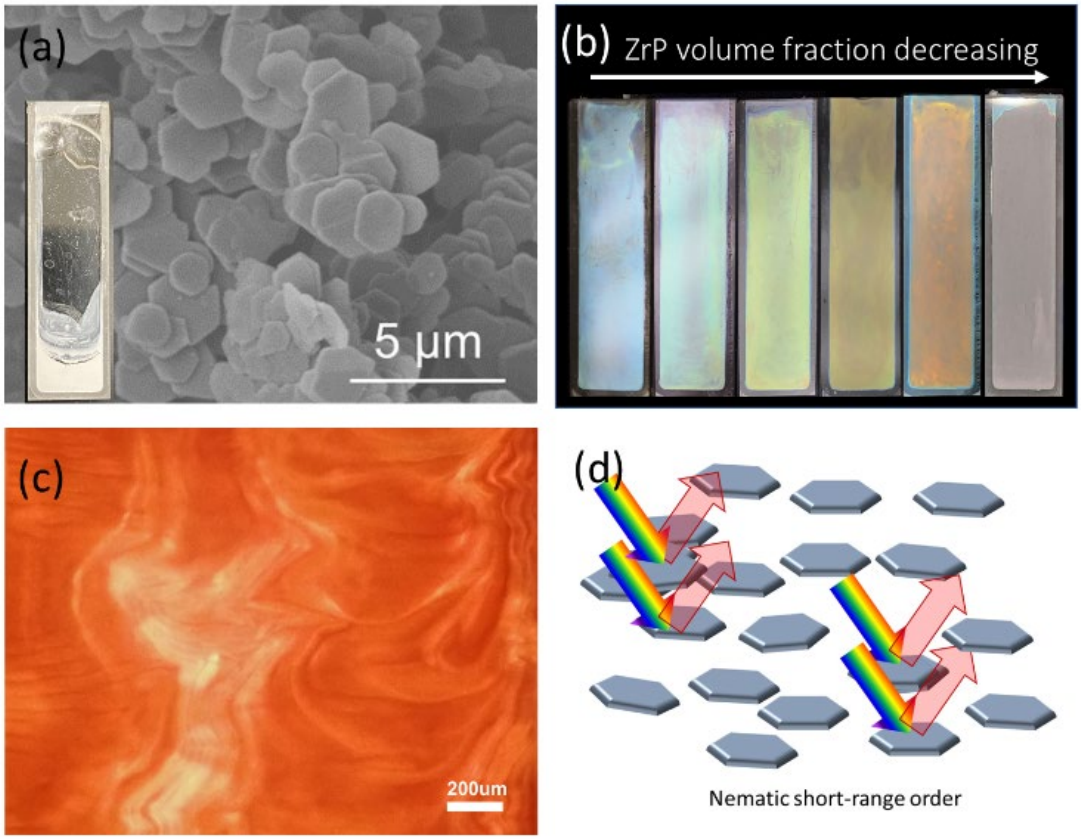

Figure 28. Self-assembly of 2D ZrP photonic liquid crystals. (a) SEM image of ZrP nanoplate and inlet photo is white ZrP nanoplate film. (b) Image of ZrP photonic liquid crystals. (c) POM image of ZrP Nematic phase. (d) Scheme of mechanism for 2D ZrP photonic liquid crystals.

We found out unexfoliated nanoplates are easier to settle down compared with exfoliated ZrP. The 2D nanoplates were easier to settle down and appear fractionation with narrower containers. As seen in Figure 29a, ZrP suspension of volume fraction 0.35 and was close to the concentration of red sample suspension in Figure 28b. The ZrP suspension was immersed into the capillary and the capillary was vertically displayed 5 days and found out that the sample has fractionated, the bottom side of the capillary presented blue color indicating higher concentration, and the top side of the capillary

presented red color indicating smaller concentration. This fractionation has motivated us to build the nematic photonic hydrogel. The recipe includes acrylic amide monomer, bis-acrylamide crosslinker, LAP photo initiator, DI water and ZrP nanoplates. Similar with the fractionation method shown in Figure 29a, the ZrP was mixed with hydrogel monomer and sealed in a film mold vertically and waited 3 days, it was obvious to see that on the top side there is no obvious structure color showing, indicating isotropic phase, while on the bottom side, the structural color of blue revealed very clearly, indicating the nematic phase formation. After UV light crosslinking, the front view and side view of (Figure 29c and d) the 2D ZrP hydrogel film under polarized optical microscope was shown. It was clear to see the edges between dark side and bright side. The bright side revealed the ZrP nematic liquid crystal phase.

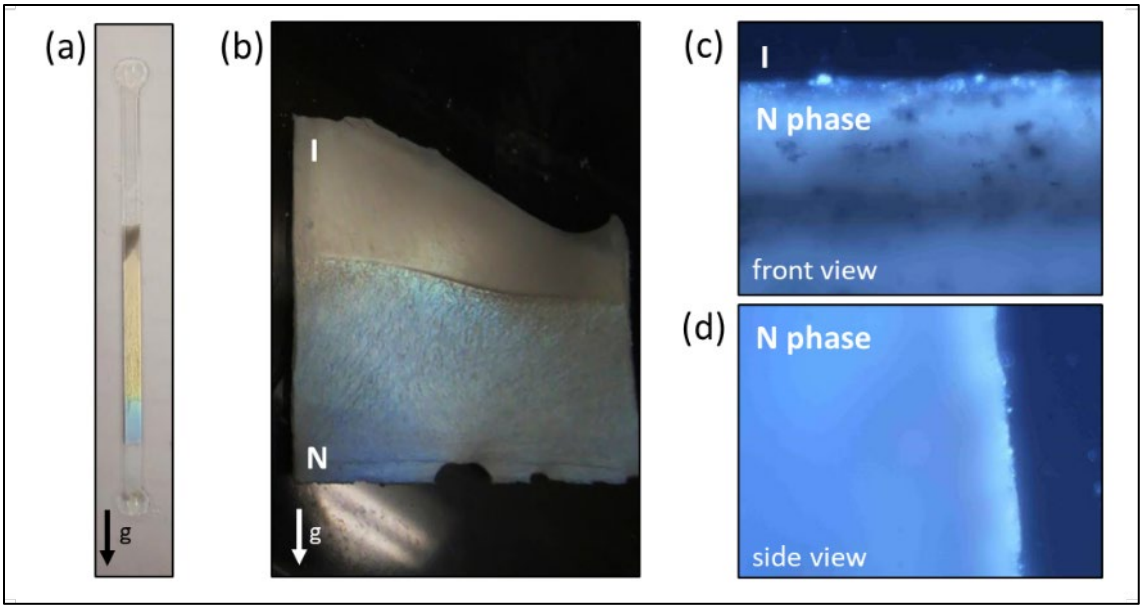

Figure 29. (a) Photograph of a capillary of ZrP suspension (Φ =0.35) vertically displayed over 5 days. (b) Photograph of ZrP nanoplate photonic hydrogel vertically displayed over 3 days. (c) POM image of the hydrogel film in front view. (d) POM image of hydrogel film in side view.

To improve the color visibility of photonic crystals for potential industry areas, the study of color enhancement additives for photonic crystals was investigated (Figure 30). As seen in Figure 30a, GQDs with various amounts (0, 0.1%, 0.5%, 1%) were synthesized and dispersed in 0D polystyrene solution. From visual perception, it was apparent that higher GQDs doping concentration in PhCs films resulted in more brilliant green structural color. The reflectance spectra shown in Figure 30b further clarified the reflectance mechanism of enhanced photonic crystals. Pure PS thin films showed relatively high reflectance intensity. When GQDs (0.1 wt%, 0.5 wt%, and 1 wt%) were added to the PS photonic crystals, the visible reflectance intensity started to decrease. Larger GQDs additives concentration resulted in lower reflectance intensity of photonic crystals. This

might result from the incoherent light absorption by the GQDs. Higher concentration of GQDs inside PS photonic crystals would absorb more background and scattering light, while enhanced photonic crystals exhibited better color visual appearance. The reflectance peak intensity of PS/GQDs photonic crystals in Figure 30b was normalized and could be seen in Figure 35, the normalized peak intensity increased from 11.58% to 18.22%, which implied the peak intensity increment of GQDs addition. Figure 30c presented different structure colors of 0D polystyrene on various substrates, performing its photonic potentials.

For Figure 30d and e, it was clear to see that the GQDs additives could also fit for fluids and 2D nanoplate photonic liquid crystals. It was obvious that the color visibility of ZrP nematic photonic crystal has improved. In Figure 30f, presented the 2D photonic crystal' drawing potential and its iridescent characteristic.

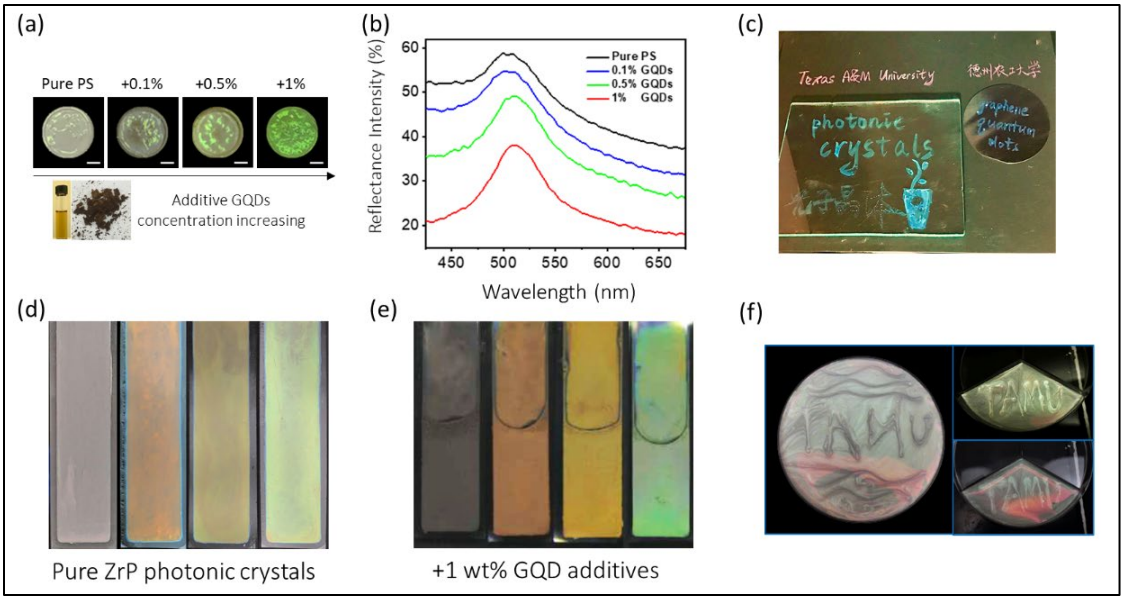

Figure 30. (a) Image of fabrication of enhanced 0D PS photonic crystals with various GQDs additives. (b) Reflectance spectra of PS-GQDs spectra. (c) 0D photonic ink writings on different substrates. (d) Photograph of Pure 2D ZrP photonic crystals before adding GQDs additive. (e) Photograph of 1wt% GQDs additive. (f) Photographs of 2D photonic fluids.

The possible mechanism of Bragg reflection color enhancement of colloidal photonic crystals is schematically illustrated in Figure 31. The synthetic photonic crystal presented structural colors under natural daylight. Monodisperse PS nanoparticles (214 nm) with ordered Bravais lattice structures formed the colloidal photonic crystals with comparatively pale green structural color. The small GQD additives tended to aggregate around the big PS nanoparticles and GQD additives entered the void space of colloidal photonic crystals. It should be noted that the lattice structure of 0D photonic crystal did not show obvious changes with the addition of a slight amount of GQD additive. The GQDs localized in the interstitial space reduced the incoherent light scattering, therefore

brilliant structural colors with high visibility were observed in such colloidal photonic crystals.

For 2D ZrP photonic liquid crystals color enhancement, similar color enchantment behaviors have been seen, there is possibility that GQDs may not adhere to 2D nanoplates but suspend in the ZrP photonic liquid crystals.

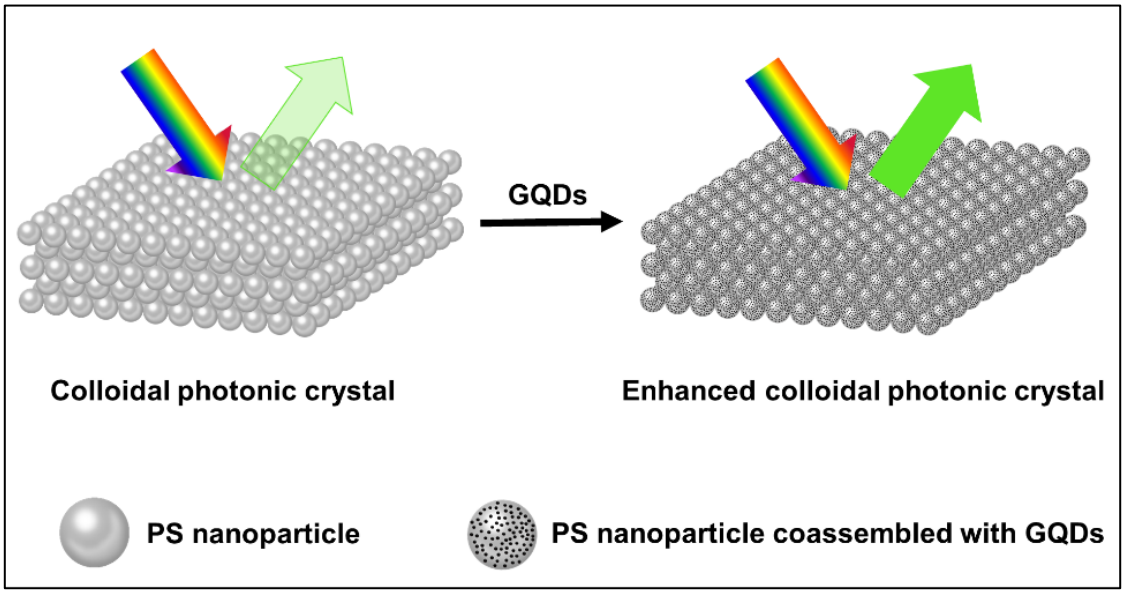

Figure 31. Schematic illustration of the Bragg-reflection color enhancement of PS and PS/GQDs colloidal photonic crystals. The size of PS nanoparticle is 214 nm.

Figure 32 represented the detailed synthetic route and characterizations of GQDs color-enhanced additives. GQDs were fabricated using a controlled hydrothermal reaction of low molecular organic compounds including citric acid, glycine, and 1-thioglycerol. During the 200 °C pyrolysis process, citric acid and glycine were utilized as main carbon sources and 1-thioglycerol worked as the reducing agent. GQDs with various

hydrothermal carbonization degrees were gradually formed due to reaction time difference. The synthesized GQDs were described as GQDs-x, in which x was the hydrothermal reaction time of GQDs. Herein, 3 hours, 5 hours, and 7 hours of hydrothermal pyrolysis of GQDs would be referred to as GQDs-3, GQDs-5 and GQDs-7, respectively. The morphology of GQDs-7 was characterized through TEM image, as shown in Figure 32b. The GQDs-7 had a narrowly distributed size range and the average size was 12.0 nm. The size uniformity of GQDs was also confirmed through AFM image. Then Figure 32c showed the absorption spectra of various GQDs in aqueous suspension. As shown in the figure, the light intensity absorption order of GQDs was GQDs-7 > GQDs-5 > GQDs-3 under the same concentration, 0.2 mg/mL. This observation confirmed that higher carbonized GQDs with additives could absorb more extra light and would be able to enhance photonic crystals. The absorption intensity of dried GQDs was further characterized by UV-vis spectroscopy in Figure 32d. The spectra showed high absorption of GQDs in the visible spectrum. The inset image was the photograph of dried GQDs-7.

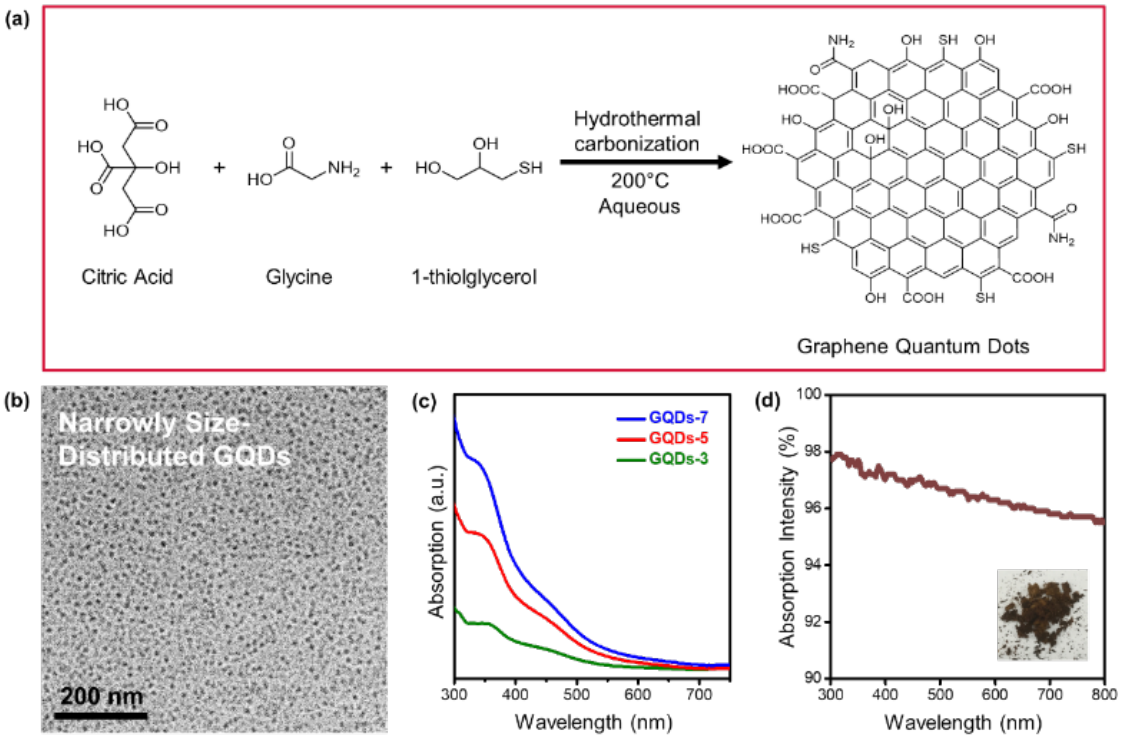

Figure 32. Fabrication of GQDs. (a) Synthesis route of GQDs. (b) TEM images of GQDs-7. (c) Absorption spectra of GQDs aqueous suspension with different reaction time (3 hours, 5 hours, and 7hours). (d) UV-vis absorption spectra of pure GQDs-7. The inset was the photograph of dried GQDs-7.

The reasonable hypothesis was made that the chemical state of GQDs would also change with the hydrothermal processing. Figure 33 exhibited the X-ray photoelectron spectroscopy (XPS) of GQDs. From the XPS survey scan in Figure 33a, we observed that the synthesized GQDs consisted mainly of four elements: carbon, nitrogen, oxygen, and sulfur. Specifically, detailed change of four elements concentration could be investigated in XPS elemental analysis, as shown in Table 5. The carbon concentration of GQDs-3, GQDs-5 and GQDs-7 were 68.06%, 70.55% and 74.11%, revealing a clear increasing trend of carbonization degree by increasing reaction time. Carbon content increased with

GQDs' reaction time, while a consistent loss of nitrogen, oxygen, and sulfur content was observed.

To further study the carbonization degree of GQDs, the carbon spectra of XPS under various reaction hours were performed as shown in Figure 33b. The binding energy of C-C was 284.8 eV and of which C=O was 288.6 eV. The peak intensities of C-C, C=O were obtained from Figure 33b and C-C/C=O ratio were calculated. The C-C/C=O ratio indicated the chemical environment of carbon element as well as the amount of oxygen defects existing in conjugate carbon network, which dictated the absorption capability of visible light, *i.e.*, blackness of GQDs.[139] The C-C/C=O ratios were 2.05, 2.32 and 2.95 under the reaction time of 3 hours, 5 hours, and 7 hours, respectively, suggesting that increment of hydrothermal reaction time of GQDs would result in a higher degree of carbonization.

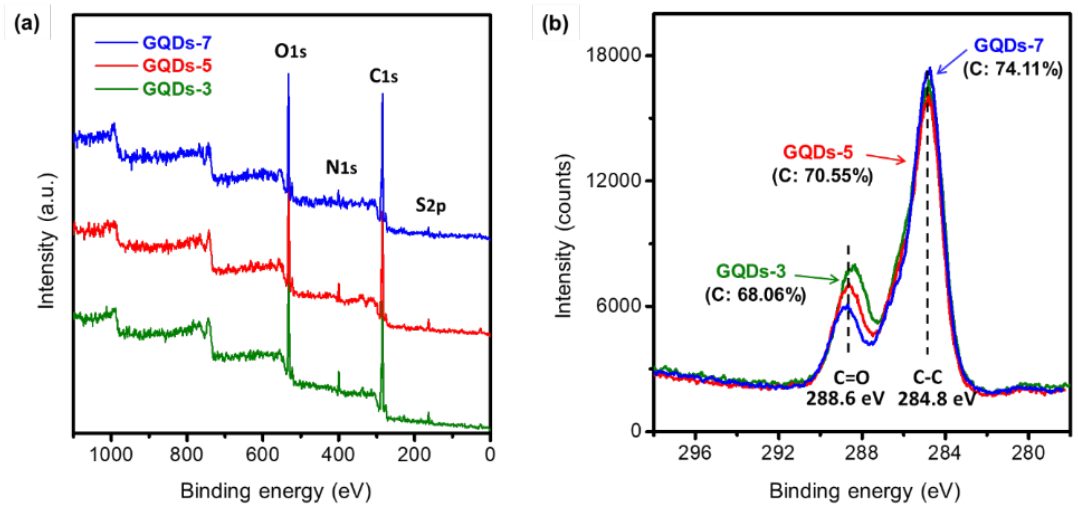

Figure 33. X-ray photoelectron spectroscopy of GQDs. (a) XPS survey scan of GQDs with reaction time of 3 hours, 5 hours, and 7 hours at 200 °C. (b) XPS carbon chemical state of GQDs with reaction time of 3 hours, 5 hours, and 7 hours. (The C-C/C=O ratios with various reaction times, respectively, were 2.05, 2.32, and 2.95)

Table 5. XPS elemental analysis of GQDs with different reaction time.

	C %	N %	O %	S %	Total %
GQDs-3	68.06	5.05	23.57	3.32	100
GQDs-5	70.55	3.15	23.06	3.24	100
GQDs-7	74.11	2.48	20.26	3.16	100

The enhanced PS photonic crystals with various GQDs' reaction time were studied in Figure 34. Two different methods of fabricating enhanced photonic crystals, centrifugal sedimentation and drop-casting, were introduced in Figure 34a and Figure 34b. PS photonic crystals with GQDs would be defined as PS/GQDs, and PS/GQDs-x would be precedingly described as the PS photonic crystals with GQDs which underwent x hours hydrothermal reaction. Photographs of photonic crystal flakes of PS and enhanced PS/GQDs, taken under natural light, were presented in Figure 34a. All PS nanoparticles in Figure 34 were uniform of 214 nm average size, and GQDs concentration was 1 wt%. From Figure 34a, pure PS photonic crystals looked pale and barely showed structural color. With increasing hydrothermal reaction time, from 0 to 3 hours, 5 hours, and 7 hours, the crystal flakes progressed to exhibit better green structural color. The size of the enhanced PhCs flakes was measured as 1 - 2 cm. Figure 34b introduced another drop-casting method of fabricating PS and PS/GQDs photonic crystals films. The films were prepared through using a pipette to drop casting a fixed amount of PS/GQDs suspension in water onto the black paper. The paper was heated on the 50 °C hot surface resulting in PhCs films with a flatter surface compared with those crystal flakes due to the quick self-assembling process. From Figure 34b, PhCs films were differentiated by the GQDs' hydrothermal reaction time. Under the same 1 wt% GQDs concentration, the color

visibility of PS/GQDs photonic crystal films was better than that of the pale PS film. The PS/GQDs-7 photonic crystals films had the best color visibility, progressing to lesser color visibility accompanied with shorter hydrothermal processing time.

The reflectance spectra of photonic crystals films, which confirmed their visual appearance, were investigated in Figure 34c. The reflectance spectra of pure PS thin films had the largest reflectance intensity of all. High reflectance intensity would come with poor color visibility. The structural color of pure PS photonic crystals appeared milky white and pale, being strongly suppressed by scattering and background light. By tuning hydrothermal reaction time of GQDs additives (3, 5 and 7 hours), the carbonization of GQDs additives was controlled simply, achieving the desired small reflectance intensity of photonic crystals films. Longer GQDs hydrothermal pyrolysis time resulted in larger carbonization, with PS/GQDs photonic crystals films having accordingly smaller reflectance intensity and higher color visibility. Figure 34d showed the corresponding normalized reflectance peak intensity of Figure 34c. PS/GQDs photonic crystals films with higher carbonized GQDs had larger normalized reflectance peak intensity compared with PS/GQDs photonic crystals of smaller carbonized GQDs and pure PS.

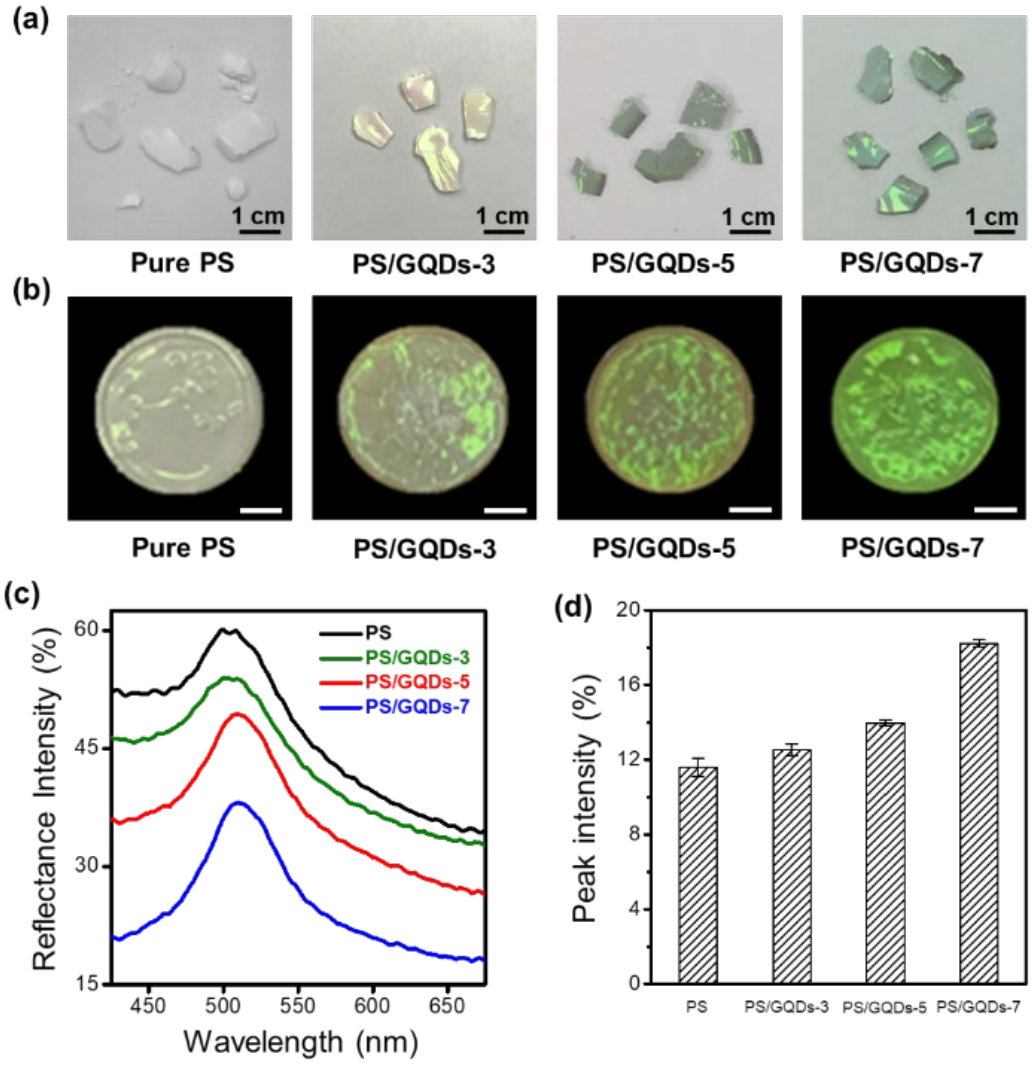

Figure 34. Fabrication of enhanced PS photonic crystals with different carbonization of GQDs.

Interestingly, apart from the effect of carbonization of GQDs, the GQDs additives dosage in PS photonic crystals could also affect color visibility. Figure 35 demonstrated the fabrication of enhanced PS photonic crystals at various GQDs concentrations. The enhanced PS/GQDs photonic crystal films were shown in Figure 35a. The polystyrene nanoparticle size was 214 nm, and the GQDs had undergone hydrothermal reaction of 7

hours. The PhC films were also fabricated by the drop-casting method, with all films having around 1 cm diameter. From visual perception, it was apparent that higher GQDs doping concentration in PhCs films created more brilliant green structural color. The reflectance spectra shown in Figure 35b further clarified the reflectance mechanism of enhanced photonic crystals. Pure PS thin films showed relatively high reflectance intensity. When GQDs-7 (0.1 wt%, 0.5 wt%, and 1 wt%) were added to the PS photonic crystals, the visible reflectance intensity started to decrease. Larger GQDs additives concentration resulted in lower reflectance intensity of photonic crystals. This might result from the incoherent light absorption by the GQDs. Higher concentration of GQDs inside PS photonic crystals would absorb more background and scattering light, while enhanced photonic crystals exhibited better color visual appearance. The reflectance peak intensity of PS/GQDs photonic crystals in Figure 35b was normalized, as shown in Figure 35c. With the GQDs-7 concentration increasing from 0 wt% to 1 wt%, the normalized peak intensity increased from 11.58% to 18.22%, which implied the peak intensity increment of GQDs addition.

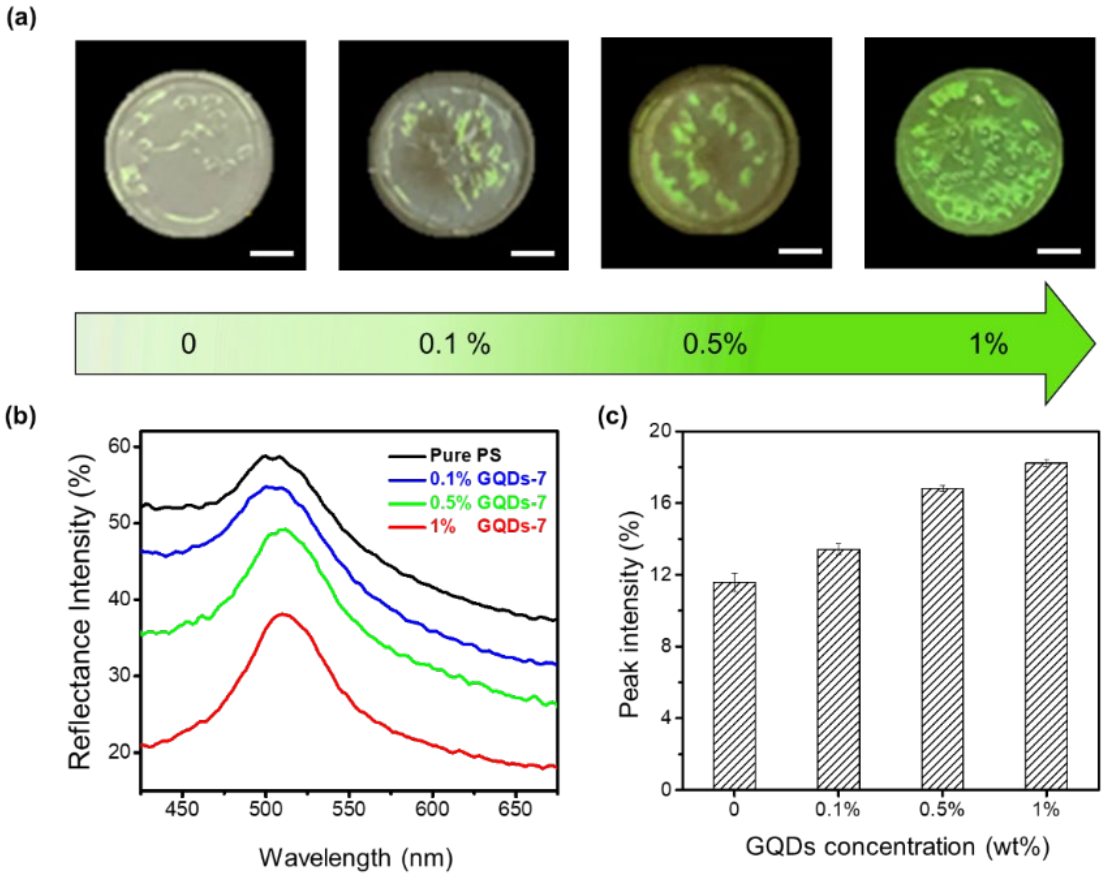

Figure 35. Enhanced PS photonic crystals with various GQDs concentrations.

After green color PhCs enhancement, full visible spectra range color enhancement PhCs was also achieved through tuning the particle size of PhCs and the concentration of GQDs. The enhanced coloring of PS nanoparticles with GQDs was shown in Figure 36. In addition to green color group PhCs, blue, red and cyan enhanced PhCs with GQDs (Figure 36a) were also fabricated by drop-casting method. Four different sizes of uniform PS nanoparticles were synthesized and the diameters were measured as 192, 214, 274 and 396 nm from both SEM and DLS measurement. The corresponding PhCs films were aligned in four rows showing blue, green, red and cyan structural color groups. Each row

in Figure 36a represented a color group PS/GQDs photonic crystal films with variable GQDs additive concentration. The GQDs concentration was 0 wt%, 0.1 wt%, 0.25 wt%, 0.5 wt% and 1 wt%. The color visibility also increased each row from left to right, with the leftmost palest and the rightmost representing best brilliant structural color.

The reflectance peaks of four PS/GQDs films conducted through UV-vis spectrofluorometer was 446 nm, 510 nm, 640 nm, and 472 nm, as shown in Figure 36b. The PS/GQD films compositions were PS nanoparticles (192, 214, 274 and 396nm) with 1 wt% GQDs-7. The peaks data achieved could be compared with theoretical calculations. For the visible wavelength range photonic crystals, the reflectance mechanism of photonic crystals could be explained through Bragg's law. The reflectance wavelength of light λ could be represented below:

$$\lambda = \frac{1}{K} * 2\sqrt{\frac{2}{3}}\, D_{c-c}\sqrt{n_{effective}^2 - \sin^2\theta} \tag{8}$$

where λ is the reflectance wavelength of light, K is the order of reflection, D_{c-c} is the distance between two nearest nanoparticles, $n_{effective}$ is the effective refractive index of photonic crystal and θ is the incident angle. Accordingly, in PS/GQDs enhanced photonic crystals composites, $n_{effective}$ would consist of the refractive index of the PS nanoparticles, the PS interstitial space air and GQDs. The effective refractive index could be defined below:

$$n_{effective} = \emptyset_{PS} * n_{PS} + \emptyset_{Air} * n_{Air} + \emptyset_{GQDs} * n_{GQDs} \tag{9}$$

where n_{PS}, n_{Air} and n_{GQDs} represented refractive index of PS (n= 1.59), air (n= 1) and GQDs (n= 1.88), respectively. Φ_{PS}, Φ_{Air} and Φ_{GQDs} represented the volume fraction of PS (Φ= 74%), air (Φ= 25%) and GQDs (Φ= 1%). $n_{effective}$ was herein calculated as 1.4454. To calculate reflectance wavelength λ of PS/GQDs photonic crystals, D_{c-c} was considered equal to the size of the average PS nanoparticle (192, 214, 274, and 396 nm) due to close packed FCC structure. The incident angle θ was 0° because the incident angle was perpendicular to the surface. The refractive index $n_{effective}$ was 1.4454, and order of Bragg reflection K is integer 1 or 2. The calculated λ of PS/GQDs films (PS sizes: 192, 214, 274, and 396 nm) were 453.18 nm, 505.11 nm, 646.73 nm, and 467.35 nm, respectively. The calculated peaks closely matched with experimental test wavelengths and proved their credibility after comparison. From the simulated calculation of Bragg's law and UV-vis characterization, it was found that the colors of blue, green, and red thin films resulted from the 1st order of Bragg reflection, and cyan color thin film resulted from the 2nd order of Bragg reflection.

The PS/GQDs enhanced photonic crystals with various structural colors could be directly utilized as photonic inks for painting or calligraphy. Figure 36c represented photonic ink writings and drawings on diverse substrates like paper, silicon wafer and glass. And Figure 36d showed the photograph of photonic ink Chinese calligraphy, which was a Chinese Tang dynasty eternally famous poem "On the Stork Tower" by poet Zhihuan Wang. The results exhibited the great potential of enhanced photonic crystals in painting and printing areas. One ink brush was used for all writings and drawings in Figure 36c and Figure 36d.

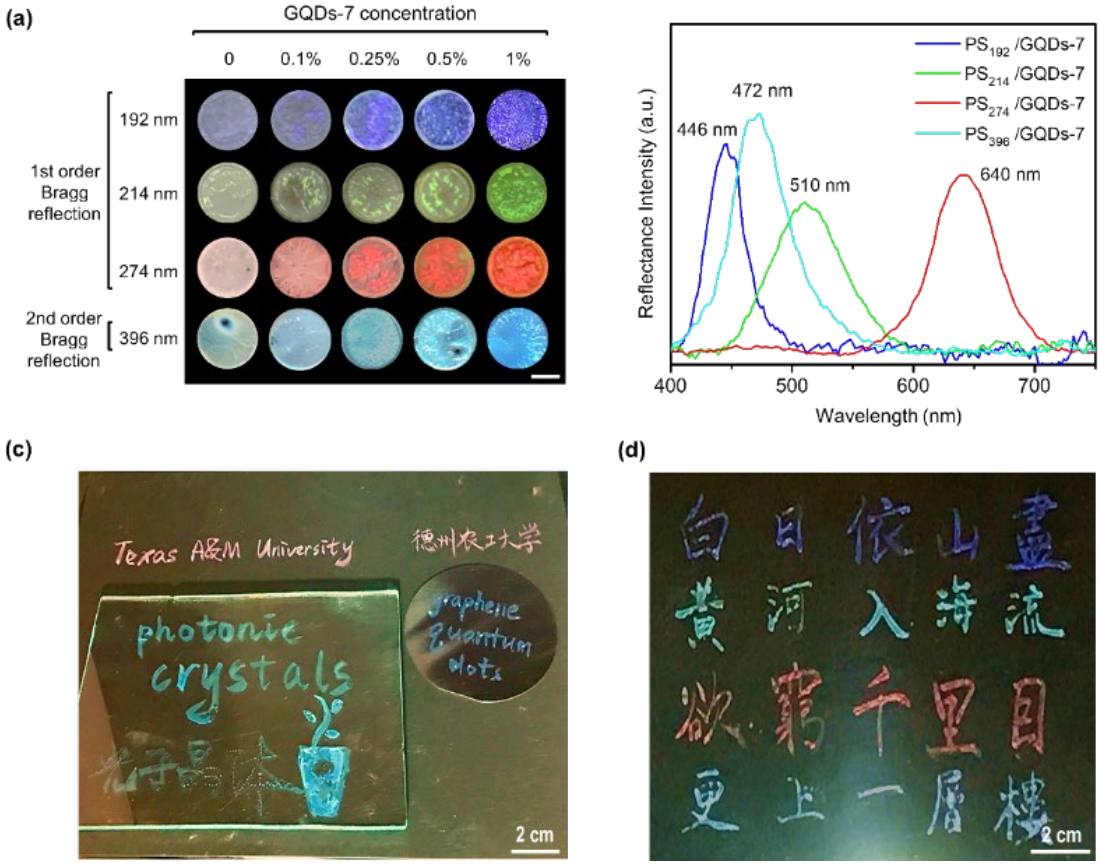

Figure 36. Coloring of PS nanoparticles with GQDs.

6.5 Summary

In conclusion, 0D sphere and 2D nanoplate synthetic photonic crystals inspired by nature have been achieved. It was worth noting that 2D nematic photonic liquid crystal structural color was achieved in the ZrP nanoplate suspension. Different from 0D photonic crystals built by long-range periodic arrangement, the structural color of 2D ZrP photonic liquid crystals comes from short-ranged nematic order. The 2D nanoplate photonic liquid crystal which is a fluid and highly dependent on ZrP concentration, both have the liquid

crystal and photonic crystal behavior. The structural color will have a redshift when decreasing ZrP volume concentration due to the increasing lattice spacing. Through tuning concentration, full visible wavelength structural colors of 2D ZrP photonic crystals were fabricated. The colorful nematic hydrogels were accordingly fabricated for potential flexible wearable sensors and photo-responsive devices. Besides, the colloidal photonic crystals with enhanced color visibility were accomplished through adding black additives and could reduce incoherent scattering and background light of resulting colloidal PhCs.

CHAPTER VII

CONCLUSIONS AND FUTURE RECOMMENDATIONS

7.1 Conclusions

This dissertation research investigated controlled self-assembly of 2D ZrP liquid crystal and its phase transition behaviors. Highly anisotropy and small aspect ratio of ZrP nanoplate is a good study model to investigate the 2D liquid crystal phase transition. The optical visualization of 2D liquid crystals is beneficial to observe the real-time orientation of 2D colloids. The processing and optical performance relation of the ZrP liquid crystals have been studied and can promote to other 2D colloidal systems.

The following points summarize the major findings:

1) The self-assembly of 2D colloids is highly affected by material internal properties like aspect ratios. The phase transition behavior of 2D ZrP liquid crystals is dependent on the nanoplate aspect ratio. The smaller nanoplate aspect ratio has a smaller volume fraction and will earlier reach the I-N phase transition point accompanying increasing concentration. Moreover, the higher nanoplate aspect ratio will achieve the nematic phase sooner and form 2D oriented structures (Chapter IV).

2) The self-assembly of 2D colloids is dependent on external fields like temperature gradient fields. An external temperature-gradient-induced formation of 2D liquid crystals was firstly deployed for studying I-N-S phase transition behaviors. The appearance of nematic and smectic of 2D nanoplates is indicative of thermophoretic effects, moving from cold end to hot end. And the natural convection speeds up the process. The external temperature-controlled formation of liquid crystals is the first time achieved in the colloidal system. It has excellent potential in physical engineering and bioengineering (Chapter V).

3) Inspired by nature, the structural colors of nematic photonic liquid crystals were achieved in the 2D ZrP nanoplate suspension. Unlike the structural colors of 0D photonic crystals built by long-range periodic FCC arrangement, the structural colors of 2D ZrP photonic liquid crystals come from the short-range nematic order structure. The 2D nanoplate photonic liquid crystals are fluid and dependent on ZrP concentration. The structural color will have a redshift when decreasing ZrP volume concentration due to the increasing lattice spacing. Through tuning concentration, full visible spectra of the structural colors of 2D ZrP photonic crystals were synthesized. The colorful nematic hydrogels were also fabricated for potential flexible wearable sensors and photo-responsive devices (Chapter VI).

7.2 Future recommendations

Based on our liquid crystal research findings, more synthesis, nucleation & growth methods and applications of 2D colloidal liquid crystals can be investigated for future research directions:

1) 2D liquid crystals, including but not limited to ZrP liquid crystals and tactoids droplets formed on earth, could perform different phase behaviors under microgravity in space. The nucleation & growth rate of tactoids and their morphology might accordingly change. The special polarized optical microscope could be designed and operated to observe vertically displayed samples, as shown in Figure 37. The capillary was vertically placed in the vertical stage (red area) to observe the gravity effect on the growth of 2D liquid crystals. Some results were shown in Figure 38, which were the polarized optical microscopy images of ZrP suspension (complete nematic phase) growth through time. The ZrP sample was injected in a vertically displayed capillary and manually stirred for homogenization. Tactoids were found to form, then grew larger and started for sedimentation. More tests with various aspect ratios and volume fractions could be performed and compared with the samples for future microgravity test.

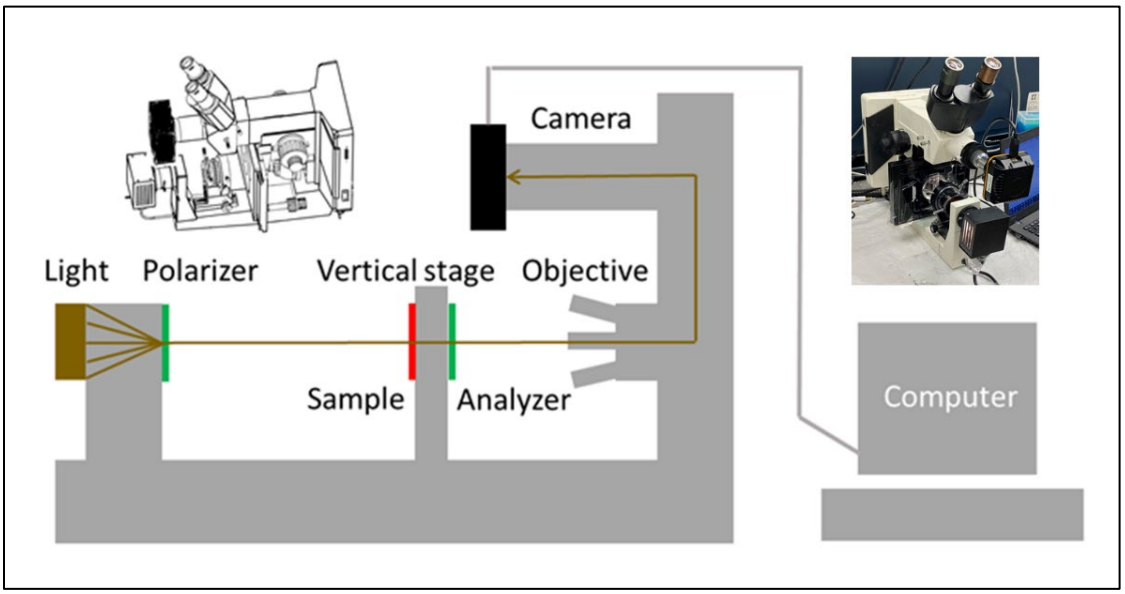

Figure 37. Schematic illustration and photograph for polarized optical microscope for vertically displayed sample observation.

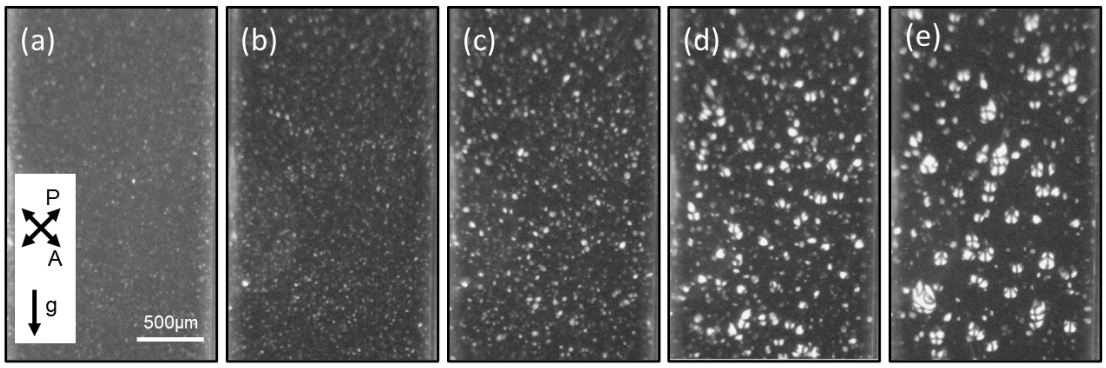

Figure 38. Cross-polarized optical microscopy images of nematic suspension of nanoplates with time (a) 250 seconds; (b) 1000 seconds; (c) 2000 seconds; (d) 3000 seconds (e) 4500 seconds.

2) Precisely controlled liquid crystals printing with ultrafine linewidth could be achieved through laser deposition printing. The liquid crystal deposition can be manually tuned and printed on different substrates with laser deposition printing. The laser could precisely control the temperature speed and deposition location. Figure 39 shows the deposition process when a laser is operating. The ZrP nanoplate nematic suspension has reoriented under the control of laser deposition (Figure 39a). The laser deposition location will get adjusted by the specific program, and different patterns with ultrafine linewidth liquid crystals printing could be achieved. Figure 39b is the polarized microscopy image of the preset laser deposition butterfly pattern. The controlled laser printing offers a new liquid crystal growth control method and could promote to liquid crystal display designs.

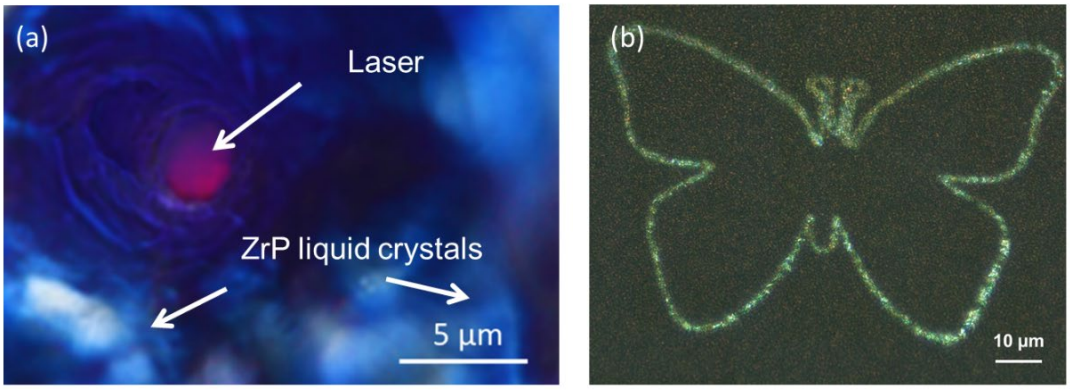

Figure 39. Cross-polarized microscopy photographs of (a) laser deposition process (b) ultrafine linewidth butterfly pattern by laser deposition.

3) Thermophoretic microfluidic channels could be designed for studying liquid crystal phase transitions. It would be better to observe the movement of nematic liquid crystals and reduce the convection effect. The initial experiment setup containers in the project are vials or capillaries, which have relatively large thickness and height, not easy for real-time observation or tuning. Building microfluidic channels will benefit the study for thermophoresis of nanoplate liquid crystals, and one simple schematic drawing is shown in Figure 40. Temperature fields are set between two sides of channels. ZrP nanoplate liquid crystals go through the channels and a polarized optical microscope records the movement with camera system from thermophoretic area in (a) to (f) and the outlet area (g) and (h). It could be helpful in the biomedical and drug delivery system.

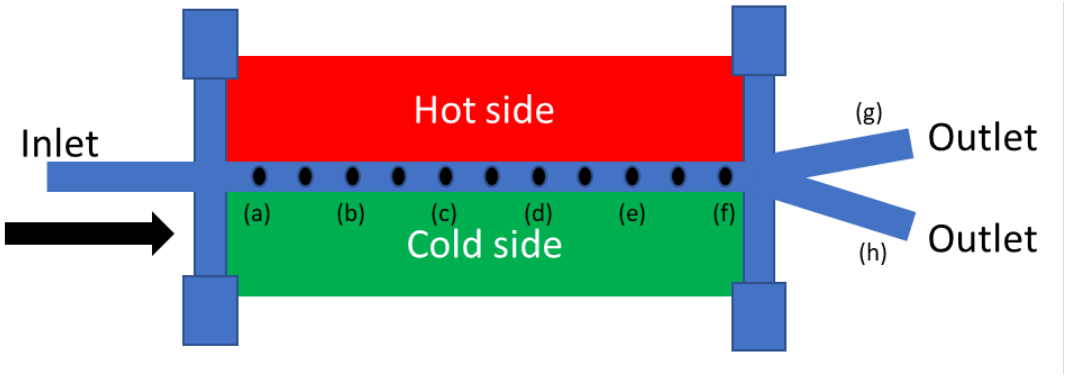

Figure 40. Schematic drawing for thermophoretic microfluidic setup.

4) The optoelectronic devices could be integrated with our 2D colloidal liquid crystals for more functioning applications. Now multiple researches are working on wearable and implantable devices in biomedical areas. Figure 41a presented the fabrication process of photonic liquid crystals on wearable devices, the photonic liquid crystal was attached in the polymers and released to fabricate the device. Figure 41b showed the complete visible spectrum structural colors fabricated by 2D ZrP suspension with self-assembly. If the photonic liquid crystals in Figure 41b could be fabricated uniformly in the designated substrate in Figure 41c, the following PDMS could cover, crosslink, and released to get the miniaturized soft device. The biocompatibility of ZrP photonic liquid crystals, including solvent and ZrP nanoplates will be considered for bio-related applications.

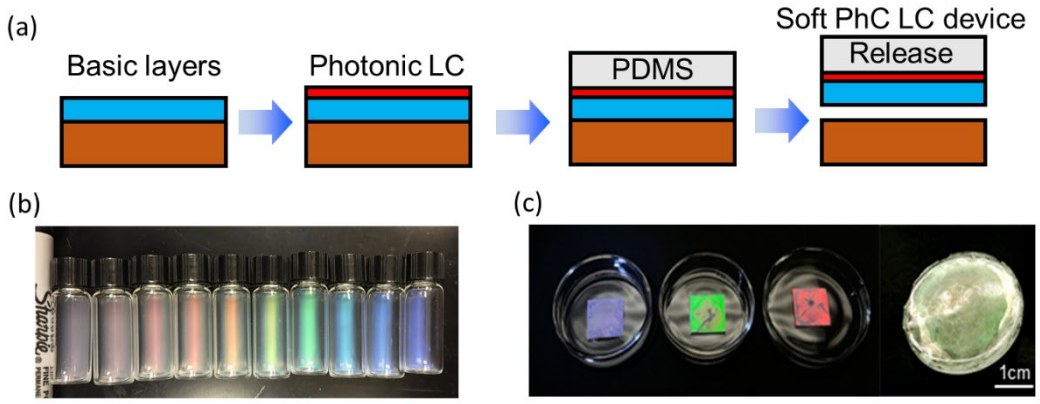

Figure 41. (a) Schematic illustration of making PDMS soft flexible filter. (b) Photograph of various structural colors fabricated by 2D nanoplate photonic liquid crystals. (c) ZrP photonic crystals on substrate and PDMS.

REFERENCES

1. Schmid, G., *Clusters and colloids: from theory to applications*. John Wiley & Sons: **2008**.

2. Dhont, J. K. G., *An introduction to dynamics of colloids*. Elsevier: **1996**.

3. Aastuen, D. J. W.; Clark, N. A.; Cotter, L. K.; Ackerson, B. J., Nucleation and growth of colloidal crystals. *Physical review letters* **1986,** *57* (14), 1733.

4. van Blaaderen, A., Chemistry: Colloidal molecules and beyond. *Science* **2003,** *301* (5632), 470-471.

5. Li, F.; Josephson, D. P.; Stein, A., Colloidal assembly: the road from particles to colloidal molecules and crystals. *Angewandte Chemie International Edition* **2011,** *50* (2), 360-388.

6. Choi, P. T. L.; Yip, G.; Quinonez, L. G.; Cook, D. J., Crystalloids vs. colloids in fluid resuscitation: a systematic review. *Critical care medicine* **1999,** *27* (1), 200-210.

7. He, L.; Ye, J.; Shuai, M.; Zhu, Z.; Zhou, X.; Wang, Y.; Li, Y.; Su, Z.; Zhang, H.; Chen, Y.; Liu, Z.; Cheng, Z.; Bao, J., Graphene oxide liquid crystals for reflective displays without polarizing optics. *Nanoscale* **2015,** *7* (5), 1616-22.

8. Park, J. Y.; Davies, J. E., Red blood cell and platelet interactions with titanium implant surfaces. *Clinical oral implants research* **2000,** *11* (6), 530-539.

9. Yan, Z.; Fu, L.; Yang, H., Functionalized 2D clay derivative: hybrid nanosheets with unique lead sorption behaviors and interface structure. *Advanced Materials Interfaces* **2018,** *5* (4), 1700934.

10. Akinwande, D.; Brennan, C. J.; Bunch, J. S.; Egberts, P.; Felts, J. R.; Gao, H.; Huang, R.; Kim, J.-S.; Li, T.; Li, Y., A review on mechanics and mechanical properties of 2D materials—Graphene and beyond. *Extreme Mechanics Letters* **2017,** *13*, 42-77.

11. Sun, D.; Sue, H.-J.; Cheng, Z.; Martínez-Ratón, Y.; Velasco, E., Stable smectic phase in suspensions of polydisperse colloidal platelets with identical thickness. *Physical Review E* **2009,** *80* (4), 041704.

12. Yun, T.; Jeong, G. H.; Padmajan Sasikala, S.; Kim, S. O., 2D graphene oxide liquid crystal for real-world applications: Energy, environment, and antimicrobial. *APL Materials* **2020,** *8* (7), 070903.

13. Guo, C.; Wang, J.; Cao, F.; Lee, R. J.; Zhai, G., Lyotropic liquid crystal systems in drug delivery. *Drug discovery today* **2010,** *15* (23-24), 1032-1040.

14. Vertogen, G.; De Jeu, W. H., *Thermotropic liquid crystals, fundamentals*. Springer Science & Business Media: **2012**; Vol. 45.

15. Neto, A. M. F.; Salinas, S. R. A., *The physics of lyotropic liquid crystals: phase transitions and structural properties*. Oxford University Press on Demand: **2005**; Vol. 62.

16. Chandrasekhar, S.; Ranganath, G. S., Discotic liquid crystals. *Reports on Progress in Physics* **1990,** *53* (1), 57.

17. Chandrasekhar, S., Discotic liquid crystals. A brief review. *Liquid Crystals* **1993,** *14* (1), 3-14.

18. Onsager, L., The effects of shape on the interaction of colloidal particles. *Annals of the New York Academy of Sciences* **1949,** *51* (4), 627-659.

19. Mozumder, A., Effect of an external electric field on the yield of free ions. I General results from the Onsager theory. *The Journal of Chemical Physics* **1974,** *60* (11), 4300-4304.

20. Tjipto‐Margo, B.; Evans, G. T., The Onsager theory of the isotropic–nematic liquid crystal transition: Incorporation of the higher virial coefficients. *The Journal of chemical physics* **1990,** *93* (6), 4254-4265.

21. Cuetos, A.; Martínez-Haya, B., Columnar phases of discotic spherocylinders. *The Journal of chemical physics* **2008,** *129* (21), 214706.

22. Kim, J. E.; Han, T. H.; Lee, S. H.; Kim, J. Y.; Ahn, C. W.; Yun, J. M.; Kim, S. O., Graphene oxide liquid crystals. *Angewandte Chemie* **2011,** *123* (13), 3099-3103.

23. Paineau, E.; Antonova, K.; Baravian, C.; Bihannic, I.; Davidson, P.; Dozov, I.; Impéror-Clerc, M.; Levitz, P.; Madsen, A.; Meneau, F., Liquid-crystalline nematic phase in aqueous suspensions of a disk-shaped natural beidellite clay. *The Journal of Physical Chemistry B* **2009,** *113* (48), 15858-15869.

24. van der Kooij, F. M.; Kassapidou, K.; Lekkerkerker, H. N. W., Liquid crystal phase transitions in suspensions of polydisperse plate-like particles. *Nature* **2000,** *406* (6798), 868-871.

25. Shuai, M., *Synthesis and Liquid Crystal Phase Transitions of Zirconium Phosphate Disks*. **2013**.

26. Cheng, Y.; Chuah, G. K., The synthesis and applications of α-zirconium phosphate. *Chinese Chemical Letters* **2020,** *31* (2), 307-310.

27. Xiao, H.; Liu, S., Zirconium phosphate (ZrP)-based functional materials: Synthesis, properties and applications. *Materials & Design* **2018,** *155*, 19-35.

28. Kaschak , D. M.; Johnson, S. A.; Hooks, D. E.; Kim, H.-N.; Ward, M. D.; Mallouk, T. E., Chemistry on the Edge: A Microscopic Analysis of the Intercalation, Exfoliation, Edge Functionalization, and Monolayer Surface Tiling Reactions of α-Zirconium Phosphate. *Journal of the American Chemical Society* **1998,** *120* (42), 10887-10894.

29. Mejia, A. F.; Chang, Y.-W.; Ng, R.; Shuai, M.; Mannan, M. S.; Cheng, Z., Aspect ratio and polydispersity dependence of isotropic-nematic transition in discotic suspensions. *Physical Review E* **2012,** *85* (6).

30. Clearfield, A.; Duax, W. L.; Medina, A. S.; Smith, G. D.; Thomas, J. R., Mechanism of ion exchange in crystalline zirconium phosphates. I. Sodium ion exchange of. alpha.-zirconium phosphate. *The Journal of Physical Chemistry* **1969,** *73* (10), 3424-3430.

31. Clearfield, A.; Stynes, J. A., The preparation of crystalline zirconium phosphate and some observations on its ion exchange behaviour. *Journal of Inorganic and Nuclear Chemistry* **1964,** *26* (1), 117-129.

32. Gura, V.; Macy, A. S.; Beizai, M.; Ezon, C.; Golper, T. A., Technical breakthroughs in the wearable artificial kidney (WAK). *Clinical Journal of the American Society of Nephrology* **2009,** *4* (9), 1441-1448.

33. Trobajo, C.; Khainakov, S. A.; Espina, A.; García, J. R., On the synthesis of α-zirconium phosphate. *Chemistry of materials* **2000,** *12* (6), 1787-1790.

34. Wang, X.; Zhang, L.; Yu, Y. H.; Jia, L.; Sam Mannan, M.; Chen, Y.; Cheng, Z., Nano-encapsulated PCM via Pickering Emulsification. *Sci Rep* **2015,** *5*, 13357.

35. Shuai, M.; Mejia, A. F.; Chang, Y.-W.; Cheng, Z., Hydrothermal synthesis of layered α-zirconium phosphate disks: control of aspect ratio and polydispersity for nano-architecture. *CrystEngComm* **2013,** *15* (10), 1970.

36. Sun, L.; Boo, W. J.; Sue, H.-J.; Clearfield, A., Preparation of α-zirconium phosphate nanoplatelets with wide variations in aspect ratios. *New J. Chem.* **2007,** *31* (1), 39-43.

37. Yu, Y. H.; Chen, Y. P.; Zeng, M.; Cheng, Z., Microwave-assisted rapid synthesis of hexagonal α-zirconium phosphate nanodisks as a Pickering emulsion stabilizer. *Mater. Lett.* **2016,** *163*, 158.

38. SooD, A. K., Structural ordering in colloidal suspensions. *Solid State Physics* **1991,** *45*, 1-73.

39. Zhang, D.; Gökce, B.; Barcikowski, S., Laser synthesis and processing of colloids: fundamentals and applications. *Chemical reviews* **2017,** *117* (5), 3990-4103.

40. Zhang, J.; Luijten, E.; Grzybowski, B. A.; Granick, S., Active colloids with collective mobility status and research opportunities. *Chemical Society Reviews* **2017,** *46* (18), 5551-5569.

41. Gasser, U., Crystallization in three-and two-dimensional colloidal suspensions. *Journal of Physics: Condensed Matter* **2009,** *21* (20), 203101.

42. Van Megen, W.; Underwood, S. M., The motions of particles in concentrated dispersions as observed by dynamic light scattering. *Langmuir* **1990,** *6* (1), 35-42.

43. Henderson, S. I.; Mortensen, T. C.; Underwood, S. M.; van Megen, W., Effect of particle size distribution on crystallisation and the glass transition of hard sphere colloids. *Physica A: Statistical Mechanics and its Applications* **1996,** *233* (1-2), 102-116.

44. Harland, J. L.; Van Megen, W., Crystallization kinetics of suspensions of hard colloidal spheres. *Physical Review E* **1997,** *55* (3), 3054.

45. Martin, S.; Bryant, G.; Van Megen, W., Crystallization kinetics of polydisperse colloidal hard spheres: experimental evidence for local fractionation. *Physical Review E* **2003,** *67* (6), 061405.

46. Mejia, A. F.; Chang, Y. W.; Ng, R.; Shuai, M.; Mannan, M. S.; Cheng, Z., Aspect ratio and polydispersity dependence of isotropic-nematic transition in discotic suspensions. *Phys Rev E Stat Nonlin Soft Matter Phys* **2012,** *85* (6 Pt 1), 061708.

47. He, P.; Mejia, A. F.; Cheng, Z.; Sun, D.; Sue, H.-J.; Dinair, D. S.; Marquez, M. J. P. R. E., Hindrance function for sedimentation and creaming of colloidal disks. **2010,** *81* (2), 026310.

48. Bates, M. A.; Frenkel, D., Nematic–isotropic transition in polydisperse systems of infinitely thin hard platelets. *The Journal of chemical physics* **1999,** *110* (13), 6553-6559.

49. Sullivan, M.; Zhao, K.; Harrison, C.; Austin, R. H.; Megens, M.; Hollingsworth, A.; Russel, W. B.; Cheng, Z.; Mason, T.; Chaikin, P. M., Control of colloids with gravity, temperature gradients, and electric fields. *Journal of Physics: Condensed Matter* **2002,** *15* (1), S11.

50. Inadomi, T.; Ikeda, S.; Okumura, Y.; Kikuchi, H.; Miyamoto, N., Photo‐Induced Anomalous Deformation of Poly (N‐Isopropylacrylamide) Gel Hybridized with an

Inorganic Nanosheet Liquid Crystal Aligned by Electric Field. *Macromolecular rapid communications* **2014,** *35* (20), 1741-1746.

51. Nakato, T.; Nakamura, K.; Shimada, Y.; Shido, Y.; Houryu, T.; Iimura, Y.; Miyata, H., Electrooptic Response of Colloidal Liquid Crystals of Inorganic Oxide Nanosheets Prepared by Exfoliation of a Layered Niobate. *The Journal of Physical Chemistry C* **2011,** *115* (18), 8934-8939.

52. Nakato, T.; Nono, Y.; Mouri, E.; Nakata, M., Panoscopic organization of anisotropic colloidal structures from photofunctional inorganic nanosheet liquid crystals. *Physical Chemistry Chemical Physics* **2014,** *16* (3), 955-962.

53. Paineau, E.; Antonova, K.; Baravian, C.; Bihannic, I.; Davidson, P.; Dozov, I.; Impéror-Clerc, M.; Levitz, P.; Madsen, A.; Meneau, F.; Michot, L. J., Liquid-Crystalline Nematic Phase in Aqueous Suspensions of a Disk-Shaped Natural Beidellite Clay. *The Journal of Physical Chemistry B* **2009,** *113* (48), 15858-15869.

54. Chen, M.; Shinde, A.; Wang, L.; Ye, C.; Zeng, M.; Yan, Q.; Lin, P.; Chen, Y.; Cheng, Z., Rainbows in a vial: controlled assembly of 2D colloids in two perpendicular external fields. *2D Materials* **2019,** *6* (2), 025031.

55. Luo, J.; Zeng, M.; Peng, B.; Tang, Y.; Zhang, L.; Wang, P.; He, L.; Huang, D.; Wang, L.; Wang, X.; Chen, M.; Lei, S.; Lin, P.; Chen, Y.; Cheng, Z., Electrostatic-Driven Dynamic Jamming of 2D Nanoparticles at Interfaces for Controlled Molecular Diffusion. *Angewandte Chemie* **2018,** *130* (36), 11926-11931.

56. Li, B.-X.; Borshch, V.; Shiyanovskii, S. V.; Liu, S.-B.; Lavrentovich, O. D., Electro-optic switching of dielectrically negative nematic through nanosecond electric modification of order parameter. *Applied Physics Letters* **2014,** *104* (20), 201105.

57. Sano, K.; Kim, Y. S.; Ishida, Y.; Ebina, Y.; Sasaki, T.; Hikima, T.; Aida, T., Photonic water dynamically responsive to external stimuli. *Nature communications* **2016,** *7*, 12559.

58. Frka‐Petesic, B.; Radavidson, H.; Jean, B.; Heux, L., Dynamically controlled iridescence of cholesteric cellulose nanocrystal suspensions using electric fields. *Advanced Materials* **2017,** *29* (11), 1606208.

59. De Groot, S. R.; Mazur, P., Non-equilibrium thermodynamics. Courier Corporation: North Chelmsford, **2013**; pp 1-83.

60. Chapman, S., The characteristics of thermal diffusion. *Proc. R. Soc. Lond. A* **1940,** *177* (968), 38-62.

61. Chapman, S., Thermal diffusion in ionized gases. *Proceedings of the Physical Society* **1958,** *72* (3), 353.

62. Bringuier, E.; Bourdon, A., Kinetic theory of colloid thermodiffusion. *Physica A: Statistical Mechanics and its Applications* **2007,** *385* (1), 9-24.

63. Geelhoed, P. F.; Lindken, R.; Westerweel, J., Thermophoretic separation in microfluidics. *Chemical Engineering Research and Design* **2006,** *84* (5), 370-373.

64. Vigolo, D.; Rusconi, R.; Stone, H. A.; Piazza, R., Thermophoresis: microfluidics characterization and separation. *Soft Matter* **2010,** *6* (15), 3489-3493.

65. Giddings, J. C., Field-flow fractionation: analysis of macromolecular, colloidal, and particulate materials. *Science* **1993,** *260* (5113), 1456-1465.

66. Duhr, S.; Braun, D., Optothermal molecule trapping by opposing fluid flow with thermophoretic drift. *Physical review letters* **2006,** *97* (3), 038103.

67. Cheng, Z. D.; Russell, W. B.; Chaikin, P. M., Controlled growth of hard-sphere colloidal crystals. *Nature* **1999,** *401* (6756), 893-895.

68. Kleman, M.; Lavrentovich, O. D., Topological point defects in nematic liquid crystals. *Philosophical Magazine* **2006,** *86* (25-26), 4117-4137.

69. Mohebbi, R.; Mehryan, S. A. M.; Izadi, M.; Mahian, O., Natural convection of hybrid nanofluids inside a partitioned porous cavity for application in solar power plants. *Journal of Thermal Analysis and Calorimetry* **2019**, 1-15.

70. Bhuvaneswari, M.; Ganesan, P. B.; Sivasankaran, S.; Viswanathan, K. K., Effect of variable fluid properties on natural convection of nanofluids in a cavity with linearly varying wall temperature. *Mathematical Problems in Engineering* **2015,** *2015*.

71. Choubineh, N.; Jannesari, H.; Kasaeian, A., Experimental study of the effect of using phase change materials on the performance of an air-cooled photovoltaic system. *Renewable and Sustainable Energy Reviews* **2019,** *101*, 103-111.

72. Sheikholeslami, M., Numerical investigation of nanofluid free convection under the influence of electric field in a porous enclosure. *Journal of Molecular Liquids* **2018,** *249*, 1212-1221.

73. Ho, C.-J.; Chen, M. W.; Li, Z. W., Numerical simulation of natural convection of nanofluid in a square enclosure: effects due to uncertainties of viscosity and thermal

conductivity. *International Journal of Heat and Mass Transfer* **2008,** *51* (17-18), 4506-4516.

74. Jayaraj, S.; Dinesh, K. K.; Pillai, K. L., Thermophoresis in natural convection with variable properties. *Heat and Mass Transfer* **1999,** *34* (6), 469-475.

75. Chang, B. H.; Mills, A. F.; Hernandez, E., Natural convection of microparticle suspensions in thin enclosures. *International Journal of Heat and Mass Transfer* **2008,** *51* (5-6), 1332-1341.

76. Wang, X.; Zhao, D.; Diaz, A.; Medina, I. B. N.; Wang, H.; Cheng, Z., Thermo-sensitive discotic colloidal liquid crystals. *Soft Matter* **2014,** *10* (39), 7692-7695.

77. Wiegand, S., Thermal diffusion in liquid mixtures and polymer solutions. *Journal of Physics: Condensed Matter* **2004,** *16* (10), R357.

78. Ruckenstein, E., Can phoretic motions be treated as interfacial tension gradient driven phenomena? *Journal of Colloid and Interface Science* **1981,** *83* (1), 77-81.

79. Piazza, R.; Parola, A., Thermophoresis in colloidal suspensions. *Journal of Physics: Condensed Matter* **2008,** *20* (15), 153102.

80. Tan, Z.; Yang, M.; Ripoll, M., Anisotropic thermophoresis. *Soft Matter* **2017,** *13* (40), 7283-7291.

81. Putnam, S. A.; Cahill, D. G., Transport of Nanoscale Latex Spheres in a Temperature Gradient. *Langmuir* **2005,** *21* (12), 5317-5323.

82. Würger, A., Transport in charged colloids driven by thermoelectricity. *Physical review letters* **2008,** *101* (10), 108302.

83. Helfand, E.; Kirkwood, J. G., Theory of the heat of transport of electrolytic solutions. *The Journal of Chemical Physics* **1960,** *32* (3), 857-866.

84. van der Kooij, F. M.; Kassapidou, K.; Lekkerkerker, H. N., Liquid crystal phase transitions in suspensions of polydisperse plate-like particles. *Nature* **2000,** *406* (6798), 868-871.

85. Shinde, A.; Wang, X.; Cheng, Z., Aspect Ratio Dependence of Isotropic-Nematic Phase Separation of Nanoplates in Gravity. *Gravitational and Space Research* **2016,** *4* (1).

86. Iacopini, S.; Rusconi, R.; Piazza, R., The “macromolecular tourist": Universal temperature dependence of thermal diffusion in aqueous colloidal suspensions. *The European Physical Journal E* **2006,** *19* (1), 59-67.

87. Braibanti, M.; Vigolo, D.; Piazza, R., Does thermophoretic mobility depend on particle size? *Physical review letters* **2008,** *100* (10), 108303.

88. Duhr, S.; Braun, D., Thermophoretic depletion follows Boltzmann distribution. *Physical review letters* **2006,** *96* (16), 168301.

89. Talbot, E. L.; Kotar, J.; Parolini, L.; Di Michele, L.; Cicuta, P., Thermophoretic migration of vesicles depends on mean temperature and head group chemistry. *Nature communications* **2017,** *8*, 15351.

90. Saxena, V.; Diaz, A.; Clearfield, A.; Batteas, J. D.; Hussain, M. D., Zirconium phosphate nanoplatelets: a biocompatible nanomaterial for drug delivery to cancer. *Nanoscale* **2013,** *5* (6), 2328-2336.

91. Díaz, A.; Saxena, V.; González, J.; David, A.; Casañas, B.; Carpenter, C.; Batteas, J. D.; Colón, J. L.; Clearfield, A.; Hussain, M. D., Zirconium phosphate nano-

platelets: a novel platform for drug delivery in cancer therapy. *Chemical Communications* **2012,** *48* (12), 1754-1756.

92. Park, H.-S.; Kang, S.-W.; Tortora, L.; Nastishin, Y.; Finotello, D.; Kumar, S.; Lavrentovich, O. D., Self-assembly of lyotropic chromonic liquid crystal sunset yellow and effects of ionic additives. *The Journal of Physical Chemistry B* **2008,** *112* (51), 16307-16319.

93. Cheng, Z.; Russel, W. B.; Chaikin, P. M., Controlled growth of hard-sphere colloidal crystals. *Nature* **1999,** *401* (6756), 893-895.

94. Piazza, R., 'Thermal forces': colloids in temperature gradients. *Journal of Physics: Condensed Matter* **2004,** *16* (38), S4195.

95. Giglio, M.; Vendramini, A., Soret-type motion of macromolecules in solution. *Physical Review Letters* **1977,** *38* (1), 26.

96. Lüsebrink, D.; Ripoll, M., Collective thermodiffusion of colloidal suspensions. *The Journal of chemical physics* **2012,** *137* (19), 194904.

97. Pet'kov, V. I.; Asabina, E. A.; Markin, A. V.; Kir'yanov, K. V., Calorimetric study of sodium-rich zirconium phosphate. *Thermochimica acta* **2003,** *403* (2), 185-196.

98. Shinde, A.; Wang, X.; Guerra, R.; Cheng, Z., Experimental measurement of equation of state for isotropic suspension of nanoplates. *Bulletin of the American Physical Society* **2014,** *59*.

99. Shinde, A.; Wang, X.; Cheng, Z. In *Observation of large nematic domains of discotic liquid crystals*, APS Meeting Abstracts, **2015**.

100. Zeng, M.; Huang, D.; Wang, P.; King, D.; Peng, B.; Luo, J.; Lei, Q.; Zhang, L.; Wang, L.; Shinde, A., Autonomous Catalytic Nanomotors Based on 2D Magnetic Nanoplates. *ACS Applied Nano Materials* **2019,** *2* (3), 1267-1273.

101. Sørensen, B. E., A revised Michel-Lévy interference colour chart based on first-principles calculations. *European Journal of Mineralogy* **2013,** *25* (1), 5-10.

102. Vukusic, P.; Sambles, J.; Lawrence, C., Structural colour: Colour mixing in wing scales of a butterfly. *Nature* **2000,** *404* (6777), 457-457.

103. Siddique, R. H.; Vignolini, S.; Bartels, C.; Wacker, I.; Hölscher, H., Colour formation on the wings of the butterfly Hypolimnas salmacis by scale stacking. *Scientific reports* **2016,** *6*, 36204.

104. Pinheiro, C. E.; Freitas, A. V.; Campos, V. C.; DeVries, P. J.; Penz, C. M., Both Palatable and Unpalatable Butterflies Use Bright Colors to Signal Difficulty of Capture to Predators. *Neotrop Entomol* **2016,** *45* (2), 107-13.

105. Kinoshita, S.; Yoshioka, S., Structural colors in nature: the role of regularity and irregularity in the structure. *Chemphyschem* **2005,** *6* (8), 1442-59.

106. Potyrailo, R. A.; Ghiradella, H.; Vertiatchikh, A.; Dovidenko, K.; Cournoyer, J. R.; Olson, E., Morpho butterfly wing scales demonstrate highly selective vapour response. *Nature Photonics* **2007,** *1* (2), 123-128.

107. Wang, L.; Li, Q., Photochromism into nanosystems: towards lighting up the future nanoworld. *Chemical Society Reviews* **2018**.

108. Hanlon, R., Cephalopod dynamic camouflage. *Current Biology* **2007,** *17* (11), R400-R404.

109. Mather, J. A., Cephalopod skin displays: from concealment to communication. *Evolution of communication systems* **2004**, 193-214.

110. Stavenga, D. G.; Leertouwer, H. L.; Wilts, B. D., Coloration principles of nymphaline butterflies - thin films, melanin, ommochromes and wing scale stacking. *J Exp Biol* **2014,** *217* (Pt 12), 2171-80.

111. Wilts, B. D.; Trzeciak, T. M.; Vukusic, P.; Stavenga, D. G., Papiliochrome II pigment reduces the angle dependency of structural wing colouration in nireus group papilionids. *Journal of Experimental Biology* **2012,** *215* (5), 796-805.

112. Chung, K.; Yu, S.; Heo, C. J.; Shim, J. W.; Yang, S. M.; Han, M. G.; Lee, H. S.; Jin, Y.; Lee, S. Y.; Park, N.; Shin, J. H., Flexible, angle-independent, structural color reflectors inspired by morpho butterfly wings. *Adv Mater* **2012,** *24* (18), 2375-9.

113. Yoshioka, S.; Kinoshita, S., Structural or pigmentary? Origin of the distinctive white stripe on the blue wing of a Morpho butterfly. *Proc Biol Sci* **2006,** *273* (1583), 129-34.

114. Kinoshita, S.; Yoshioka, S.; Miyazaki, J., Physics of structural colors. *Reports on Progress in Physics* **2008,** *71* (7), 076401.

115. Xiao, M.; Li, Y.; Allen, M. C.; Deheyn, D. D.; Yue, X.; Zhao, J.; Gianneschi, N. C.; Shawkey, M. D.; Dhinojwala, A., Bio-inspired structural colors produced via self-assembly of synthetic melanin nanoparticles. *ACS nano* **2015,** *9* (5), 5454-5460.

116. Xu, J.; Li, W.; Shen, P.; Li, Y.; Li, Y.; Deng, Y.; Zheng, Q.; Liu, Y.; Ding, Z.; Li, J.; Zheng, T., Microfluidic fabrication of photonic encoding magnetized silica microspheres for aptamer-based enrichment of Ochratoxin A. *Microchimica Acta* **2017,** *184* (10), 3755-3763.

117. Liu, G.; Zhou, L.; Wu, Y.; Wang, C.; Fan, Q.; Shao, J., The fabrication of full color P (St‐MAA) photonic crystal structure on polyester fabrics by vertical deposition self‐assembly. *Journal of Applied Polymer Science* **2015,** *132* (13).

118. De Angelis, R.; Venditti, I.; Fratoddi, I.; De Matteis, F.; Prosposito, P.; Cacciotti, I.; D'Amico, L.; Nanni, F.; Yadav, A.; Casalboni, M.; Russo, M. V., From nanospheres to microribbons: Self-assembled Eosin Y doped PMMA nanoparticles as photonic crystals. *J Colloid Interface Sci* **2014,** *414*, 24-32.

119. Wang, L.; Bisoyi, H. K.; Zheng, Z.; Gutierrez-Cuevas, K. G.; Singh, G.; Kumar, S.; Bunning, T. J.; Li, Q., Stimuli-directed self-organized chiral superstructures for adaptive windows enabled by mesogen-functionalized graphene. *Materials Today* **2017,** *20* (5), 230-237.

120. Ganter, P.; Lotsch, B. V., Photonic nanoarchitectonics with stimuli-responsive 2D materials. *Molecular Systems Design & Engineering* **2019,** *4* (3), 566-579.

121. Wang, M.; Zou, C.; Sun, J.; Zhang, L.; Wang, L.; Xiao, J.; Li, F.; Song, P.; Yang, H., Asymmetric tunable photonic bandgaps in self‐organized 3D nanostructure of polymer‐stabilized blue phase I modulated by voltage polarity. *Advanced Functional Materials* **2017,** *27* (46), 1702261.

122. Wang, L., Self-activating liquid crystal devices for smart laser protection. *Liquid Crystals* **2016,** *43* (13-15), 2062-2078.

123. Sano, K.; Kim, Y. S.; Ishida, Y.; Ebina, Y.; Sasaki, T.; Hikima, T.; Aida, T., Photonic water dynamically responsive to external stimuli. *Nature communications* **2016,** *7* (1), 1-9.

124. Li, P.; Wong, M.; Zhang, X.; Yao, H.; Ishige, R.; Takahara, A.; Miyamoto, M.; Nishimura, R.; Sue, H.-J., Tunable lyotropic photonic liquid crystal based on graphene oxide. *ACS photonics* **2014,** *1* (1), 79-86.

125. Yang, X.; Ge, D.; Wu, G.; Liao, Z.; Yang, S., Production of Structural Colors with High Contrast and Wide Viewing Angles from Assemblies of Polypyrrole Black Coated Polystyrene Nanoparticles. *ACS Appl Mater Interfaces* **2016,** *8* (25), 16289-95.

126. Yi, B.; Shen, H., Liquid-immune structural colors with angle-independence inspired from hollow melanosomes. *Chemical Communications* **2017,** *53* (66), 9234-9237.

127. Ge, D.; Yang, X.; Chen, Z.; Yang, L.; Wu, G.; Xia, Y.; Yang, S., Colloidal inks from bumpy colloidal nanoparticles for the assembly of ultrasmooth and uniform structural colors. *Nanoscale* **2017,** *9* (44), 17357-17363.

128. Ge, J.; Yin, Y., Magnetically responsive colloidal photonic crystals. *Journal of Materials Chemistry* **2008,** *18* (42), 5041-5045.

129. Ge, J.; Goebl, J.; He, L.; Lu, Z.; Yin, Y., Rewritable photonic paper with hygroscopic salt solution as ink. *Advanced Materials* **2009,** *21* (42), 4259-4264.

130. Zhang, Y.; Dong, B.; Chen, A.; Liu, X.; Shi, L.; Zi, J., Using cuttlefish ink as an additive to produce -non-iridescent structural colors of high color visibility. *Adv Mater* **2015,** *27* (32), 4719-24.

131. Cao, A.; Liu, Z.; Chu, S.; Wu, M.; Ye, Z.; Cai, Z.; Chang, Y.; Wang, S.; Gong, Q.; Liu, Y., A facile one‐step method to produce graphene–CdS quantum dot nanocomposites as promising optoelectronic materials. *Advanced materials* **2010,** *22* (1), 103-106.

132. Bacon, M.; Bradley, S. J.; Nann, T., Graphene quantum dots. *Particle & Particle Systems Characterization* **2014,** *31* (4), 415-428.

133. Li, X.; Rui, M.; Song, J.; Shen, Z.; Zeng, H., Carbon and graphene quantum dots for optoelectronic and energy devices: a review. *Advanced Functional Materials* **2015,** *25* (31), 4929-4947.

134. Peng, J.; Gao, W.; Gupta, B. K.; Liu, Z.; Romero-Aburto, R.; Ge, L.; Song, L.; Alemany, L. B.; Zhan, X.; Gao, G.; Vithayathil, S. A.; Kaipparettu, B. A.; Marti, A. A.; Hayashi, T.; Zhu, J. J.; Ajayan, P. M., Graphene quantum dots derived from carbon fibers. *Nano Lett* **2012,** *12* (2), 844-9.

135. Min, S.; Hou, J.; Lei, Y.; Ma, X.; Lu, G., Facile one-step hydrothermal synthesis toward strongly coupled TiO 2/graphene quantum dots photocatalysts for efficient hydrogen evolution. *Applied Surface Science* **2017,** *396*, 1375-1382.

136. Ge, J.; Lan, M.; Zhou, B.; Liu, W.; Guo, L.; Wang, H.; Jia, Q.; Niu, G.; Huang, X.; Zhou, H., A graphene quantum dot photodynamic therapy agent with high singlet oxygen generation. *Nature communications* **2014,** *5*, 4596.

137. Lin, L.; Zhang, S., Creating high yield water soluble luminescent graphene quantum dots via exfoliating and disintegrating carbon nanotubes and graphite flakes. *Chemical communications* **2012,** *48* (82), 10177-10179.

138. Miao, X.; Qu, D.; Yang, D.; Nie, B.; Zhao, Y.; Fan, H.; Sun, Z., Synthesis of carbon dots with multiple color emission by controlled graphitization and surface functionalization. *Advanced Materials* **2018,** *30* (1), 1704740.

139. Dong, Y.; Shao, J.; Chen, C.; Li, H.; Wang, R.; Chi, Y.; Lin, X.; Chen, G., Blue luminescent graphene quantum dots and graphene oxide prepared by tuning the carbonization degree of citric acid. *Carbon* **2012,** *50* (12), 4738-4743.

140. Zhang, M.; Bai, L.; Shang, W.; Xie, W.; Ma, H.; Fu, Y.; Fang, D.; Sun, H.; Fan, L.; Han, M., Facile synthesis of water-soluble, highly fluorescent graphene quantum dots as a robust biological label for stem cells. *Journal of materials chemistry* **2012,** *22* (15), 7461-7467.

141. Shang, W.; Zhang, X.; Zhang, M.; Fan, Z.; Sun, Y.; Han, M.; Fan, L., The uptake mechanism and biocompatibility of graphene quantum dots with human neural stem cells. *Nanoscale* **2014,** *6* (11), 5799-5806.

142. Gupta, V.; Chaudhary, N.; Srivastava, R.; Sharma, G. D.; Bhardwaj, R.; Chand, S., Luminscent graphene quantum dots for organic photovoltaic devices. *Journal of the American Chemical Society* **2011,** *133* (26), 9960-9963.

143. Li, Y.; Hu, Y.; Zhao, Y.; Shi, G.; Deng, L.; Hou, Y.; Qu, L., An electrochemical avenue to green ‐ luminescent graphene quantum dots as potential electron ‐ acceptors for photovoltaics. *Advanced materials* **2011,** *23* (6), 776-780.

144. Zhao, J.; Chen, G.; Zhu, L.; Li, G., Graphene quantum dots-based platform for the fabrication of electrochemical biosensors. *Electrochemistry Communications* **2011,** *13* (1), 31-33.

145. Zhao, K.; Yu, X., A case based reasoning approach on supplier selection in petroleum enterprises. *Expert Systems with Applications* **2011,** *38* (6), 6839-6847.

146. Tissot, B. P.; Welte, D. H., *Petroleum formation and occurrence*. Springer Science & Business Media: **2013**.

147. Trenberth, K. E.; Fasullo, J. T.; Kiehl, J., Earth's global energy budget. *Bulletin of the American Meteorological Society* **2009,** *90* (3), 311-324.

148. Lesage, D.; Van de Graaf, T., *Global energy governance in a multipolar world*. Routledge: **2016**.

149. Petroleum, B., BP Statistical Review of World Energy Report. *BP: London, UK* **2019**.

150. Bentley, R. W., Global oil & gas depletion: an overview. *Energy policy* **2002,** *30* (3), 189-205.

151. Millero, F. J.; Huang, F., The density of seawater as a function of salinity (5 to 70 g kg-1) and temperature (273.15 to 363.15 K). *Ocean Science* **2009,** *5* (2).

152. Evdokimov, I. N.; Eliseev, N. Y.; Iktisanov, V. A., Excess density in oilfield water—crude oil dispersions. *Journal of colloid and interface science* **2005,** *285* (2), 795-803.

153. Buckmaster, J., Viscous–gravity spreading of an oil slick. *Journal of Fluid Mechanics* **1973,** *59* (3), 481-491.

154. Ermakov, S. A.; Zujkova, A. M.; Panchenko, A. R.; Salashin, S. G.; Talipova, T. G.; Titov, V. I., Surface film effect on short wind waves. *Dynamics of atmospheres and oceans* **1986,** *10* (1), 31-50.

155. Li, P.; Cai, Q.; Lin, W.; Chen, B.; Zhang, B., Offshore oil spill response practices and emerging challenges. *Mar Pollut Bull* **2016,** *110* (1), 6-27.

156. Kaushik, M., 11 Major Oil Spills Of The Maritime World. **2019**.

157. Baffes, J., Oil spills on other commodities. *Resources Policy* **2007,** *32* (3), 126-134.

158. Kujawinski, E. B.; Kido Soule, M. C.; Valentine, D. L.; Boysen, A. K.; Longnecker, K.; Redmond, M. C., Fate of dispersants associated with the Deepwater Horizon oil spill. *Environmental science & technology* **2011,** *45* (4), 1298-1306.

159. McNutt, M. K.; Camilli, R.; Crone, T. J.; Guthrie, G. D.; Hsieh, P. A.; Ryerson, T. B.; Savas, O.; Shaffer, F., Review of flow rate estimates of the Deepwater Horizon oil spill. *Proceedings of the National Academy of Sciences* **2012,** *109* (50), 20260-20267.

160. Blumer, M.; Sanders, H. L.; Grassle, J. F.; Hampson, G. R., An ocean of oil: a small oil spill. *Environment: Science and Policy for Sustainable Development* **1971,** *13* (2), 2-12.

161. Chang, S. E.; Stone, J.; Demes, K.; Piscitelli, M., Consequences of oil spills: a review and framework for informing planning. *Ecology and Society* **2014,** *19* (2).

162. Chen, J.; Zhang, W.; Wan, Z.; Li, S.; Huang, T.; Fei, Y., Oil spills from global tankers: Status review and future governance. *Journal of cleaner production* **2019,** *227*, 20-32.

163. Yin, L.; Zhang, M.; Zhang, Y.; Qiao, F., The long-term prediction of the oil-contaminated water from the Sanchi collision in the East China Sea. *Acta Oceanologica Sinica* **2018,** *37* (3), 69-72.

164. Agrawal, H.; Welch, W. A.; Miller, J. W.; Cocker, D. R., Emission measurements from a crude oil tanker at sea. *Environmental science & technology* **2008,** *42* (19), 7098-7103.

165. Wan, Z.; Chen, J., Human errors are behind most oil-tanker spills. Nature Publishing Group: **2018**.

166. Itopf, Oil tanker spill statistics 2016. ITOPF London, UK: **2017**.

167. Dave, D.; Ghaly, A. E., Remediation technologies for marine oil spills: A critical review and comparative analysis. *American Journal of Environmental Sciences* **2011,** *7* (5), 423.

168. Brandvik, P. J.; Daling, P. S., Optimisation of oil spill dispersant composition by mixture design and response surface methods. *Chemometrics and Intelligent Laboratory Systems* **1998,** *42* (1-2), 63-72.

169. Gundlach, E. R.; Hayes, M. O., Vulnerability of coastal environments to oil spill impacts. *Marine technology society Journal* **1978,** *12* (4), 18-27.

170. Ivshina, I. B.; Kuyukina, M. S.; Krivoruchko, A. V.; Elkin, A. A.; Makarov, S. O.; Cunningham, C. J.; Peshkur, T. A.; Atlas, R. M.; Philp, J. C., Oil spill problems and sustainable response strategies through new technologies. *Environmental Science: Processes & Impacts* **2015,** *17* (7), 1201-1219.

171. Kochurova, N. N.; Rusanov, A. I., Dynamic surface properties of water: Surface tension and surface potential. *Journal of Colloid and Interface Science* **1981,** *81* (2), 297-303.

172. Garrett, W. D.; Barger, W. R., Factors affecting the use of monomolecular surface films to control oil pollution on water. *Environmental Science & Technology* **1970,** *4* (2), 123-127.

173. Langmuir, I., Oil lenses on water and the nature of monomolecular expanded films. *The Journal of Chemical Physics* **1933,** *1* (11), 756-776.

174. Pramauro, E.; Pelezetti, E., *Surfactants in analytical chemistry*. Elsevier Amsterdam: **1996**.

175. Salafranca, J.; Gazquez, J.; Pérez, N. s.; Labarta, A.; Pantelides, S. T.; Pennycook, S. J.; Batlle, X.; Varela, M., Surfactant organic molecules restore magnetism in metal-oxide nanoparticle surfaces. *Nano letters* **2012,** *12* (5), 2499-2503.

176. Yang, Y.; Fang, Z.; Chen, X.; Zhang, W.; Xie, Y.; Chen, Y.; Liu, Z.; Yuan, W., An Overview of Pickering Emulsions: Solid-Particle Materials, Classification, Morphology, and Applications. *Front Pharmacol* **2017,** *8*, 287.

177. Chevalier, Y.; Bolzinger, M.-A., Emulsions stabilized with solid nanoparticles: Pickering emulsions. *Colloids and Surfaces A: Physicochemical and Engineering Aspects* **2013,** *439*, 23-34.

178. Binks, B. P., Particles as surfactants—similarities and differences. *Current opinion in colloid & interface science* **2002,** *7* (1-2), 21-41.

179. Creighton, M. A.; Ohata, Y.; Miyawaki, J.; Bose, A.; Hurt, R. H., Two-dimensional materials as emulsion stabilizers: interfacial thermodynamics and molecular barrier properties. *Langmuir* **2014,** *30* (13), 3687-3696.

180. Wu, H.; Yi, W.; Chen, Z.; Wang, H.; Du, Q., Janus graphene oxide nanosheets prepared via Pickering emulsion template. *Carbon* **2015,** *93*, 473-483.

181. Mosby, B. M.; Díaz, A.; Clearfield, A., Surface modification of layered zirconium phosphates: a novel pathway to multifunctional materials. *Dalton Transactions* **2014,** *43* (27), 10328-10339.

182. Mosby, B. M.; Díaz, A.; Bakhmutov, V.; Clearfield, A., Surface functionalization of zirconium phosphate nanoplatelets for the design of polymer fillers. *ACS applied materials & interfaces* **2014,** *6* (1), 585-592.

183. Wang, X.; Zhao, D.; Medina, I. B.; Diaz, A.; Wang, H.; Clearfield, A.; Mannan, M. S.; Cheng, Z., Surface modification of layered zirconium phosphate with PNIPAM. *Chem Commun (Camb)* **2016,** *52* (26), 4832-5.

184. Tian, X.; He, W.; Cui, J.; Zhang, X.; Zhou, W.; Yan, S.; Sun, X.; Han, X.; Han, S.; Yue, Y., Mesoporous zirconium phosphate from yeast biotemplate. *Journal of colloid and interface science* **2010,** *343* (1), 344-349.

185. Díaz, A.; David, A.; Pérez, R.; González, M. L.; Báez, A.; Wark, S. E.; Zhang, P.; Clearfield, A.; Colón, J. L., Nanoencapsulation of insulin into zirconium phosphate for oral delivery applications. *Biomacromolecules* **2010,** *11* (9), 2465-2470.

186. Kalita, H.; Kumar, B. N. P.; Konar, S.; Tantubay, S.; Mahto, M. K.; Mandal, M.; Pathak, A., Sonochemically synthesized biocompatible zirconium phosphate nanoparticles for pH sensitive drug delivery application. *Materials Science and Engineering: C* **2016,** *60*, 84-91.

187. CampbellàScott, J., Microwave-assisted synthesis of monodispersed CdTe nanocrystals. *Chemical Communications* **2010,** *46* (27), 4971-4973.

188. Fei, H.; Dong, J.; Wan, C.; Zhao, Z.; Xu, X.; Lin, Z.; Wang, Y.; Liu, H.; Zang, K.; Luo, J., Microwave‐Assisted Rapid Synthesis of Graphene‐Supported Single Atomic Metals. *Advanced Materials* **2018,** *30* (35), 1802146.

189. Standard, A., D1141-98: Standard Practice for the Preparation of Substitute Ocean Water. *ASTM International, West Conshohocken* **2013**.

190. Buist, I.; Meyer, P. In *Research on using oil herding agents for rapid response in situ burning of oil slicks on open water*, Proceedings of the Thirty-fifth AMOP Technical Seminar on Environmental Contamination and Response, **2012**; pp 480-505.

191. Lee, K.; Tong, L. T.; Millero, F. J.; Sabine, C. L.; Dickson, A. G.; Goyet, C.; Park, G. H.; Wanninkhof, R.; Feely, R. A.; Key, R. M., Global relationships of total alkalinity with salinity and temperature in surface waters of the world's oceans. *Geophysical research letters* **2006,** *33* (19).

192. Huang, D.; Sebastian, R.; Zhang, L.; Xu, H.; Lei, S.; Chen, M.; Shinde, A.; Ma, R.; Mannan, M. S.; Cheng, Z., Biocompatible Herder for rapid oil spill treatment over a wide temperature range. *Journal of Loss Prevention in the Process Industries* **2019**, 103948.

193. Qu, S.; Wang, X.; Lu, Q.; Liu, X.; Wang, L., A biocompatible fluorescent ink based on water‐soluble luminescent carbon nanodots. *Angewandte Chemie international edition* **2012,** *51* (49), 12215-12218.

194. Li, X.; Zhou, Z.; Lu, D.; Dong, X.; Xu, M.; Wei, L.; Zhang, Y., The effect of pristine carbon-based nanomaterial on the growth of green gram sprouts and pH of water. *Nanoscale research letters* **2014,** *9* (1), 583.

195. Zeng, M.; Echols, I.; Wang, P.; Lei, S.; Luo, J.; Peng, B.; He, L.; Zhang, L.; Huang, D.; Mejia, C., Highly Biocompatible, Underwater Superhydrophilic and Multifunctional Biopolymer Membrane for Efficient Oil–Water Separation and Aqueous Pollutant Removal. *ACS Sustainable Chemistry & Engineering* **2018,** *6* (3), 3879-3887.

APPENDIX A

MICROWAVE-ASSISTED PREPARATION OF 2D ZRP HERDING SURFACTANTS FOR OFFSHORE OIL SPILL MITIGATION*

A.1 Synopsis

Crude oil spill is the uncontrolled release of liquid hydrocarbon by ruptured pipelines and tanker hulls, or blowouts and leaks from offshore storage facilities and drilling rigs, either by faulty human behaviors or inevitable natural aging processes. Spills cause disastrous environmental and economic consequences, with the effects of marine habitat damage for lasting decades, necessitating a critical need for efficient oil spill mitigation and leakage treatment. In this study, we develop one kind of 2D amphiphilic nanoplate herding surfactant for retracting spilled oil offshore on the seawater surface with various temperature and saline concentrations. Applying 2D nanoplate herding surfactant causes areas of thin oil slick floating on water to largely shrink and form a thick bulk layer.

This transformation lays the foundation for the next-step oil treatment and recovery. The microwave-assisted synthesis method was used to fabricate the surface-modified ZrP nanoplates as the oil herder, which has an amphiphilic characteristic containing both hydrophilic and hydrophobic properties. The 2D nanoplate surfactants

* Parts of this chapter are reprinted with permission from (1) "Microwave-assisted preparation of two-dimensional amphiphilic nanoplate herding surfactants for offshore oil spill treatment." by Huang, D., Xu, H., Jacob, B., Ma, R., Yuan, S., Zhang, L., Mannan, M.S. and Cheng, Z., 2020. Journal of Loss Prevention in the Process Industries, 66, p.104213. Copyright 2021 by Elsevier. (2) "Biocompatible Herder for rapid oil spill treatment over a wide temperature range." by Huang, D., Sebastian, R., Zhang, L., Xu, H., Lei, S., Chen, M., Shinde, A., Ma, R., Mannan, M.S. and Cheng, Z., 2019. Journal of Loss Prevention in the Process Industries, 62, p.103948. Copyright 2021 by Elsevier.

decrease the air-water surface tension to facilitate the oil herding process efficiently. Using this herding procedure, we propose a biocompatible, high herding efficiency and cost-effective 2D herding surfactant fabrication method and offer a new direction for oil treatment in the offshore process safety field.

A.2 Introduction

With the global economic integration, petroleum has been paid more attention by governments as a strategic reserves material, which has led to the rapid development of offshore oil exploitation and transportation.[145, 146] Oil, coal, natural gas, nuclear power and renewable energy are the global primary energy types and the consumption percentage of oil has been stable in the 1st place within 30 years.[147, 148] Figure 42 represented global crude oil production in the past two decades.[149, 150] The crude oil production including offshore and onshore oil, increased from 75.6 to 95.9 million barrels per day between 2000 to 2019, which has an incredible 27% addition. It is worth noting that offshore oil production has a slight increase in the last 10 years and accounts for around 31% of total annual oil production, which indicated there is large potential that offshore oil production will continue increasing in the near future.

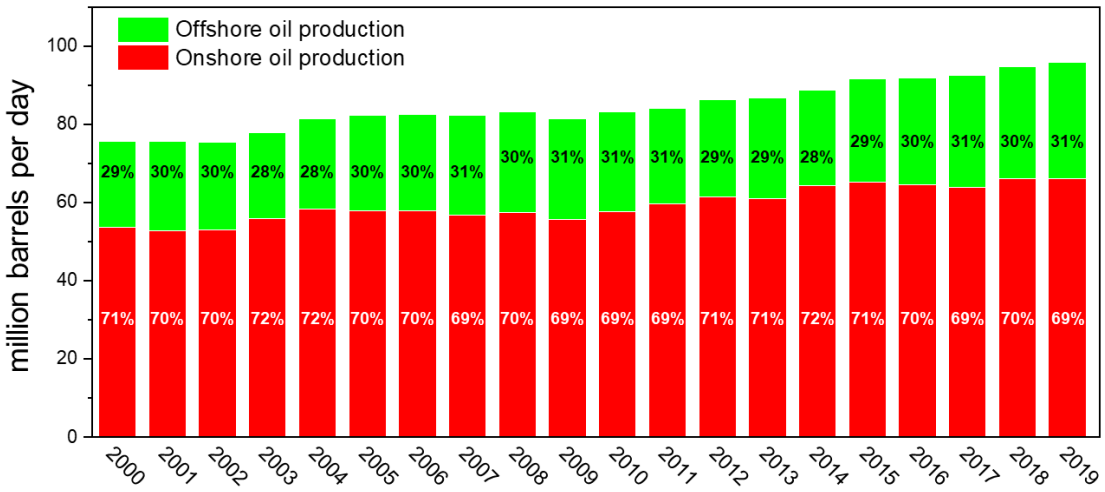

Figure 42. Global crude oil production of 2000-2019. The unit is million barrels per day.[149]

Unfortunately, offshore oil spills are inevitable to happen due to human's faulty operation or breaking down of facility. Oil, liquid hydrocarbon petroleum technically, in most cases has the lighter density (800-950 kg/m^3) than seawater (1020-1090 kg/m^3).[151, 152] The bulk of spilled oil leaking from the tanker or platform will float on the seawater surface, and starts to spread horizontally to form a very thin oil slick. The slick thickness and its movement changes with the oil surface tension, wind, and currents.[153, 154] It has been widely proven and shown empirically that oil spills have devastating effect on marine environmental, economic, public health and social effect.[155]

The world has witnessed countless oil spill scenes. Figure 43 labelled 15 largest oil spills in history occurrence in the world up to 2019.[156, 157] Among them, on April 20th 2010, the Deepwater Horizon offshore drilling rig suffered an explosion and fire due to improper management and operations. The drilling rig then sank into the Gulf of Mexico two days later and causing the marine oil spill incident. In the 10 years since the incident,

the ecological system of the coastline remain damaged by land erosion and oil contamination and local economy remains heavily affected.[158, 159] We can clearly see from Figure 43 that oil spills could occur on any continent and in any ocean, in extreme temperature ranges, from Arctic to equator.

Table 6 summarized the 15 largest oil spills in history corresponding to Figure 43. It is worth noting that large-scale oil spills as shown in Figure 43 and summarized in Table 6 resulted in huge socio-economic impacts and attracted negative media and public attention. Besides of larger oil spills, more than half of the oil spills incidents are smaller in magnitude and are commonly existing, which often evade attention and more difficult to clean up.[160]

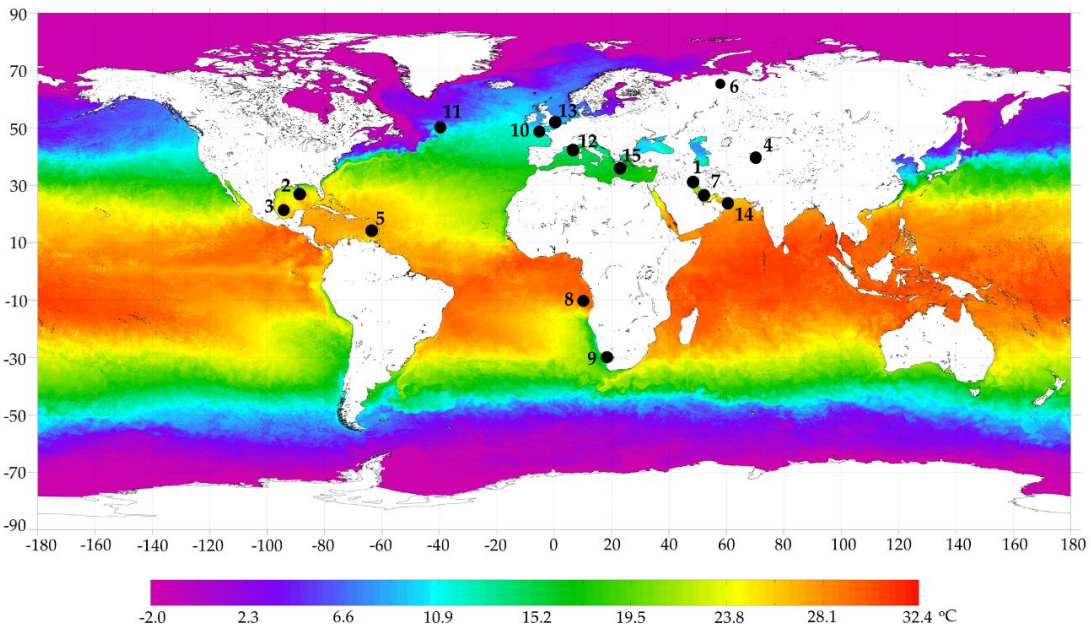

Figure 43. The world map showing locations of the 15 largest oil spills in history and sea surface temperature (5 km) contour chart. The black dots designate location of oil spills and numbers from 1 to 15 mean the volume ranking of the oil spill.

Table 6. Fifteen largest oil spills in history.

Rank	Date	Cause	Location	Source	Oil spill volume (million gallons)
1	1991.01.23	Gulf War	Persian Gulf	Oil rig	400
2	2010.04.20	Rig explosion	Gulf of Mexico	Deepwater Horizon oil rig	210
3	1979.06.03	Well blowout	Gulf of Mexico	Ixtoc 1 Oil well	140
4	1992.03.02	Well blowout	Fergana Valley, Uzbekistan	Oil well	88
5	1979.07.19	Tanker collision	Trinidad & Tobago	Atlantic Empress/ Aegean Captain Oil tanker	87
6	1994.09.08	Dam burst	Kharyaga, Russia	Oil reservoir	84
7	1983.02.04	Collision	Persian Gulf, Iran	Nowruz Fields Platform	80
8	1991.05.28	Explosion	Angola Offshore	ABT oil tanker	79
9	1983.08.06	Fire on tanker	Cape Town, South Africa	Castillo de Bellver oil tanker	78
10	1978.03.16	Tanker sinking	Coast of Brittany, France	Amoco Cadiz oil tanker	69
11	1988.11.10	Tanker explosion	North Atlantic off Coast of Canada	Odyssey oil tanker	43
12	1991.04.11	Tanker explosion	Coast of Genoa, Italy	MT Haven oil tanker	42
13	1967.03.18	Tanker leakage	Southwest Coast of United Kingdom	Torrey Canyon oil tanker	36
14	1972.12.19	Tanker collision	Gulf of Oman	Sea Star oil tanker	35
15	1980.02.23	Tanker fire	Port of Pylos	Irenes Serenade oil tanker	30

In addition to offshore oil platform spills, oil tankers spills also account for a large proportion on all offshore accidents.[161, 162] Oil spill amount which is larger than 5000 barrels would be considered as large oil spill and amount equal or smaller than 5000 barrels would be considered as small oil spill. Figure 44 summarized worldwide oil spills from oil tank ships. From Figure 44a, it was easily seen that both large and small oil spills numbers have enormously decreased continuously from 1970s to 2010s. The oil spill number of 1970s was 12 times larger than that of in 2010s, proving the successful process safety precautions taken by oil tankers, but number of large oil spill still needs more attention due to instable factors.[163, 164] Figure 44b was a mixed chart summarizing oil spill amount and number of oil spills in latest 20 years. The incidence of small oil spill decreased during this time, and number of large oil spills remains relatively small, and with 2012 experiencing no large spills. The amount of oil spilled in one large spill incident, such as the Sanchi tanker in 2018, could be more than the sum of all other oil spill amount in 2010s and came with disastrous environmental effects to East China Sea.[165] So, every oil spill incident cannot be neglected and requires efficient treatment and recovery.

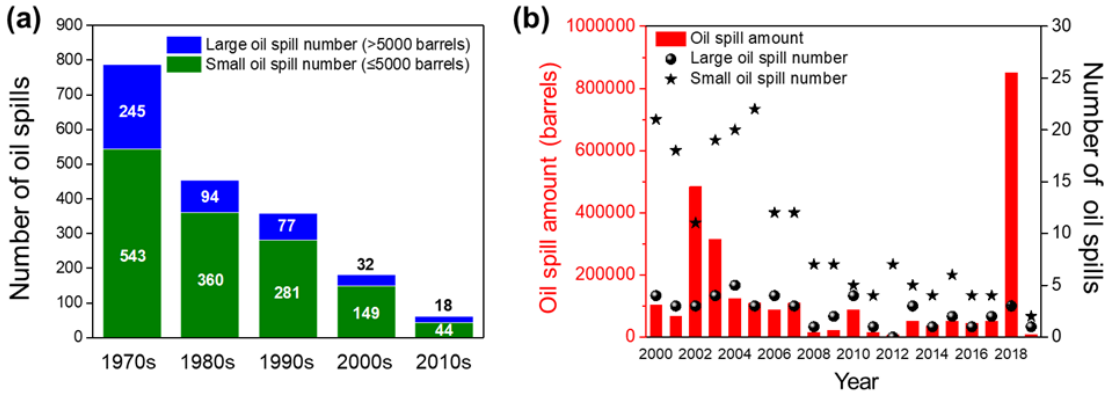

Figure 44. Worldwide oil tankers spill amount. (a) Spill number statistics 1970-2020. (b) Chart of oil spill amount and number of oil spills starting from 2000.[166]

When oil is spilled offshore, the remote location's oil spill response is complicated by the harsh conditions. In an open water, unknown wind and waves would accelerate oil slick expansion and encumber the mitigation treatment. Mechanical or chemical methods like oil booms, skimmers, dispersants; and biological agents, such as bacteria bioremediation are broadly used.[155, 167, 168] Mechanical methods usually need large number of labors and are easily restricted with local environment. Chemical methods usually have the environmental issue and unknown side effect to ocean creatures. Biological methods might need long time for processing and not suitable for coastal oil spill.[155, 169, 170] To reduce the environmental impact to marine system and to reduce labor work hazard when recovering oil manually, oil herders can be an alternate good choice for oil collecting and treatment.

Oil herding is a relatively new subject in oil spill treatment field. The initial definition of herder is the person who takes care of a herd of livestock. As a surfactant, a herder is an amphiphilic oil-collecting agent, designed to be sprayed around oil and to retract oil slick from a thin layer to form into a thick mass. Oil spread out quickly to form

a thin slick during the oil leak. Figure 45 explained the mechanism of oil herding process.[171-173] Three forces act upon the oily areas on seawater, oil-water ($\gamma_{O/W}$), oil-air ($\gamma_{O/A}$) and water-air ($\gamma_{W/A}$) surface tension exist in the system. The oil areas on seawater surface are controlled by these above forces. Before herding surfactant was applied, in Figure 45a, the spilled oil constantly spreads out due to the nonequilibrium state of the three forces. $\gamma_{W/A}$ (72.0 mN/m) is higher than the sum of $\gamma_{O/W}$ and $\gamma_{O/A}$ (25.0 mN/m), which can be written as the composition of force $F_{C1}=\gamma_{W/A} - \gamma_{O/A} - \gamma_{O/W} >0$. The oil areas continue expanding until the three forces reach new equilibrium ($F_C=0$). After the herding surfactant is applied around the oil (Figure 45b), the equilibrium state of water-air, oil-water and oil-air brakes up. The water-air surface tension decreases due to the monolayer formed by internal characteristics of amphiphilic herders and $F_{C2}=\gamma_{W/A} - \gamma_{O/A} - \gamma_{O/W} <0$. The composition of forces, therefore, drive oil slick into contracting until the three surface tension forces reach the new equilibrium state ($F_C=0$). When oil slick retracts, the volume of oil maintained the same and smaller oil slick areas resulting in a thicker oil bulk. And the oil slick after retraction facilitates for in situ burning due to the minimum burning thickness required.[174]

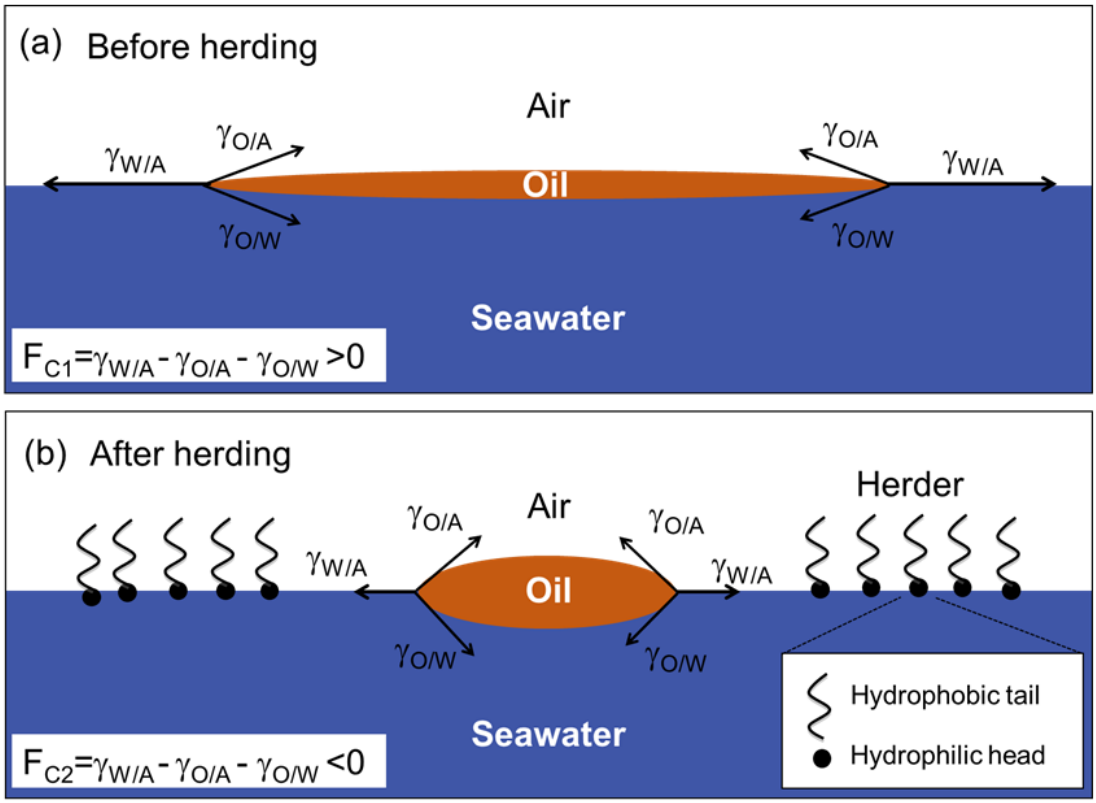

Figure 45. Schematics of oil spill on seawater and herding surfactant mechanism. (a) oil spill before herding and (b) oil spill after herding.

The herder, is a surface-active surfactant, has the amphiphilic characteristics, which is a combination of the hydrophobic tail group and the hydrophilic head group (Figure 45b), that is to say, tail is not attracting to water while head is attracting to water. Traditional surfactants are usually a category of organic molecules,[174, 175] but recently more two-dimensional nanoparticle surfactants have been reported.[176, 177] The 2D nanoparticle surfactants have the benefits of simple synthesis, convenient surface modification and precise surface coverage control compared to molecule surfactants.[178] They also exhibited larger surface area coverage and better atom utilization efficiency at

interface compared with other dimensions of nanoparticles due to their high surface-area-to-volume ratio and specific ultrathin thickness.[179, 180] Zirconium phosphate (ZrP) is a typical inorganic layered material. The internal hydrophilic property, biocompatibility and large aspect ratio of ZrP monolayer has contributed multiple surface modification reactions of ZrP and their broad applications.[36, 181-183] Specifically, the biocompatible and non-toxic properties of ZrP materials have created broad biological applications like drug delivery, yeast biotemplate and nanoencapsulation.[90, 184-186] And these relevant properties made it possible to utilize ZrP into the oil-water interfacial applications.

Different with traditional high temperature hydrothermal reaction method, microwave-assisted irradiation is a good substitute method for fabrication 2D nanoparticles. Synthetic microwave reactor produces much longer wavelength focusing directly on the samples than high temperature thermostat oven, and the reaction uses much less energy and completes more quickly. The microwave-assisted method will effectively avoid the materials aggregation by long time reactions needed by thermostat ovens. This simple, efficient and low-energy reaction method has thus garnered a lot of research interest.[187, 188]

Herein, in this research we develop a 2D surface-modified amphiphilic ZrP nanoplates as the herding surfactants for efficient oil herding strategy. The large active reaction sites and biocompatibility with marine system of the ZrP nanoplate herders made them a great candidate for oil spill treatment in remote offshore operations. The 2D nanoplate herders performed qualified herding efficiency in different temperatures and

saline density water bodies, which make them suitable for the variant oil spill environments.

A.3 Experimental

A.3.1 Chemicals

Zirconium chloride octahydrate ($ZrOCl_2 \cdot 8H_2O$), octadecyl isocyanate (ODI), anhydrous toluene (99.8%), and anhydrous dodecane (99%) were purchased from Sigma-Aldrich. The phosphoric acid (H_3PO_4) was purchased from TCI America. Tetra-(n-butylammonium) hydroxide 40% in water solution (TBAOH) was purchased from Sigma.

A.3.2 Herder fabrication

The amphiphilic 2D nanoplate herder had the characteristics of both hydrophilic and hydrophobic properties. The synthesis procedure included four steps. Firstly, hydrophilic ZrP nanoplates would be synthesized through microwave-assisted reaction. Secondly, the hydrophobic ODI would be grafted into the ZrP nanoplates, and samples would become hydrophobic with carbon chain grafting. Thirdly, TBAOH base was added into the above hydrophobic suspension to intercalate the multilayers of ZrP crystals. Finally, the samples went through sonication and complete full exfoliation. Therefore, the monolayer ZrP nanoplates were formed and the hidden hydrophilic functional group -OH between layers appeared. Both the hydrophilic and hydrophobic properties emerged in surface of the ZrP-ODI nanoplates and achieved the amphiphilic characteristic.

The microwave-assisted synthesis was performed in the Discover SP microwave synthesizer in Figure 46a. 3 g $ZrOCl_2 \cdot 8H_2O$ powder was placed into 30 mL 15 mol/L phosphoric acid in the 50 mL centrifuge tube, and stirred 10 min for homogeneous mixing. After that, 5 mL solution above was transformed to a 10 mL microwave glass vessel and 6 glass batches were achieved. Various glass vessel batches can react once a time and transfer automatically with Discover SP autosamplers when one reaction batch is ready. In contrast with conventional hydrothermal reaction in thermal oven for fabricating nanoparticles with long reaction time (>8 hours), high temperature (200 °C) and high power (1000 W) conditions,[25] the microwave irradiation reaction was setting at 170 °C, 100 W and a reaction time of 1 hour in the reaction chamber, as shown in Figure 46a and b. The localized superheating and direct activation of molecules in the vessels by microwave will accelerate the nucleation and growth of the ZrP nanocrystals. When the reaction was complete, the glass vessel was self-cooled down in 10 min and then autosampler would automatically change to another batch for reaction. The products were washed with DI water 4 times and went through centrifuging to remove unreacted H_3PO_4. The washed samples were set in a vacuum oven 24 hours at 75 °C for complete drying and were grinding into white powder for surface modification. The ZrP nanoplates showed hydrophilic performance due to abundant hydroxyl group.

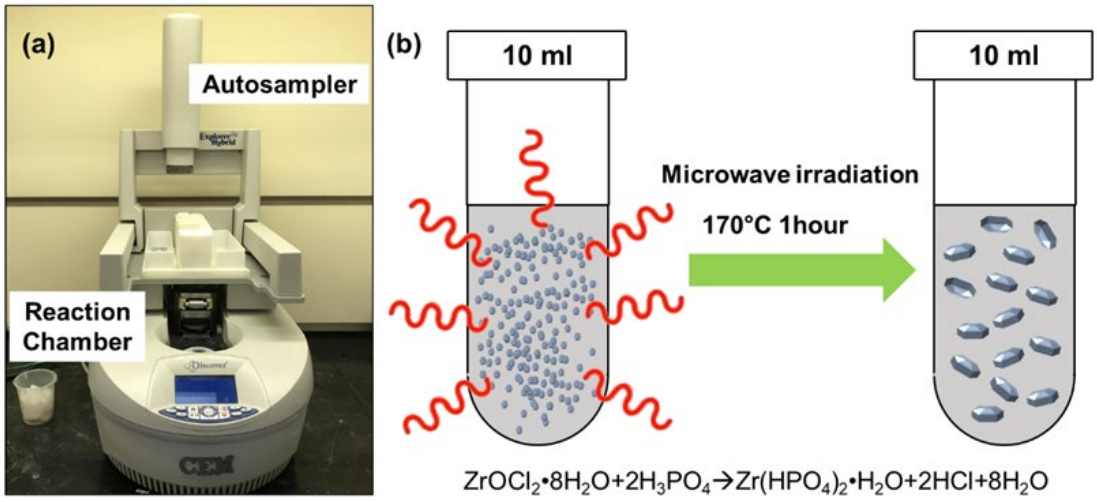

Figure 46. Microwave-assisted ZrP nanoparticle synthesis.

Figure 47 depicted the complete amphiphilic ZrP-ODI nanoplates synthesis process. 1.5 g ZrP powder was dispersed into 100 mL anhydrous toluene with adequate magnetic stirring. 0.16 g hydrophobic ODI with carbon chain was added into the ZrP suspension (ZrP/ODI molar ratio is 10: 1) and reacted for 6 hours under nitrogen at 40 °C (Figure 47a and b). The samples were washed with isopropanol and went through centrifuging to remove impurities. The final product was dried in an oven at 75 °C to obtain the hydrophobic surface-modified ZrP nanoplates.

The modified ZrP were then intercalated and exfoliated to obtain the amphiphilic nanoplate surfactant (Figure 47c and d). Exfoliated nanoplates were obtained by adding TBAOH in DI water at a molar ratio of 1:1 in ZrP and TBAOH. Detailly, 1.1 g ZrP-ODI was suspended into 15 mL DI water in a 30 mL centrifuge tube. TBAOH was added into the suspension and vortexed machine for 1 min for base intercalation. Then the suspension was subject to vigorous sonication for 2 hours, and the suspension stayed in room

temperature 2 days to guarantee the complete exfoliation of the TBAOH. Then we achieved the monolayer amphiphilic ZrP-ODI nanoplates (Figure 47d).

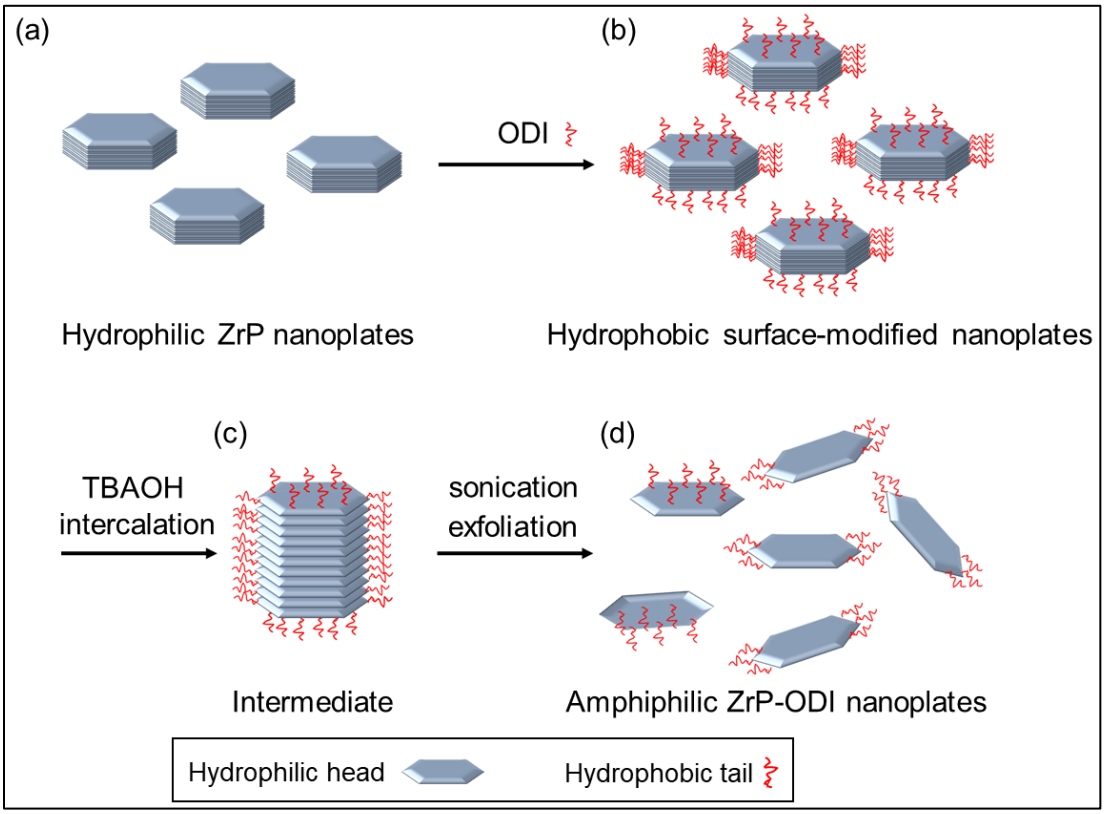

Figure 47. Schematic representation of modified amphiphilic ZrP-ODI nanoplates synthesis route.

A.3.3 Characterization

The microwave-assisted reactions were running with the Discover SP microwave synthesizer (CEM Corporation). The temperature of artificial seawater was adjusted through NESLAB RTE 7 (Thermo Electron). The pristine ZrP powder morphology was taken with JEOL scanning electron microscope (SEM) and the surface-modified amphiphilic ZrP-ODI powder morphology was imaged with TECNAI G2 transmission

electron microscope (TEM). Fourier-transform infrared spectroscopy (FTIR) was performed to investigate the chemical structures of nanoparticles. Dynamic light scattering (DLS) was tested to measure the size and distribution of nanoparticles. Pristine ZrP and modified ZrP-ODI powders were tested with thermogravimetric analysis (TGA) through TA Instruments Q500 to quantify ODI surface coverage grafting on the surface. The nanoplates were heated to 800 °C with a fixed heating rate under air and nitrogen mixture.

A.3.4 Herding test and analysis

Oil herding process was recorded under the Logitech HD Pro C920 Webcam on top of the handling tank. The image analysis software ImageJ was utilized to convert the lab-scale oil herding experiment photos into black-and-white mode. Then the image was transformed to only have oil areas, which could be used for counting number of pixels of oil spill areas photographs before and after herding on the surface, as shown in Figure 48.

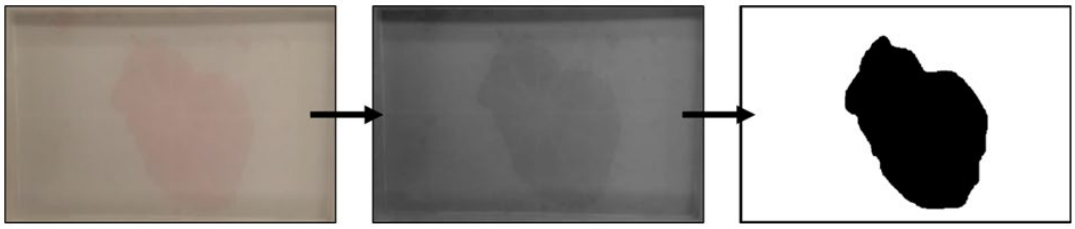

Figure 48. Image analysis of oil herding and pixels conversion.

A.4 Results and discussions

The morphology of pristine ZrP, ODI and modified ZrP-ODI was characterized in Figure 49. Figure 49a performed the SEM image of ZrP crystals. The hexagonal thick ZrP multilayer crystals were obviously shown. Figure 49b presented the TEM image of surface-modified monolayer ZrP-ODI nanoplate and kept the hexagonal configuration. The average thickness of pristine multilayer ZrP crystals was measured to be 120 nm and our previous work has reported that the thickness of exfoliated monolayer in Fig. 7b was 2.68 nm.[47] The average size of the ZrP-ODI nanoplate was measured with DLS to be 545 nm (Figure 49c). Then surface-modification of ZrP-ODI were confirmed by FTIR in Figure 49d. The $-CH_2-$ stretching vibration peak was clearly shown at 3000-2800 cm^{-1} in ZrP-ODI, while no stretching peak appeared in ZrP at the same range. Also, there were -NCO characteristics peak of 2250-2300 cm^{-1} shown in ODI spectra but there were no peaks shown at ZrP or ZrP-ODI, indicating successful surface modification of octadecyl isocyanate on ZrP nanoplates; -NCO was reacted and $-C_{18}H_{37}$ have been grafted onto the monolayer ZrP.

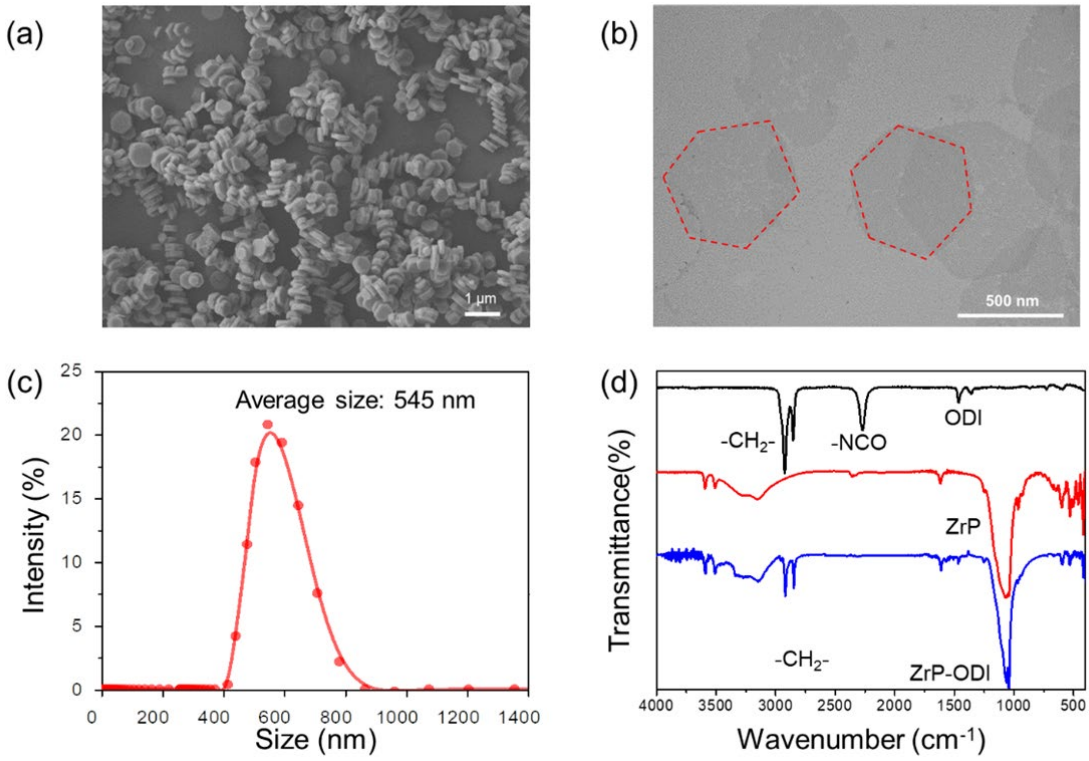

Figure 49. Characterization of ZrP and ZrP-ODI nanoplates. (a) The SEM image of ZrP crystals. (b) TEM image of ZrP-ODI nanoplates. (c) DLS size and distribution spectra of ZrP-ODI. (d) FTIR spectra of ODI, ZrP and ZrP-ODI.

The ODI surface modification coverage could be evaluated through thermogravimetric analysis (TGA). Figure 50 showed the TGA spectra of pristine ZrP and modified ZrP-ODI nanoplate between 25 and 800 °C. For pristine ZrP, it went through the thermo-decomposition and exhibited 14.1% weight decrease. For modified ZrP-ODI, the thermo-decomposition presented several weight losses stages. The first part from 25 to 205 °C was close to the pristine ZrP spectra and the loss might come from the water evaporation from ZrP surface and inside ZrP multilayers. The 205 to 465 °C region expressed a decomposition of carbon chain of ODI which grafted to ZrP. The 465 to 800

°C region was similar to the pristine ZrP and performed condensation of the phosphates. The 30.0% weight loss difference of ZrP and ZrP-ODI demonstrated the ZrP-ODI amphiphilic surface modification coverage.

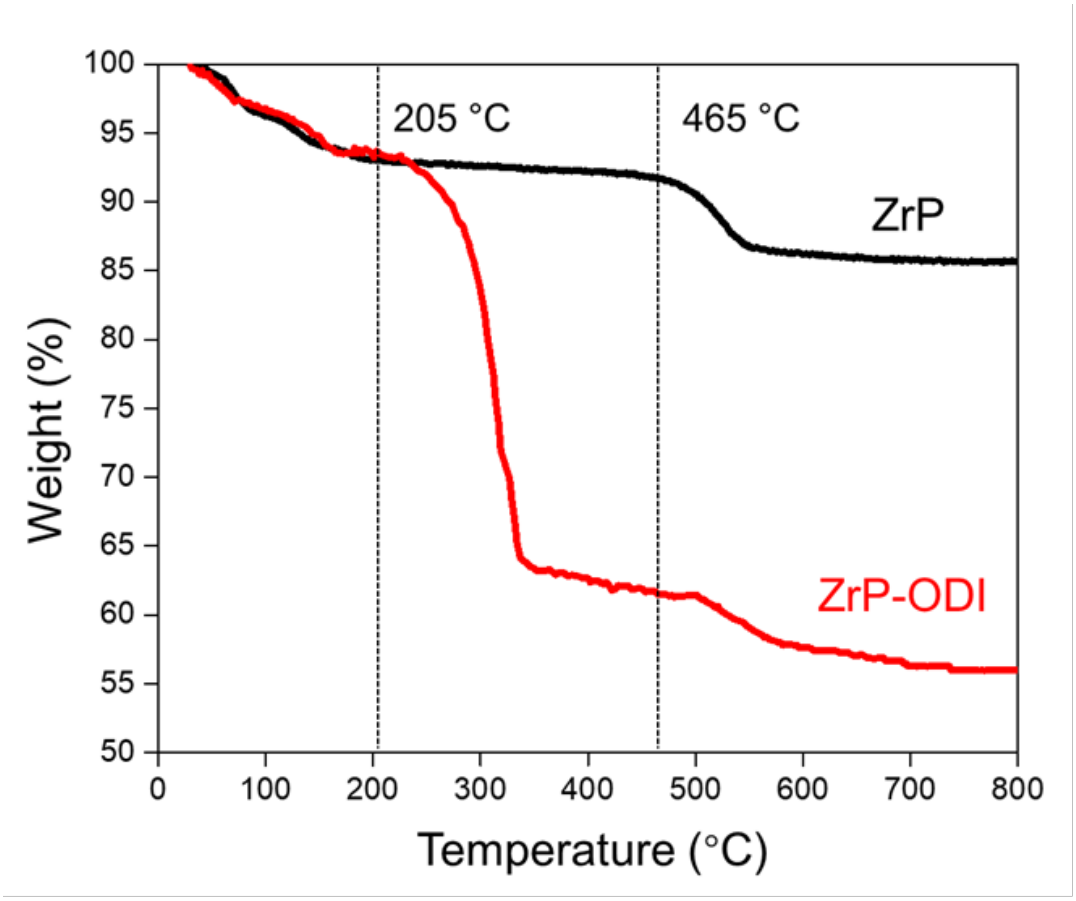

Figure 50. TGA of pristine ZrP crystals and amphiphilic ZrP-ODI nanoplates.

The oil herding experiment setup was performed below. Figure 51a and b presented the lab-scale oil herding experimental setup. A handling tank of dimension: 63.5 cm x 45cm x 8cm was utilized to mimic a sea environment. The camera was set on top of the tray to record oil herding process. Seawater was simulated through protocol ASTM D1141-98[189] with specific mineral salts and DI water, and the oil spill was simulated with

liquid hydrocarbon dodecane, dyed with 0.05 wt% Sudan IV for direct observation (Figure 51c). And Figure 51d showed an example of photographs for herding process.

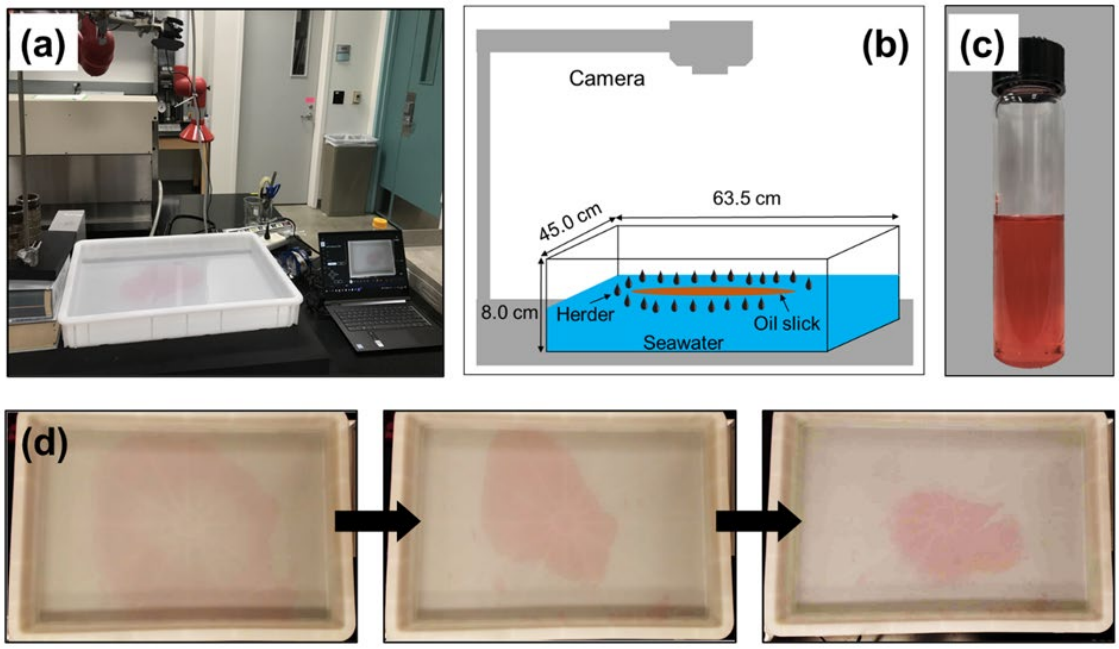

Figure 51. ZrP-ODI nanoplate oil herding facility. (a) Photograph of the lab-scale herding setup in lab. (b) Schematic herding experiment design. (c) Liquid hydrocarbon dodecane ($C_{12}H_{26}$) dyed with 0.05 wt% Sudan IV. (d) Photographs of oil herding process.

Herding efficiency of the fabricated 2D ZrP-ODI surfactant was evaluated in Figure 52. The oil slick thickness was achieved by dividing constant spilled oil volume by area on the seawater surface.[190] The herding surfactant would retract oil areas and increase the oil slick thickness simultaneously. Here, the ratio was defined as:

$$\text{Oil slick thickness ratio (\%)} = \frac{Slick\ thickness\ at\ equilibrium\ before\ herding}{Slick\ thickness\ at\ equilibrium\ after\ herding} * 100 \qquad (10)$$

Oil slick thickness ratio was an indicator of herding effect. A larger oil slick thickness ratio represented better surfactant herding efficiency. Oil areas were analyzed through ImageJ after herding 30 minutes and reaching a state of equilibrium. Firstly, ZrP-ODI herder efficiency under various saline water concentration environment was tested to evaluate the effect of water salinity on herding efficiency, as shown in Figure 52a. Four salinity concentrations of fresh water, 3.5 ppt saline water, 10 ppt saline water and 35 ppt seawater at 25 °C were used as simulations of a water body (ppt stands for parts per thousand, 35 ppt= 35 grams salt/1000g water). Before the herder was applied, the original oil slick thickness was kept at 100%. As different concentrations of ZrP-ODI herders were sprayed around oil, the slick started to aggregate and reached equilibrium in the end. Herding surfactants of 0.10 - 0.35 wt% of were tested separately in all four saline groups. Under the same salinity concentration, the oil thickness ratio increased with additional ZrP-ODI herder concentration. ZrP-ODI herding performance had better herding efficiency in lower saline concentration and has the largest oil slick thickness ratio in fresh water environment. Oil slick thickness ratio difference reduced when increasing herder concentration. The herding efficiency with various salinity was very close under 0.3 wt% and 0.35 wt% herder concentrations; and the herding efficiency only had 5% difference in thickness caused by salinity when reaching 0.3 wt% herding concentration. This demonstrated that salinity did not show an obvious side effect on ZrP-ODI herding.

The ZrP-ODI herders under different seawater temperatures were tested, as shown in Figure 52b. Temperatures of 5 °C, 15 °C, 25 °C and 35 °C were chosen to represent actual world seawater surface temperature[191] and seawater salinity was fixed at 35 ppt.

Similarly, the thickness ratio increased with adding more concentrated herder in all temperature ranges. But unlike small salinity effect in Figure 52a, temperature played an important role in herding process. Higher temperatures resulted in larger oil slick thickness ratio, in other words, better herding efficiency. The slick thickness ratio at 35 °C is 1.79 times that of 5 °C and 1.42 times that of 15 °C at 0.35 wt% herder concentration. The higher temperature accelerated herder monolayer movement towards the oil slick, enhancing ZrP-ODI surfactants herding efficiency.

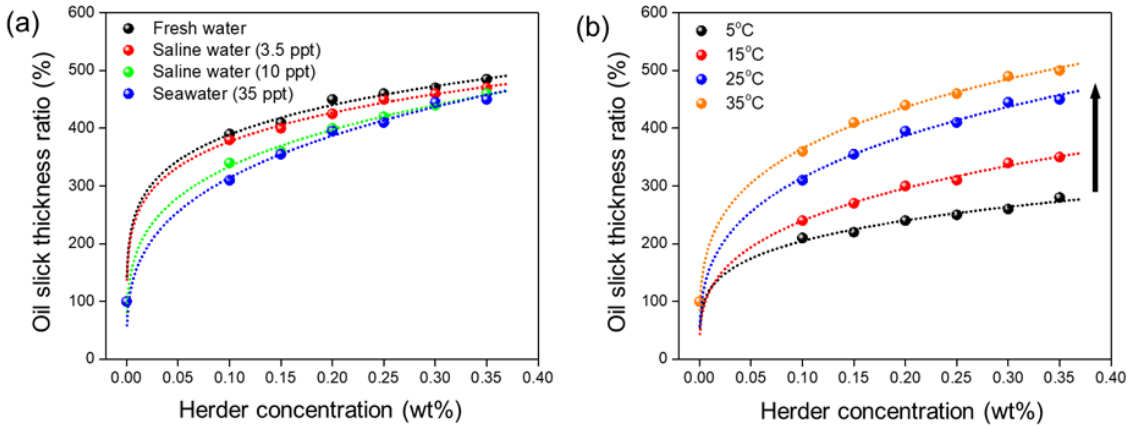

Figure 52. Herding efficiency evaluation with 2D ZrP-ODI surfactants. (a) Surfactants at different salinity concentration in 25 °C. (b) Surfactant at different temperatures in 35 ppt seawater.

Further herding experiments were tested to compare the herding efficiency of ZrP-ODI nanoplate surfactant (Figure 53). ZrP-ODI nanoplate, commercial Poly (ethylene glycol)-monolaurate herder (PEG-monolaurate), commercial US Navy herder Span 20, and our previous work and modified konjac glucomannan (MKGM) surfactant[192] were performed in 35 ppt artificial seawater and 25 °C conditions. We added 5 mL dodecane

on the seawater surface to simulate oil spill. The concentration of herders was fixed at 0.30 wt%. In Figure 53a, after oil herders were sprayed around the oil, four groups of oil slick areas all showed a substantial decrease in the first 5 minutes, changing from 1600-1800 cm^2 to 800-1000 cm^2. The rate started to slow down after 10 minutes' herding. After herding 30 minutes, all four areas of oil slicks decreased to be less than 510 cm^2, all demonstrating efficient herding. When investigating in detail of the herding 15-30 minutes in Figure 53b, the US Navy herder Span 20 performed the best efficiency, which had smallest oil slick area 260 cm^2, ZrP-ODI nanoplate herder had 2nd smallest oil slick area 330 cm^2, commercial PEG-monolaurate had area of 440 cm^2 and MKGM surfactant had area of 510 cm^2. Transformed to decreasing percentage of the herding areas, the ZrP-ODI had 78.2% better than PEG-monolaurate 75.3% and MKGM surfactant 69.7%, but smaller than 85.2% of Span 20. The amphiphilic nanoplate ZrP-ODI had much smaller particle size (545 nm) than MKGM (50-150 μm) in two magnitudes, so ZrP-ODI has much larger surface-area-to-volume ratio for surface modification than MKGM and resulted in better herding effect. Span 20 had a molecular surfactant structure which is of smaller size and containing more surfactant reaction sites than ZrP-ODI, but the molecular surfactant was not easy to synthesize and achieve surface functionalization. In contrast, the nanoplate surfactant ZrP-ODI was easy to fabricate, tune and complete surface modification, and performed as good herding efficiency as the molecular surfactant. Additionally, the price of commercial PEG-monolaurate and span 20 in Sigma Aldrich was $64.2/kg and $75.7/kg, and the price of the ZrP-ODI herding surfactant was calculated to be $51.4/kg, which made it possible for mass production. So, the ZrP-ODI nanoplate surfactants were

proved to be good choice for offshore oil spill treatment, both in experiment and economic perspective.

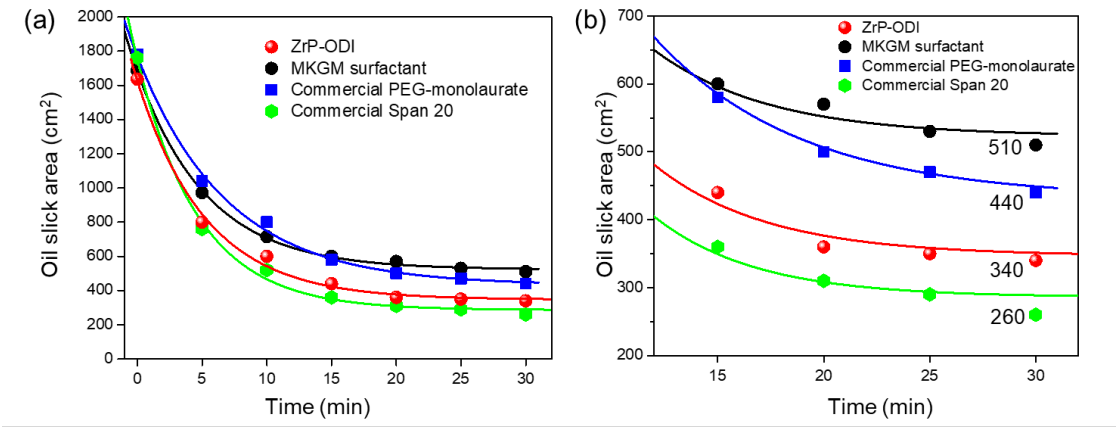

Figure 53. ZrP-ODI surfactant efficiency comparison with other herding surfactants under 25 °C, 35 ppt seawater environment. (a) Herding process 0-30 min. (b) Herding process 15-30 min.

The biocompatibility of materials could be evaluated through germination and growth of beans.[193-195] Here, the ZrP-ODI herding surfactants were tested, as shown in Figure 54. The experiment setup showed the intact black-eyed peas, black beans, and red beans in 6 separate containers. In comparative experiment (1), (3), (5), the peas and beans were growing with seawater environment, and in (2), (4), (6), peas and beans were growing with ZrP-ODI (5 wt%) seawater environment. The artificial seawater had a salinity of 3.5 wt%. After 5 days of growing at normal pressure and room temperature conditions, all beans and peas from (1) to (6) sprouted to some extent. Samples (1), (3), (5) has sprouted in seawater. And samples (2), (4) and (6) also sprouted in a similar growth

rate, indicating that the ZrP-ODI herding surfactants in seawater did not disturb the beans sprouting and proved ZrP-ODI good biocompatibility.

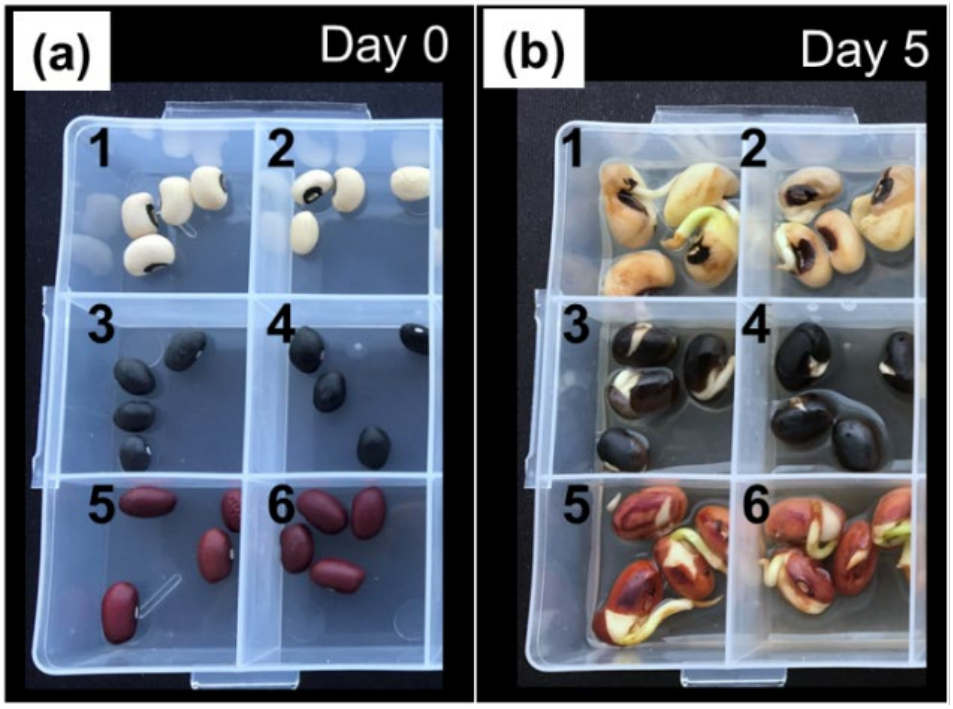

Figure 54. Biocompatible ZrP-ODI herding surfactant experiment. The black-eyed pea, black beans and red beans were tested. (1), (3), (5) were growing with artificial seawater and (2), (4), (6) were growing with ZrP-ODI (5 wt %) seawater, photograph of (a) day 0 and (b) day 5.

A.5 Summary

To conclude, a microwave-assisted preparation method of amphiphilic 2D ZrP-ODI nanoplate herding surfactant with good herding effect was successfully fabricated for offshore oil spill treatment. This microwave-assisted synthesis consumed just 20% of reaction time and energy for the nanoparticle nucleation and growth compared with the conventional hydrothermal method. The ZrP-ODI nanoparticle surfactant presented high oil herding efficiency and good biocompatibility under various seawater temperatures and saline concentrations. The 2D nanoplate surfactants might have the potential for becoming a new and broad medium for oil spill herding and making contributions to remote offshore oil process safety.